# CROSS-CALIBRATION

# FINAL REPORT


P. García-Lario[1]

with the collaboration of:

J. Blommaert[1], M. Burgdorf[1], D. Cesarsky[2], J. Chan[3], L. Decin[4], U. Klaas[5], R. Laureijs[1], T. Lim[3] Th. Müller[1], S. Peschke[1], A. Salama[1], R.F. Shipman[6], B. Schulz[1],



**SAI/2001-030/Rp, Version 2.0**

September 30, 2003



[1] ISO Data Centre, Astrophysics Division, Space Science Department of ESA, Villafranca, P.O. Box 50727, E-28080 Madrid, Spain
[2] Max Planck Institut für Extraterrestrische Physik, Giessenbachstrasse 1, D-85748 Garching, Germany
[3] Rutherford Appleton Laboratory, Chilton, Didcot, Oxon OX11 0QX, UK
[4] Katholieke Universiteit Leuven, Instituut voor Sterrenkunde, Celestijnenlaan 200B, B-3001 Heverlee, Belgium
[5] Max-Planck-Institut für Astronomie, Königstuhl 17, D-69117 Heidelberg, Germany
[6] Space Research Organization of The Netherlands, P.O. Box 800, NL-9700 AV Groningen, The Netherlands

## Document Information

| | |
|---|---|
| Document: | Cross-Calibration Final Report |
| Title: | Cross-Calibration Final Report |
| Reference Number: | SAI/2001-030/Rp |
| Issue: | Version 2.0 |
| Issue Date: | 25 September 2003 |
| Authors: | P. Garcia-Lario |

## Document Change Record

| **Date** | **Revision** | **Comments** |
|---|---|---|
| 22 March 2001 | Version 0.1 | First Draft |
| 14 August 2001 | Version 0.2 | Second Draft |
| 03 September 2001 | Version 0.3 | Third draft |
| 04 September 2001 | Version 1.0 | End of POPS version |
| 25 September 2003 | Version 2.0 | AAP version |

# Contents

# Chapter 1

# Introduction

## 1.1 The concept of cross-calibration

Cross-calibrations can be used (i) as consistency checks, and (ii) as true calibrations. In the first instance observations of a source by a pair of instruments are compared to evaluate internal consistency: if the results do not agree (to within the stated uncertainties) then the calibration procedure of one of the instruments (though possibly both) is incorrect. In the second instance, results from the less accurate instrument(s) can be calibrated against data from the more accurate one(s).

In the case of ISO, the above concept can be applied both to pairs of ISO instruments that overlap in wavelength range and also to ISO instruments vs other non-ISO instruments.

## 1.2 Cross-Calibration Strategy

During the Operational Phase a limited number of sources were observed repeatedly throughout the mission for cross-calibration purposes. The responsibility for instrument calibration rested with the Instrument Dedicated Teams (IDTs) located at VILSPA, and was supported by staff at the home institutes of the instrument teams. Demands from the different instruments and coordination of cross-calibration observations were handled by a dedicated 'Calibration Liaison' team.

As a result of these cross-calibration observations, the overall agreement among the major instrument modes was assessed in several occasions during the mission. The observations confirmed that the internal consistency in terms of absolute flux calibration was in general comparable to pre-launch expectations or better and led to the discovery of some calibration problems in the few cases where larger discrepancies than expected were found.

During Post-Operations, an improved cross-calibration plan was set up, based on the use of the whole ISO Data Archive for cross-calibration purposes, extending the analysis to a much larger number of sources. This way it was possible to study specific calibration problems in detail on dedicated subsets as well as to perform statistical analysis of the results obtained after specific calibration improvements were implemented in the pipeline in many cases.

In addition, it was decided to change the global IDC strategy for cross-calibration, from the rather 'instrument-oriented' approach which worked quite efficiently during the Operational Phase (but turned out to be inappropriate for Post-Operations) to a more 'calibration-topic' oriented organisation. For this, up to eight different Working Groups were established, each one addressing a specific calibration aspect (glitches, beam profiles and pointing, transients, line profiles, polarisation, spectral matching, general photometric calibration and interactive analysis

S/W). They were formed by members of the IDC and of the different NDCs, with all instruments represented, plus external contributors from other projects (ASTRO-F, SIRTF, Herschel,...) in many cases.

Their objectives were:

- Verify that, from a global point of view, the calibration of the individual ISO instruments was correct, and ensure a certain level of homogeneity and consistency of the data and how they were calibrated (e.g. compatibility of models, bandpass zero-points, and of calibration philosophy and procedures).
- Identify calibration problems, trigger/recommend further work, propose solutions and monitor the progress made, promoting the transfer of all useful information to the users community (new tools available, caveats,...).
- Compare the results of the different ISO instruments and seek for understanding the inconsistencies found and make similar comparisons with external data from ground-based or space facilities.

The progress made on each calibration topic under analysis was reflected every six months during Post-Operations in a series of *(Cross-)Calibration Status Reports* posted at the IDC web site where information was included on the latest achievements in the calibration of all four ISO instruments with special emphasis on cross-calibration aspects. At the end of the Post-Operations Phase (end of 2001) each of these Working Groups generated a Final Report, containing the final state-of-the-art of ISO calibration regarding each of the calibration problems addressed. All of them have been put together in this *ISO (Cross-)Calibration Final Report*.

This organisation turned out to be an ideal platform to exchange knowledge across the boundaries of the ISO instruments. The information gathered and the conclusions derived from the investigations carried out by members of these Working Groups on the many different calibration problems affecting the ISO instruments constitute an extraordinary source of information for other future space projects. Most of these results were presented to the astronomical community at *The Calibration Legacy of the ISO Mission*, [37] conference, held at VILSPA on February 5–9, 2001.

### 1.2.1 Definition of cross-calibration sources

As we have already mentioned, only a small set of astronomical sources was used during the Operational Phase for cross-calibration purposes. It was composed of a few bright stars (like HR 7310, HR 7341, HR 6436, $\gamma$ Dra or $\alpha$ Boo), planetary nebulae (NGC 7027 and NGC 6543), galaxies (Mrk 279), asteroids (Cybele, Hygiea) and planets (Neptune). For most of them, observations exist in IDA taken throughout the whole ISO mission with more than one instrument and in many cases covering a wide range of wavelengths.

During Post-Operations, and as part of the new cross-calibration strategy above described, the concept was extended to any source satisfying at least one of the following conditions:

- it should have been observed with more than one instrument/configuration at least once during the ISO mission (for internal cross-calibration purposes)
- infrared data from non-ISO instruments exist (for external cross-calibration)
- accurate models exist against which ISO data can be compared (for absolute flux calibration).

### 1.2.2 Limitations and caveats

Because of the limited common dynamic range between the ISO instruments, not all kind of internal cross-calibration comparisons were possible. In this respect, the cross-calibration of LWS with PHT in the long wavelength range was especially difficult, since the dynamic range overlap between PHT and LWS was very limited.

When comparing results derived from different instruments/detectors we also need to consider the differences in beam and filter profiles as well as in spatial and spectral resolution. This applies both to internal and external cross-calibration.

In addition, in the case of external cross-calibration, results obtained from facilities other than ISO may be based on different absolute calibration systems: different zero-points, different set of astronomical standards, different models used for the same standards, can introduce an undesired bias which has to be taken into account.

Last, but not least, some of the sources included for analysis may have been observed slightly off-axis, or show unexpected variability or extended emission escaping to our knowledge and, thus, can introduce some noise into the system. This makes cross-calibration even more complicated since individual spectra must be carefully checked one by one before being validated (see Figure 1.1).

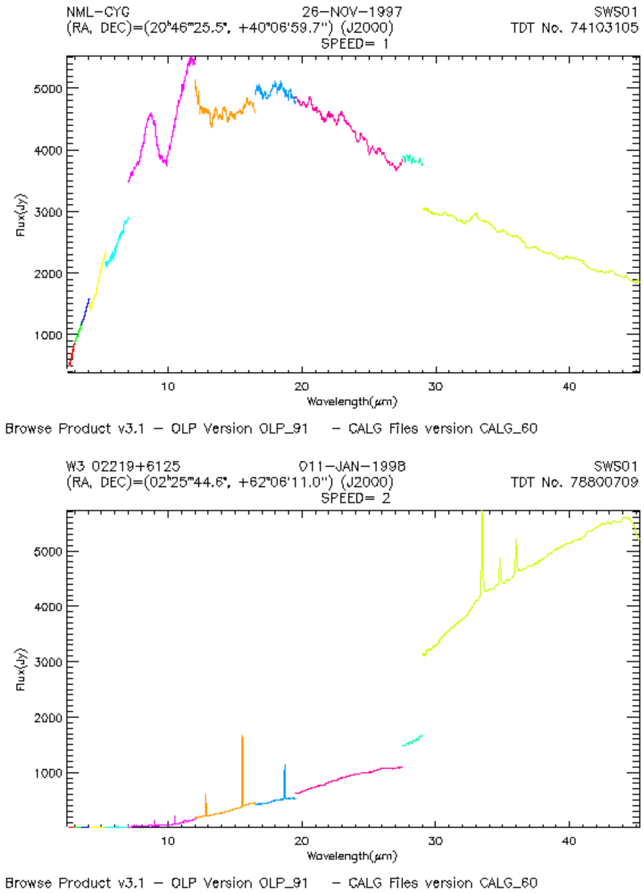


Figure 1.1: *Example of the discontinuities observed in SWS spectra as a consequence of a bad pointing (top) compared to the discontinuities due to the extended nature of the source observed (bottom). Note the always positive flux jumps towards longer wavelengths reflecting the progressive increase of the SWS apertures in this latter case.*

On the other hand, the accuracy of the absolute flux calibration is always limited by the accuracy of the available models. Stars are too faint in the long wavelength range of ISO (beyond 100 $\mu$m) to be used as standards, and asteroids and planets have to be used instead. While stellar models are believed to be accurate to $\pm 5\%$ or better, the uncertainties in asteroid and planet model spectral energy distributions are larger (10–15% level). In the case of asteroids their characterisation is additionally complicated by their variability, which limits the accuracy of the absolute flux calibration of ISO at long wavelengths.

In the following we will present a summary of the main results obtained from a number of internal and external cross-calibration analysis as well as from some consistency checks performed against available models.

Note that we intentionally exclude from this analysis internal cross-checks made by each instrument team within their own instrument detectors/bands/AOTs. These are addressed in the instrument specific volumes of the ISO Handbook and will not be discussed here.

# Chapter 2

# Internal Cross-Calibration

## 2.1 Between the ISO spectrometers

### 2.1.1 SWS versus PHT-S

The sample used for this internal cross-calibration comparison comprised around 100 different sources with both SWS (AOT SWS01) and PHT-S (AOT PHT40 either in staring or chopped mode) spectra available in IDA, showing a reasonable signal-to-noise ratio.

The OLP data products were compared in a systematic way since the end of the Post-Operations Phase with every new release since OLP Version 7. This resulted in the detection of several calibration problems affecting both PHT and SWS calibration that were conveniently reported in the corresponding *(Cross)-Calibration Status Report*.

As an example, one of the calibration problems discovered was the effect of poorly modelled molecular features in the spectra of the calibration stars used in the dynamic calibration of PHT-S, before it was implemented in Version 9.0 of the pipeline. Based on the comparison of OLP Version 7 SWS data and staring PHT-S observations of the asteroid Hygiea with the available thermophysical model it was possible to identify the residuals left in the calibrated PHT-S spectra between 8 and 9 $\mu$m by SiO features not considered in the original models of the late type stars taken as standards. Only excluding these stars from the generation of the calibration files (and hence accepting a larger gap in the flux range covered by the calibration standards) the spurious features were eliminated in the calibrated spectra. After the correction was introduced in OLP Version 9.0 the agreement between SWS01 and PHT-S staring observations improved significantly.

As of OLP Version 10, the level of agreement reached in terms of absolute flux between these two ISO instruments and observing modes was better than 10–15% for well-behaved data sets (bright, point-like sources not affected by any other known calibration problem). Moreover, the overall shape and even the faintest spectral features were also largely preserved from instrument to instrument (to within the few percent level in most cases) all over the spectral range covered by both instruments.

Figure 2.1 shows some examples which illustrate the good agreement found over a wide variety of sources with different spectral properties, all of them taken from this cross-calibration sample. The plotted spectra are OLP Version 10 data products directly retrieved from IDA corresponding to representative cases of sources showing a 'blue' (HR 7310 and HR 6132) or 'red' continuum (AFGL 4106 and OH 26.5+0.6), or sources where strong PAH emission bands and/or nebular emision lines (BD +30°3639 and NGC 7027) appear overimposed on the infrared continuum. A very good agreement between both instruments and the IRAS photometry at 12 $\mu$m (indicated with a blue square in the plots) is also found.

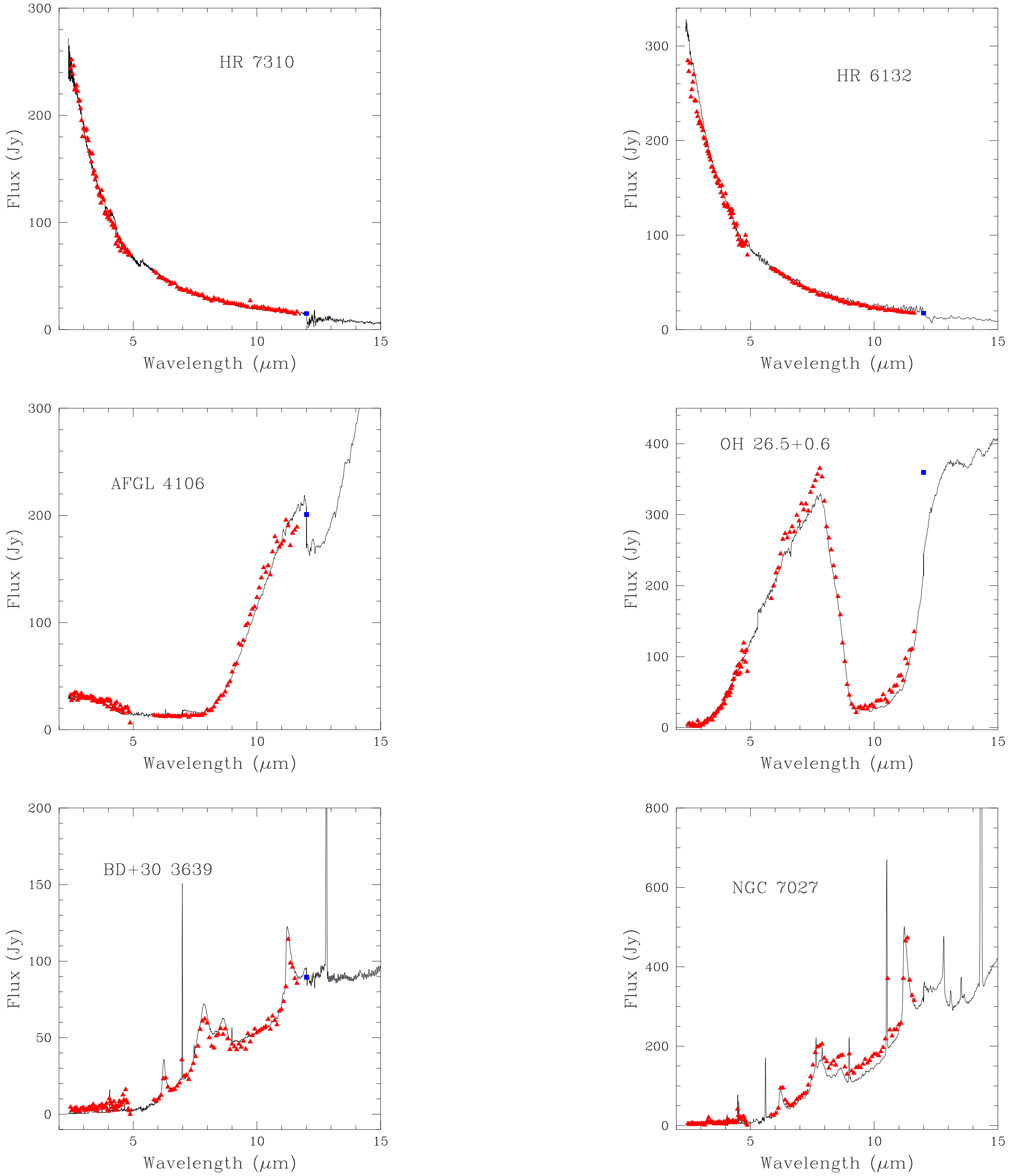


Figure 2.1: *SWS (black solid line) versus PHT-S (red filled triangles) OLP Version 10 spectra of a variety of sources with different spectral properties taken from the cross-calibration sample. The blue squares represent the IRAS photometry at 12 μm when available.*

The examples shown in Figure 2.1 correspond to relatively bright sources observed in all cases with PHT-S in staring mode. For the fainter sources the chopping mode of PHT-S was usually prefered and the behaviour of this mode was also investigated in terms of cross-calibration. The results obtained indicate a similar level of agreement with SWS (10–15%), in spite of the fact

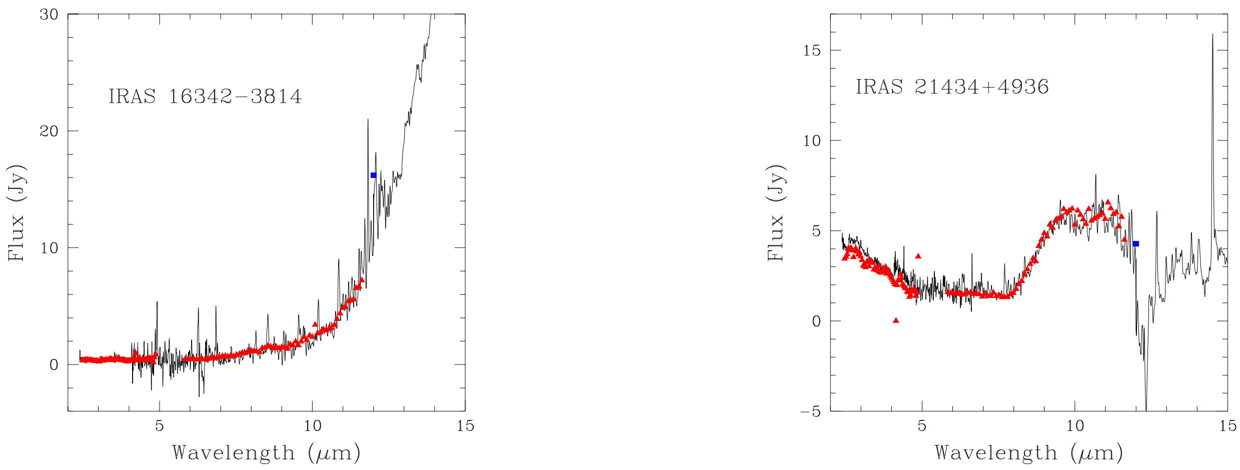


Figure 2.2: *Same as Figure 2.1 for two faint sources. Note the effect of an inaccurate dark current subtraction by the pipeline at the blue edge of band 3A (12.0 μm) in the SWS spectrum of IRAS 21434+4936. The blue squares represent again the IRAS photometry at 12 μm.*

that the accuracy achievable with SWS at low flux levels is not expected to be as good.

Figure 2.2 shows two *faint* sources (flux density below 5–10 Jy) observed with SWS and PHT-S. IRAS 16342−3814 was observed with PHT-S in staring mode while IRAS 21434+4936 was observed using triangular chopping. We can see that a very nice agreement exists at absolute flux level as well as in the shape of the individual SWS and PHT-S spectra in both cases. Again, there is also a very good agreement with the IRAS photometry at 12 μm.

Outside the overlapping spectral range, a significant jump in flux is detected at the blue edge of band 3A in the SWS spectrum of IRAS 21434+4936 at 12.0 μm. This is indicating an inaccurate dark current subtraction by the automated pipeline (OLP Version 10). This kind of problem is sometimes observed in the SWS spectra of faint sources and needs to be manually corrected with the use of the SWS interactive software analysis (OSIA) where the right dark current level can be interactively chosen, eliminating the problem.

### 2.1.2 SWS versus CAM-CVF

A similar exercise was performed with a sample of around 20 sources identified in IDA to have SWS (AOT SWS01) and CAM-CVF (AOT CAM04) spectra available with a signal-to-noise ratio enough to be used for cross-calibration purposes.

Again, the OLP data products were compared in a systematic way since the end of the Post-Operations Phase with every new pipeline release since OLP Version 7.

In this case, the main improvement implemented in the pipeline since the start of this cross-calibration analysis was the application of transient corrections based on the Fouks-Schubert method (Fouks & Schubert 1995, [17]) both to SWS01 (band 2) and CAM04 data, which are described in detail in the corresponding instrument specific volumes of the ISO Handbook.

As of OLP Version 10, the level of agreement between SWS01 and CAM04 spectra was in general within 10–15%, down to the limits were dark current subtraction becomes a significant contribution to the error budget (especially for SWS) over the whole spectral range covered by both instruments, with the exception of the edges of CAM-CVF scans, which might still be affected by transient effects even after the application of the Fouks-Schubert transient correction (this is true especially in the case of bright point sources, for which this correction simply does not work).

Figure 2.3 shows two examples where comparisons are made of CAM04 and SWS01 OLP Version 10 data products directly retrieved from IDA, taken from this cross-calibration sample. They correspond to the bright star HR 7310 (left panel) and to the fainter HD 179218 (right panel), which are representative of the general behaviour observed.

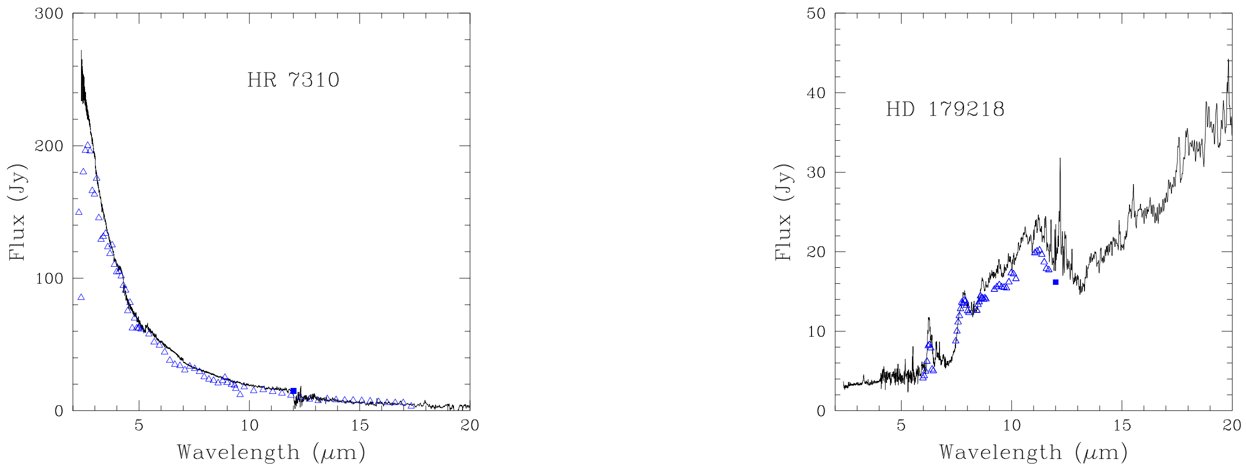


Figure 2.3: *SWS (black solid line) versus CAM-CVF (blue open triangles) OLP Version 10 spectra of two point sources taken from the cross-calibration sample. Note the strong transient observed at the blue edge of the CAM-CVF spectra of HR 7310 (left panel). The blue squares represent the IRAS photometry at 12 $\mu$m.*

As we can see, the agreement is very good with the only exception of the blue edge of the CAM-CVF spectrum of HR 7310, affected by strong transient effects at the beginning of the measurement. This is, as we have already mentioned, a common feature observed in many cases in CAM-CVF spectra of bright sources and its strength depends on the illumination history conditions. It is well known that the Fouks-Schubert correction which is applied in the pipeline only works efficiently for very weak and/or extended sources (i.e. for low flux gradients) and has a neutral effect on bright point sources like HR 7310. Unfortunately, the problem cannot be corrected with the help of CIA.

### 2.1.3 CAM-CVF versus PHT-S

Around 10 other sources were used for a similar internal cross-calibration comparison of CAM-CVF (AOT CAM04) and PHT-S (AOT PHT40 either in staring or chopping mode).

Figure 2.4 shows two examples where comparisons are made of CAM04 and PHT-S OLP Version 10 data products retrieved from IDA, taken from this small cross-calibration sample. They correspond to the bright star HR 7310 (left panel) and the faint HD 207129 (right panel), which are representative of the general behaviour observed.

Note that for the faint star HD 207129, the background continuum emission is not negligible. In this case, a background measurement available in IDA taken at a position 3′ away from the central source was used to subtract this contribution. The spectrum shown in Figure 2.4 is the result obtained after subtraction of this background.

We can see once more that a very good level of agreement exists (within 10–15%) in the overall shape and in the absolute flux level determined by the pipeline for CAM-CVF and PHT-S

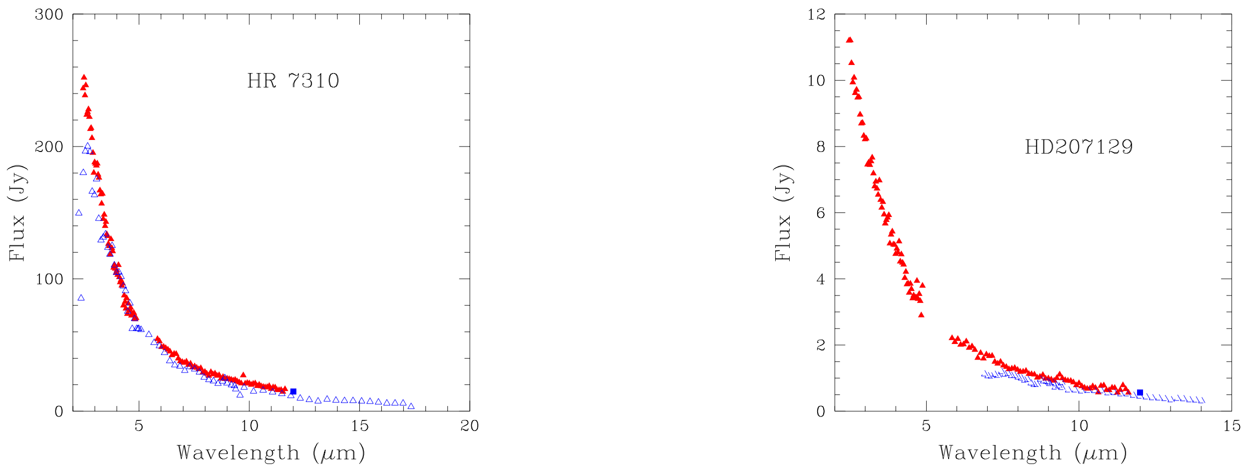


Figure 2.4: *CAM-CVF (blue open triangles) versus PHT-S (red filled triangles) OLP Version 10 spectra of two sources taken from the cross-calibration sample. As usual, the blue squares represent the IRAS photometry at 12 μm.*

spectra, as well as between the two instrument observing modes and the IRAS photometry at 12 $\mu$m.

Again, the main problem is the strong discrepancy observed at the short end of the CAM-CVF spectra of both HR 7310 and HD 207129 induced, as we have already mentioned, by transient effects in the ISOCAM detectors.

### 2.1.4 SWS/LWS overlap region

In order to extend our internal cross-calibration analysis to longer wavelengths we also checked the consistency of the absolute flux calibration of SWS (AOT SWS01) and LWS (AOT LWS01) in the overlapping region of these instruments. For this, a total number of 122 common pointings (separated less than $2''$) were selected from IDA for which both SWS and LWS measurements were available with fluxes between 43.7 and 44.4 $\mu$m higher than 100 Jy.

Sources identified as variable in the literature in this cross-calibration sample were identified and removed from the sample except when the SWS and the LWS measurements were taken on the same revolution (usually one after the other as concatenated observations). Similarly, all sources reported to be extended were also discarded to avoid problems derived from the comparison of fluxes measured through different aperture sizes. In addition, a few other sources were excluded from the analysis because they were identified either as badly pointed (off-axis) or as sources with a possible (not previously reported) extended nature, according to the strong discontinuities observed between SWS bands (see Figure 1.1).

After this purge, the resulting sample still contains around 50 different sources suitable for cross-calibration. A reduced subsample composed of 25 sources (used as test cases) were systematically investigated every time there was a new release of the automated pipeline since OLP Version 7. For each of them the average value of the observed flux density ratio LWS/SWS at 44 $\mu$m was determined using ISAP (assuming that the source SED shape was of the form $\nu \times f_\nu$ = constant, or equivalently $\lambda \times f_\lambda$ = constant).

As it also happened in other cross-calibration analysis performed during Post-Operations, some calibration problems were identified during the course of this exercise. The most important one in this case was the detection of an anomalous behaviour of the SW1 detector in LWS in all the spectra taken before revolution 237. The flux of this detector appeared systematically underestimated (around 20%) with respect to both the adjacent SW2 detector of LWS and band 4 of SWS. The problem was identified as related to an incorrect treatment by the pipeline of the illuminator flash sequence used by LWS before this revolution and solved in OLP Version 10.1 by applying the necessary modifications in the automated calibration software.

The results obtained as of OLP Version 10 for the 25 test cases above mentioned using ISAP Version 2.1 are listed in Table 2.1. Some examples of the corresponding composite SWS+LWS spectra are shown in Figure 2.5.

Table 2.1: *OLP Version 10 LWS/SWS ratios at 44 $\mu$m of the 25 test cases used to analyse the internal consistency between SWS and LWS absolute flux calibration.*

| Source | SWS TDT# | LWS TDT# | LWS/SWS | Notes |
|---:|---|---|---|---|
| HD 161796 | 07100579 | 07100579 | 0.95 | |
| HD 101584 | 07901402 | 07901520 | 1.01 | |
| Hen 2−113 | 07903307 | 07903229 | 0.98 | |
| HD 161796 | 07100579 | 08001732 | 1.03 | |
| CPD −56 8032 | 27301339 | 08401538 | 1.03 | |
| IRAS 16342−3814 | 45801328 | 08402827 | 0.94 | |
| Circinus | 07902231 | 10401133 | 1.26 | bad SWS band 4 |
| AFGL 4106 | 10401225 | 10401227 | 0.95 | |
| M 1−78 | 15901853 | 15901854 | 0.90 | |
| CW Leo | 19700159 | 19800158 | 1.11 | |
| $\mu$ Cep | 08001274 | 22002005 | 1.07 | |
| SAO 34504 | 26302115 | 26300513 | 1.12 | bad SWS band 4 |
| IRAS 19114+0002 | 52000234 | 31900901 | 0.96 | |
| OH 26.5+0.6 | 33000525 | 33000316 | 1.01 | |
| VX Sgr | 09900171 | 33100802 | 1.04 | |
| IRAS 15452−5459 | 45900615 | 48800916 | 1.12 | bad SWS band 4 |
| IRAS 16594−4656 | 45800441 | 49001642 | 1.02 | |
| IRAS 19114+0002 | 52000234 | 52500861 | 1.00 | |
| R Dor | 58900918 | 59300644 | 1.03 | |
| Hen 2−113 | 07903307 | 60701891 | 1.07 | |
| CRL 618 | 68800561 | 68800450 | 0.90 | bad SWS band 4 |
| IC 418 | 82901301 | 68900805 | 1.04 | |
| TX Cam | 69501070 | 69501069 | 1.06 | |
| HD 44179 | 70201801 | 70201904 | 1.00 | |
| IC 418 | 82901301 | 86801205 | 1.03 | |

If we exclude from the analysis four objects showing calibration problems in band 4 of SWS (those presenting strong mismatches with band 3, indicated in Table 2.1), we can see that the mean LWS/SWS ratio derived from these measurements is <LWS/SWS> = 1.01, very close to unity, with a very little dispersion around this value (in most cases the agreement is at the 10% level or better). This is remarkable, if we consider that LWS and SWS were calibrated in a totally different way (LWS calibration is based on Uranus as primary calibrator while SWS band 4 calibration is mainly based on the results of ground-based ILT experiments using blackbody sources).

As a byproduct of this analysis and since some of the objects in this cross-calibration sample were repeatedly observed throughout the mission with either SWS or LWS, it was also possible to perform an independent analysis of the stability of both instruments in terms of absolute flux calibration. The results obtained indicate that both for LWS and SWS the reproducibility was better than 15% in all cases.

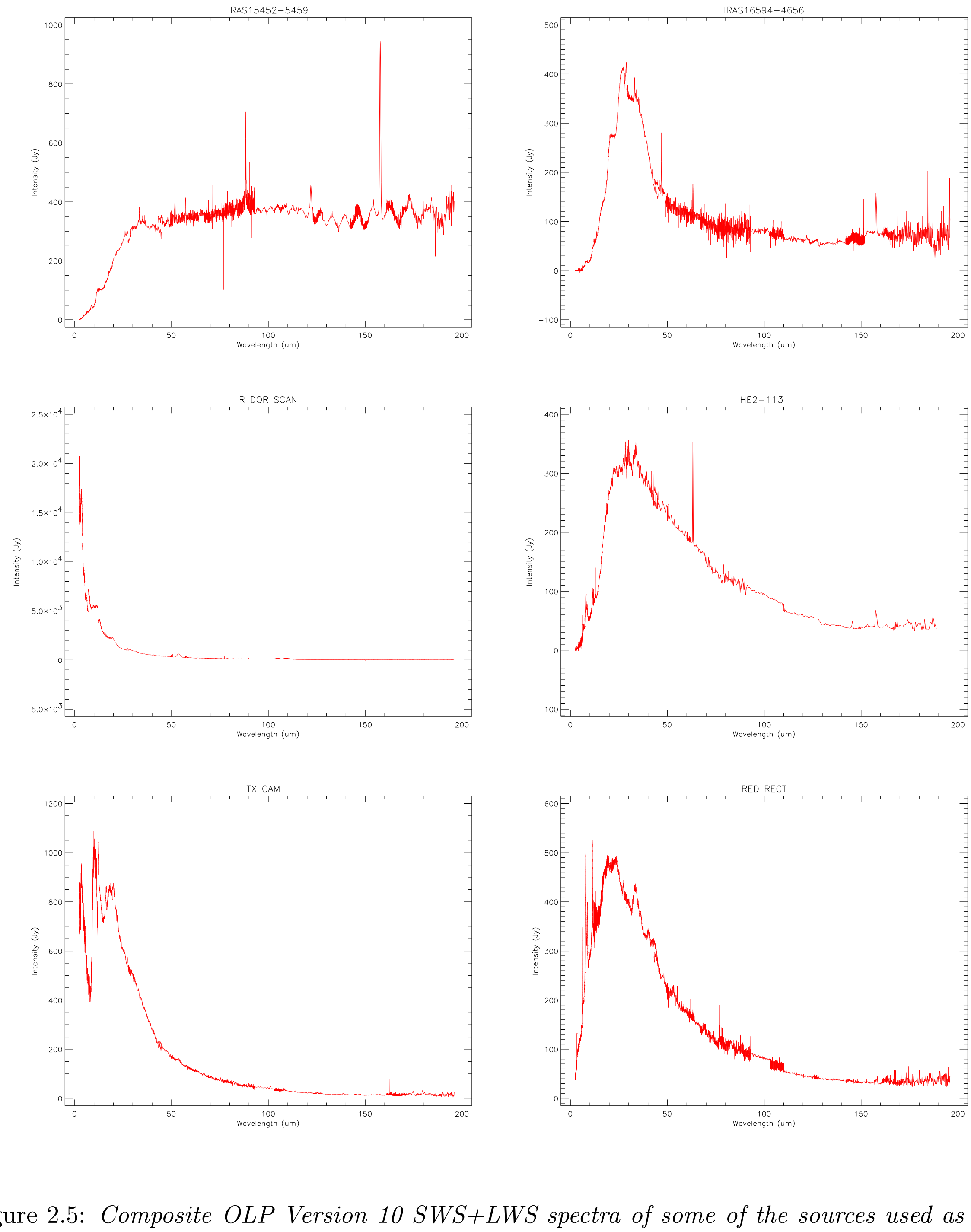


Figure 2.5: *Composite OLP Version 10 SWS+LWS spectra of some of the sources used as test cases for the consistency check between SWS and LWS. Note the excellent match at 44 μm in most cases.*

## 2.2 Filter measurements versus spectroscopy

### 2.2.1 ISOCAM filters versus chopped PHT-S

An excellent agreement is also found when comparing ISOCAM filter measurements with PHT-S spectroscopy. As an example of this, we present here the results obtained from a cross-calibration comparison performed at a very low flux level (a few mJy) of ISOCAM filter photometry (AOT CAM01) and PHT-S spectroscopy (AOT PHT40) of a sample of 55 Seyfert galaxies reported in Schulz et al. 2000, [43]. Seyfert galaxies in the sample were observed both with ISOCAM LW2 (6.7 $\mu$m) and LW7 (9.6 $\mu$m) filters and with chopped PHT-S photometry.

In this case, however, the comparison is not based on OLP Version 10 data products. Instead, calibration was performed using standard CIA and PIA routines starting from ERD. Manual recalibration of the spectra included only glitch de-tailing and transient correction of the chopped PHT-S measurements in a similar way as the Version 10 of the automated pipeline does it. Thus, the expected level of agreement reached in the final products is very similar.

In Figure 2.6 we can see two nice examples of PHT-S and ISOCAM filter measurements of the Seyfert galaxies Markarian 509 (Seyfert 1) and NGC 5953 (Seyfert 2).

The results obtained are very satisfactory since the global median flux ratio (ISOCAM filter/PHT-S) derived from the measurements is: 1.15 for the LW2 measurements and 0.94 for LW7, i.e. ISOCAM flux densities without colour correction are only 15% higher in LW2 and 6% lower in LW7 than the corresponding PHT-S measurements.

The colour correction for the large bandpass-filter could explain the difference for LW2 up to 10%, as the spectral energy distribution of the Seyfert galaxies observed are red, and with the PAHs contribution in the reddest part of the filter wavelength range. On the other hand, the higher fluxes detected in the LW2 5–8.5 $\mu$m filter might also be contaminated by the contribution from the stellar content of the underlying extended galaxy which may still be detectable even for the almost point-like Seyferts, the ISOCAM aperture being wider than the PHT-S one.

### 2.2.2 ISOCAM filters versus SWS

Observations of the Orion bar complex made with CAM-CVF and SWS by Cesarsky et al. 2000, [3] are shown here as an example of this cross-calibration analysis. The spectrum of this region of the sky shows a combination of strong emission features corresponding to PAHs and amorphous silicate grains together with narrow emission lines coming from an ionised region around the isolated O9.5 V star $\Theta^2$ Ori A, as we can see in Figure 2.7.

The simultaneous presence of broad and narrow emission features makes this comparison quite interesting for cross-calibration purposes since it constitutes an excellent laboratory to test the internal consistency of ISO calibration in the presence of emission lines.

The CAM-CVF observations employed the 6" per pixel field of view of ISOCAM. Full scans of the two CVFs in the LW channel of the camera were performed with both increasing and decreasing wavelength. The results of these two scans are almost identical, showing that the transient response of the detector was only a minor problem for these observations. The raw data were processed using CIA in a standard way and the Fouks-Schubert transient correction was applied to the data resulting in only minor corrections. The CAM-CVF spectrum of $\Theta^2$ Ori shown in Figure 2.7 was obtained co-adding all the pixels falling within the SWS aperture.

The full range (2.4 to 46 $\mu$m) SWS spectrum of the HII region surrounding the star $\Theta^2$ Ori A was reduced with SIA using version 30 of the Cal-G files.

Since the interactive data reduction performed was done in a similar way as Version 10 of the pipeline does it both for ISOCAM and SWS data, the level of agreement reached is expected to

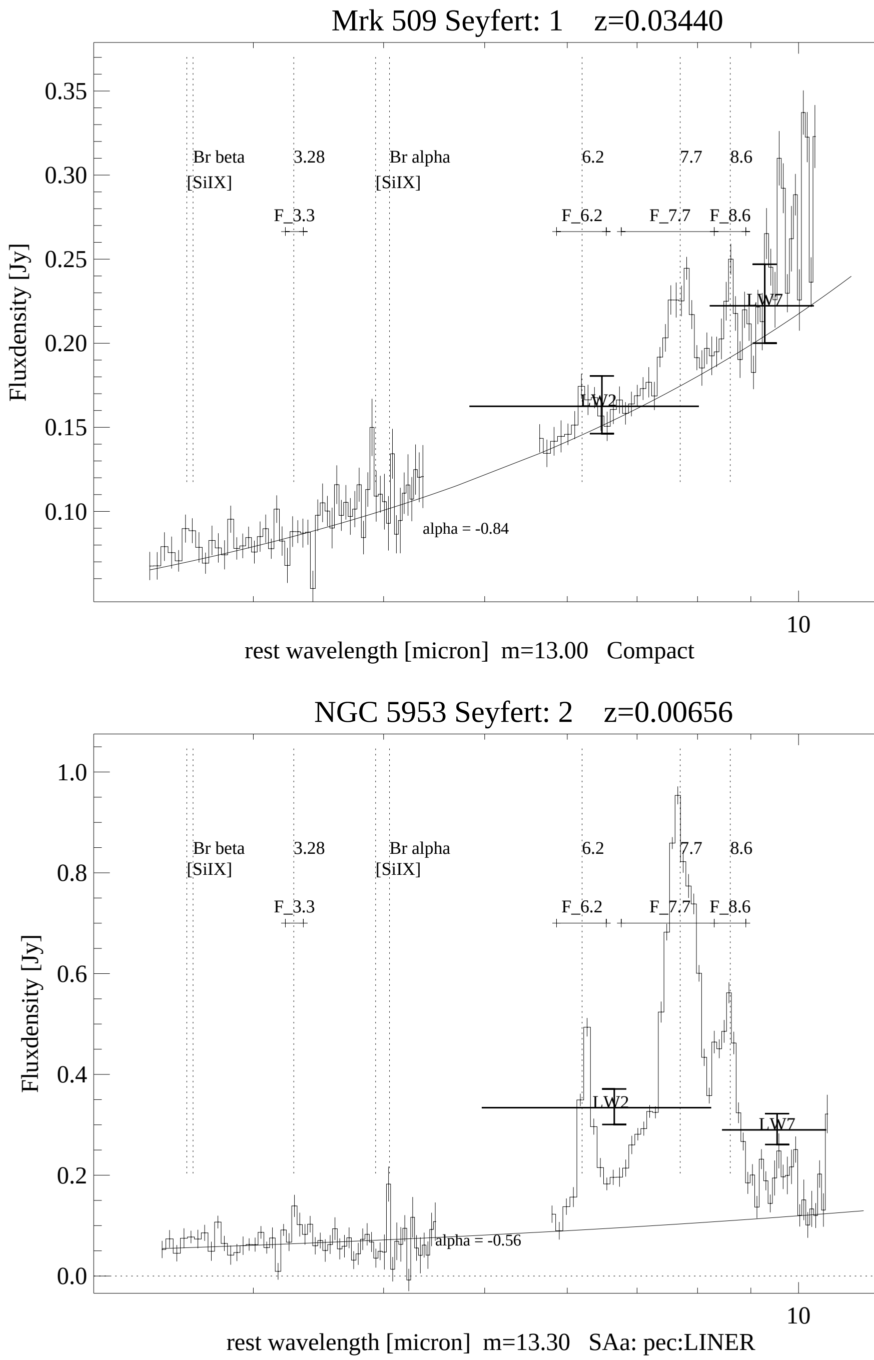


Figure 2.6: *PHT-S spectrum and ISOCAM LW2 and LW7 filter measurements of the Seyfert 1 galaxy Mrk 509 and of the Seyfert 2 galaxy NGC 5953. The position of some of the more prominant PAH bands and emission lines are indicated. The two large crosses marked LW2 and LW7 indicate the flux from ISOCAM images with its error and wavelength range. The best fit power-law continuum is shown as a continuous line (taken from Schulz et al. 2000, [43])*

be comparable to that obtained using OLP data products. And this was actually found to be excellent, within 20% both for the continuum and for the emission lines.

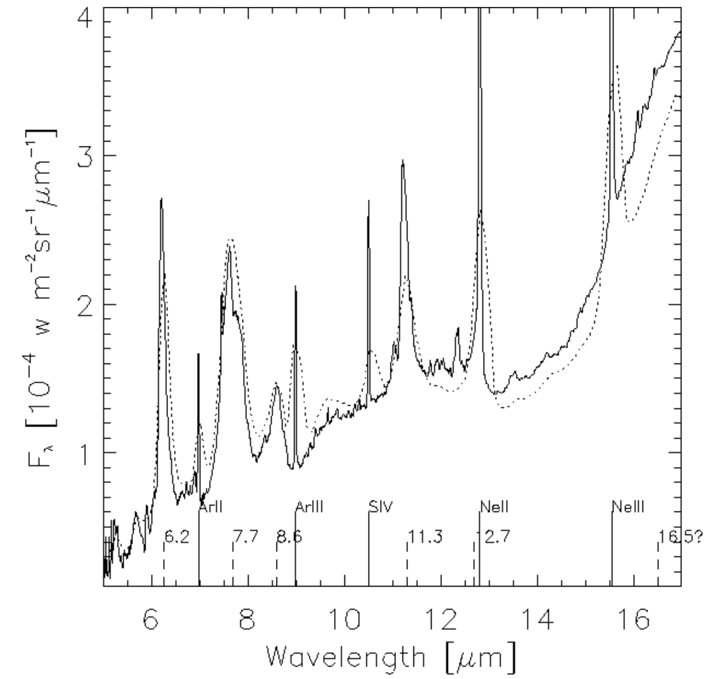


Figure 2.7: *SWS spectrum (full line) compared to the CAM-CVF spectrum (dotted line) of the region around $\Theta^2$ Ori A. All the ISOCAM pixels falling in the SWS aperture have been co-added (from Cesarsky et al. 2000, [3]).*

### 2.2.3 ISOPHOT filters versus ISO spectroscopy

Observations of comet Hale-Bopp taken in October 1996 with ISOPHOT using 4 different detectors (P1, P2, C100 and C200) and 10 filters covering the range between 3.6 and 170 $\mu$m by Grün et al. 2001, [19] have been compared with quasi-simultaneous observations taken with PHT-S (Crovisier et al. 1997, [10]), SWS (Crovisier et al. 2000, [11]) and LWS (Lellouch et al. 1998, [35]).

Figure 2.8, taken from Grün et al. 2001, [19] shows the ISOPHOT photometric fluxes together with the PHT-S, SWS and LWS spectra taken on 6–7 October 1996, scaled to a 19$''$ aperture. This required the application of aperture correction factors which assumed a $1/\rho$ brightness distribution, where $\rho$ is defined as the projected distance from the nucleus. Details on the data reduction of each dataset used in this cross-calibration comparison can be found in the above referenced paper.

In the case of the ISOPHOT filter measurements, background observations were performed with identical instrument settings at the same positions on the sky several days after the comet observations to subtract the contribution from the sky emission to the on-source photometric measurements. All observations were done in single pointing, single filter absolute photometric mode (PHT05 and PHT25).

A reasonable agreement was found between the independently calibrated photometry and spectroscopy in most cases in spite of the many different correction factors applied to the data. These correction factors are needed in the case of ISOPHOT to cope with the different apertures used per filter, positional offsets (observations where the source was not perfectly centred in the aperture), PSF effects on coma measurements, and the usual colour corrections. For SWS, additional scaling factors were applied to the different bands to make the spectrum continuous; these scaling factors were always close to one.

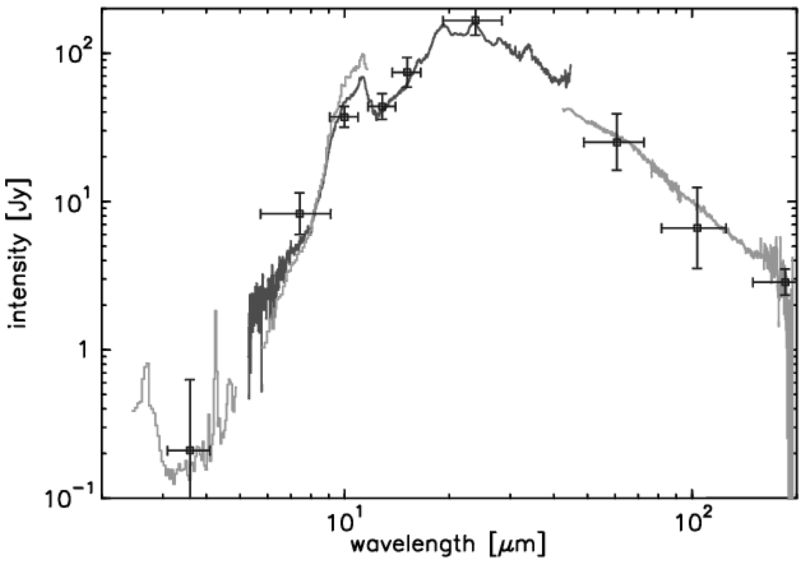


Figure 2.8: *Comparison of ISOPHOT photometry (open squares) and the PHT-S, SWS and LWS spectra of Comet Hale-Bopp on 6–7 October 1996. All fluxes have been scaled to a 19′ diameter aperture.*

### 2.2.4 ISOPHOT filters versus LWS

We present here the results obtained from the cross-calibration analysis performed at the long wavelength spectral range covered by ISO between 60 and 200 $\mu$m using a combination of PHT-C measurements and LWS01 observations.

As it has already been mentioned before, this comparison is difficult because of the limited common dynamic range and the lack of astronomical sources observed both with PHT-C and LWS suitable for cross-calibration.

Searching the ISO Data Archive it is possible to select around 200 different positions in the sky where ISO observations were performed both with PHT-C filters (photometry beyond 60 $\mu$m) and LWS01, corresponding to about 100 different astronomical sources. However, there are very few of them with both PHT and LWS observations of enough quality to derive reliable numbers. In addition, the strong infrared background sometimes completely dominates the measurements especially at the longest wavelengths making cross-comparisons more difficult.

Moreover, we need to purge as usual this cross-calibration sample for bad-pointed observations, variable and extended sources, which at the end limits the number of suitable sources to just 9 common observations which are presented in Tables 2.2 and 2.3. These were the observations selected as test cases for this cross-calibration analysis.

For the derivation of the fluxes quoted in Tables 2.2 and 2.3 we retrieved from the ISO Data Archive the OLP Version 10 PHT-C photometric data together with the corresponding OLP Version 10 LWS spectra. In the case of the PHT-C photometry we just took directly the values provided by the automated pipeline while the LWS spectra were further processed with ISAP Version 2.1 in order to derive the equivalent 'synthetic photometry' at 60, 100, 120, 150 and 200 $\mu$m.

For this we used the `syn_phot` application in ISAP, which allows the convolution of the ISO LWS spectrum with the transmission profile of the different IRAS PHT-C filters used in the comparison. The programme assigns a monochromatic flux at each of these wavelengths as output under the assumption that the source SED shape is of the form $\nu \times f_\nu$ = constant, or equivalently $\lambda \times f_\lambda$ = constant, in the same way as PHT-C calibration did.

Table 2.2: *List of cross-calibration sources used in the comparison between PHT-C100 and LWS*

| Source | C100 60 $\mu$m | C100 100 $\mu$m | C100 120 $\mu$m | LWS 60 $\mu$m | LWS 100 $\mu$m | LWS 120 $\mu$m | IRAS $CIRR2$ |
|---|---|---|---|---|---|---|---|
| CRL 3068 | - | - | 70.0 | - | - | 67.0 | 1 |
| Y CVn | 21.0 | 10.5 | - | 14.6 | 8.3 | - | 1 |
| HD 161796 | - | - | 54.8 | - | - | 54.1 | 1 |
| R Cas | 102 | 38.5 | - | 85.5 | 32.9 | - | 2 |
| IRAS 16342−3814 | - | - | 269 | - | - | 146 | 4 |
| OH104.9+2.4 | 84.5 | 63.0 | - | 89.2 | 44.6 | - | 5 |
| $\chi$ Cyg | 92.8 | 50.5 | - | 82.3 | 36.6 | - | 5 |
| $\mu$ Cep | 112.5 | 64.0 | 177.5 | 108.5 | 52.9 | 39.0 | 5 |
| VX Sgr | - | - | 1240 | - | - | 205 | 6 |

Table 2.3: *List of cross-calibration sources used in the comparison between PHT-C200 and LWS*

| Source | C200 150 $\mu$m | C200 200 $\mu$m | LWS 150 $\mu$m | LWS 200 $\mu$m | IRAS $CIRR2$ |
|---|---|---|---|---|---|
| CRL 3068 | 43.0 | 23.0 | 36.5 | 24.4 | 1 |
| Y CVn | 11.7 | 7.3 | 3.0 | 5.0 | 1 |
| HD 161796 | 31.2 | 17.2 | 17.4 | 19.1 | 1 |
| R Cas | 52.7 | 37.9 | 13.3 | 4.7 | 2 |
| IRAS 16342−3814 | 221 | 171 | 97.0 | 70.5 | 4 |
| OH104.9+2.4 | 246 | 270 | 33.2 | 35.3 | 5 |
| $\chi$ Cyg | 161 | 136 | 33.3 | 46.8 | 5 |
| $\mu$ Cep | 179.5 | 147.5 | 25.8 | 18.3 | 5 |
| VX Sgr | 1640 | 1210 | 216 | 229 | 6 |

In Tables 2.2 and 2.3 the sources have been sorted according to the increasing value of the parameter *CIRR2* as quoted in the IRAS Point Source Catalogue Version 2.1. This is a logarithmic function which describes the contamination expected from background cirrus emission at 100 $\mu$m and responds to the equation:

$$CIRR2 = int[(8/3) \times log(F_c/F_s) + (19/3)] \tag{2.1}$$

where $F_c$ is the cirrus flux and $F_s$ is the source flux (see the *IRAS Explanatory Supplement*, [28]). A value of *CIRR2*=1 corresponds to the cirrus flux being less than 1% of the source flux while *CIRR2* larger than 5–6 indicates that the flux measurement is probably dominated by the cirrus contribution.

The cirrus contamination effect has clearly been detected in the cross-calibration measurements shown in Tables 2.2 and 2.3, especially beyond 100 $\mu$m.

While the consistency between PHT-C and LWS is better than 20–30% in most cases at 60 and 100 $\mu$m (detector C-100), we can see that at longer wavelengths (detector C-200) the situation becomes worse and this good level of agreement is only reached by the sources showing a very low value of the *CIRR2* parameter (and not always). For the rest of the sources in the short list under analysis the cirrus contamination completely dominates the flux detected at 120, 150 and 200 $\mu$m. This is clearly reflected by the fact that the flux ratios PHT-C/LWS at these wavelengths closely approach a constant value (between 6 and 8) which is a pure consequence of the difference in size of effective apertures between both instruments.

A similar analysis was carried out by Müller & Lagerros 2002, [40] using a combination of LWS01 grating scans and LWS02 fixed grating observations on a number of asteroids. For this cross-calibration comparison further processing of OLP Version 10 data products was performed using ISAP Version 2.0.

In the case of LWS01 grating scans the detector signals were deglitched, $\sigma$-clipped (2.5 $\times$ r.m.s.) and averaged. Detectors SW1 to SW5 were then smoothed with the nominal resolution element of 0.29 $\mu$m, LW1 to LW5 with a resolution element of 0.6 $\mu$m and both scan directions averaged. Observations on a large number of standard sources (planets, asteroids, stars) have shown that the responsivities of the detectors LW1, LW2 and LW3 might be flux dependent. In order to correct for these suspected non-linearities empirical correction values were derived and applied to the asteroid scans (Müller 2001, [38]). The background values were taken from COBE/DIRBE (Hauser et al. 1998a, [23]) weekly maps (25–100 $\mu$m) and yearly maps (140–240 $\mu$m). LWS solid angles and correction factors for extended sources were taken from the ISO Handbook Volume III on LWS, [20]. Maximal background contributions were 4% for Ceres and up to 50% for Hygiea with the largest influence at long wavelengths.

For the fixed grating LWS02 observations the data reduction was also performed manually taking only the last 100 s of the measurements where the signals were usually stabilised. Dark current subtraction and flux calibration was done in the ISAP command mode. The detector non-linearities and the backgrounds were corrected in the same way as for the LWS01 mode. Maximal background contributions were up to 16% for Ceres, up to about 10% for Pallas and Vesta and up to 40% for Hygiea. The dark current signals in LW4 (160.6 $\mu$m) and LW5 (178.0 $\mu$m) were in many cases unstable during the integration times and the corresponding fluxes could therefore not be used.

The ISOPHOT observations were calibrated against standard stars and planets only with the help of PIA, using 'ad-hoc' Cal-G files excluding intentionally all the asteroids from them (they are also considered calibration standards for ISOPHOT), and treating the asteroid measurements this way as independent scientific observations.

All these observations were compared with thermophysical models of the asteroids (Müller & Lagerros 2002, [40] and references therein), which consider aspects like size, albedo and shape together with the spin vector, a beaming model, thermal inertia and a wavelength-dependent emissivity.

The observations/model ratios are shown in Figures 2.9 to 2.12. It may be interesting to remark here that this cross-calibration comparison comprises a large variety of observing geometries, aspect and phase angles, typically 2–3 orders of magnitude in flux and different background conditions for each asteroid. The observation from the 2 instruments (LWS, ISOPHOT) were taken in different observing modes (LWS01, LWS02, PHT22, PHT25, PHT99) and quite different integration times. They underwent completely different data processing and calibration schemes. Nevertheless, the observations/model representation gives a consistent picture, expressed in ratios close to one. In general no systematic offsets on absolute terms between the instruments or observing modes can be seen with the exception of the well known flux underestimation of the SW1 detector of LWS for observations taken before revolution 237 (some of which are represented in the plots as outliers), corrected in the final Version 10.1 of the LWS pipeline, and a few residual jumps betwen detector bands which are not yet fully understood.

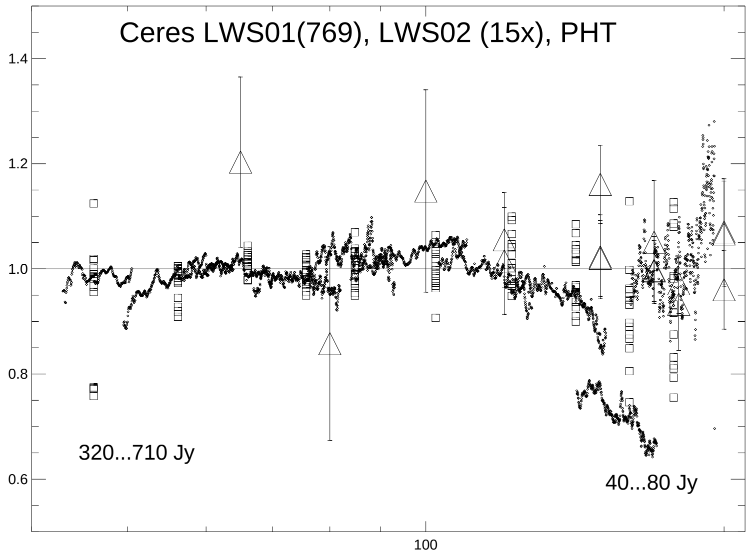


Figure 2.9: *LWS (fixed grating: squares; grating scans: dots) and ISOPHOT (triangles) observations of Ceres divided by its thermophysical model. A few LWS-SW1 fixed grating observations taken before revolution 237 are visible in the plot as outliers as well as a few measurements taken with the LWS-LW4 and LWS-LW5 detectors. No other systematic differences between LWS and ISOPHOT can be seen (from Müller & Lagerros 2002, [40]).*

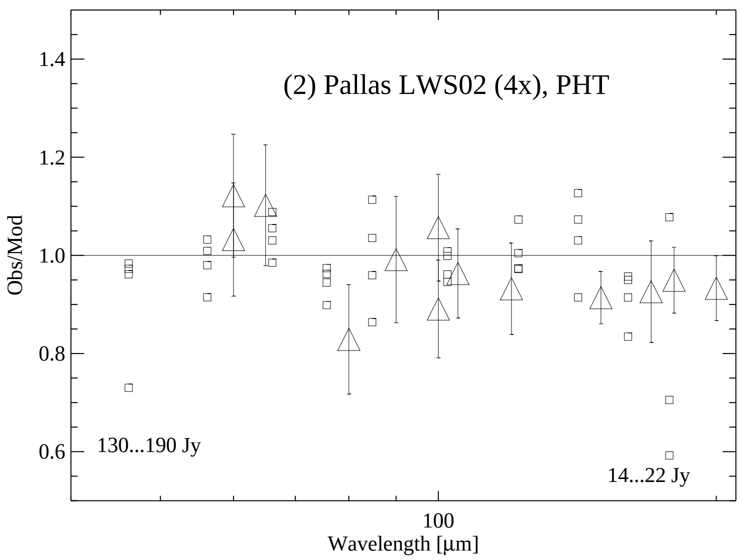


Figure 2.10: *LWS (fixed grating: squares) and ISOPHOT (triangles) observations of Pallas divided by its thermophysical model. Only one LWS-SW1 fixed grating measurement taken before revolution 237 and a couple of individual LW5 measurements show strong discrepancies with respect to the ISOPHOT data and/or the thermophysical model (from Müller & Lagerros 2002, [40]).*

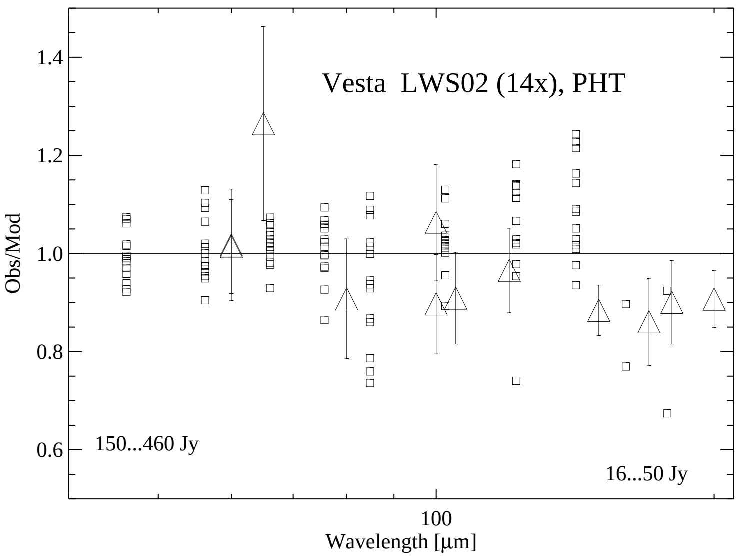


Figure 2.11: *LWS (fixed grating: squares) and ISOPHOT (triangles) observations of Vesta divided by its thermophysical model. Again, with the exception of a few measurements at the longest wavelength range, no strong systematic differences between LWS and ISOPHOT can be seen (from Müller & Lagerros 2002, [40]).*

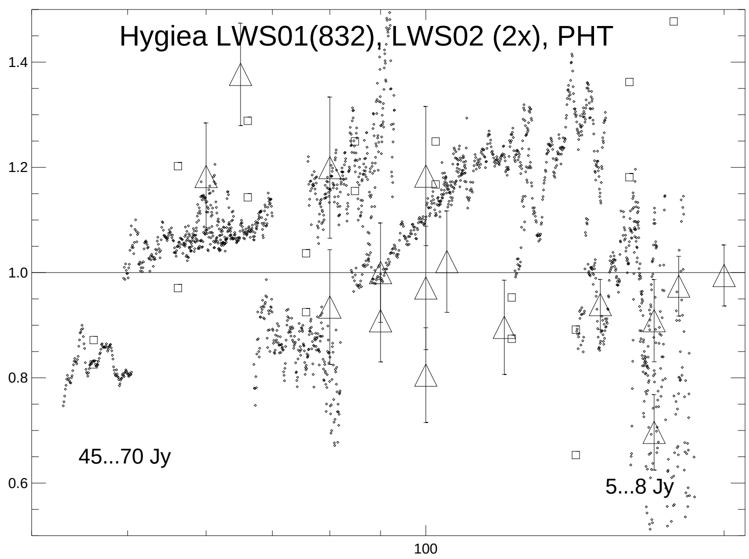


Figure 2.12: *LWS (fixed grating: squares; grating scans: dots) and ISOPHOT (triangles) observations of Hygiea divided by its thermophysical model. Note the ∼20% discrepancy of the LWS-SW1 measurements, both taken before revolution 237. Other jumps between LWS bands are calibration artifacts. Especially the high quality ISOPHOT C200 measurements are consistent with the model predictions. Note that the flux level in this case is of only a few Jy at the longest wavelength range, close to the detection limit for LWS (from Müller & Lagerros 2002, [40]).*

# Chapter 3

# External Cross-Calibration

## 3.1 Comparison with IRAS

### 3.1.1 SWS versus IRAS photometry

A large number of astronomical sources observed with SWS were also detected by IRAS at the 12 and 25 $\mu$m bands and are included in the IRAS Point Source Catalogue.

In order to compare the absolute flux calibration of IRAS and ISO SWS we searched the ISO Data Archive for observations made with ISO at the same positions of the sky, allowing a maximum offset of $1.5'$. This way, we found up to 556 different pointings in the ISO Data Archive containing SWS01 observations corresponding to around 400 different IRAS sources.

Unfortunately, many of the sources in this sample had to be discarded because they were known to be slightly extended sources or strongly variable. Extended sources may introduce uncertainty in the results; first, because the SWS calibration is based on point source flux calibration and correction factors are needed to derive their actual absolute flux and, second, because many of these extended sources are usually located in areas of the sky with a complex structure at infrared wavelengths, which complicates even more the problem.

Sources which look extended to SWS are easily recognised because the spectra show strong flux jumps between bands coincident with changes in the aperture size, as we have already shown in Figure 1.1 (bottom panel).

Concerning variability, we know that many of the stars observed by ISO are characterised by their strong photometric variability. Many of them are pulsating stars in the Asymptotic Giant Branch (AGB) phase evolving into planetary nebulae. Some others are young stellar objects which may also be variable (although in this case the amplitude of the variations in this spectral range is usually not very large).

In spite of all these limitations, we ended up with a list of still more than 250 individual observations susceptible to be used for cross-calibration with the IRAS photometry at 12 and 25 $\mu$m, corresponding to more than 100 different astronomical sources, covering a wide range of spectral shapes and brightness.

Each of these 250 individual OLP Version 10 SWS spectra were retrieved from the ISO Data Archive and further processed with ISAP Version 2.1. Basically, bad data points affected by glitches were identified and removed from the spectra using the available tools in ISAP and what we can call 'ISO SWS photometry' was performed at 12 and 25 $\mu$m with the help of the `syn_phot` application of ISAP, which simply convolves the ISO spectrum with the transmission profile of the IRAS filters at 12 and 25 $\mu$m and assigns a monochromatic flux at these two wavelengths under the assumption that the source SED shape is of the form $\nu \times f_\nu$ = constant, or equivalently $\lambda \times f_\lambda$ = constant, in the same way as IRAS did.

In Figure 3.1 we show the results obtained at 12 $\mu$m. At first sight, the conclusion is that, in general, ISO SWS synthetic photometry and IRAS photometry at 12 $\mu$m are consistent within the 15% level in most cases independent on the flux level considered (from few Jy to several thousand Jy), with only a few sources showing a slightly worse agreement (∼25–30%) at low flux levels (below 25 Jy).

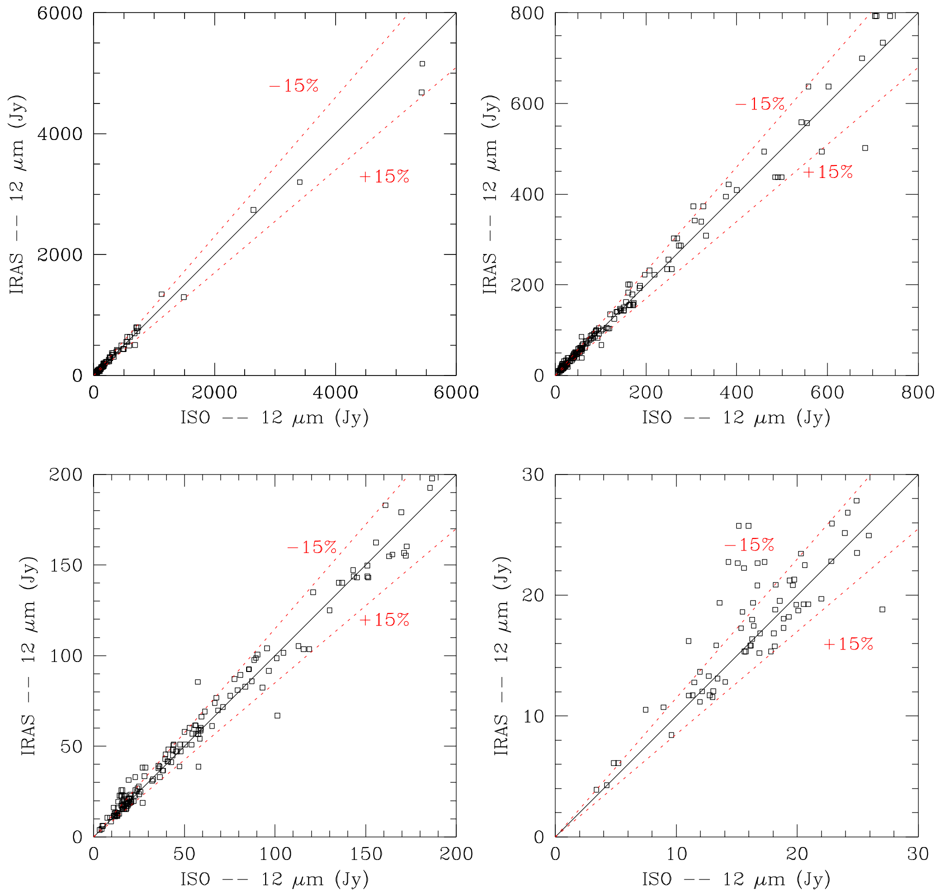


Figure 3.1: *ISO SWS synthetic photometry at 12 µm derived from OLP Version 10 data products compared to IRAS photometry at the same wavelength. The dashed red line represents a 15% discrepancy level*

Figure 3.3 (left panel) shows the distribution of the discrepancies found between the ISO SWS synthetic photometry and IRAS photometry at 12 $\mu$m. Taking the mean absolute flux level of all the measurements taken with SWS and IRAS at 12 $\mu$m the zero-point consistency is found to be better than 2%.

Note that the overall distribution is, however, slightly asymmetric. In the absence of other known calibration problems, the few obvious outliers towards positive values (ISO fluxes overestimated with respect to IRAS) might correspond to variable sources not recognized as such in the sample (and, thus, not purged) detected close their maximum brightness by ISO, while those towards negative values (ISO fluxes underestimated with respect to IRAS) are interpreted as a combination of previously unknown variable sources (caught this time during minimum brightness by ISO) and slightly bad-pointed observations which have partially escaped from detection.

A very similar result is obtained at 25 $\mu$m, as we can see in Figure 3.2. The level of agreement is again in most cases within 15% for strong sources (above 50 Jy), with very few exceptions, although it becomes also slightly worse for low flux levels (typically within 25–30% for fluxes below 15–20 Jy). Comparing the absolute flux level of all the measurements performed with SWS and IRAS at 25 $\mu$m the zero-point consistency is found to be better than 1% (for the derivation of this number, the measurements at 25 $\mu$m corresponding to sources with an absolute flux level at this wavelength below 15 Jy were excluded).

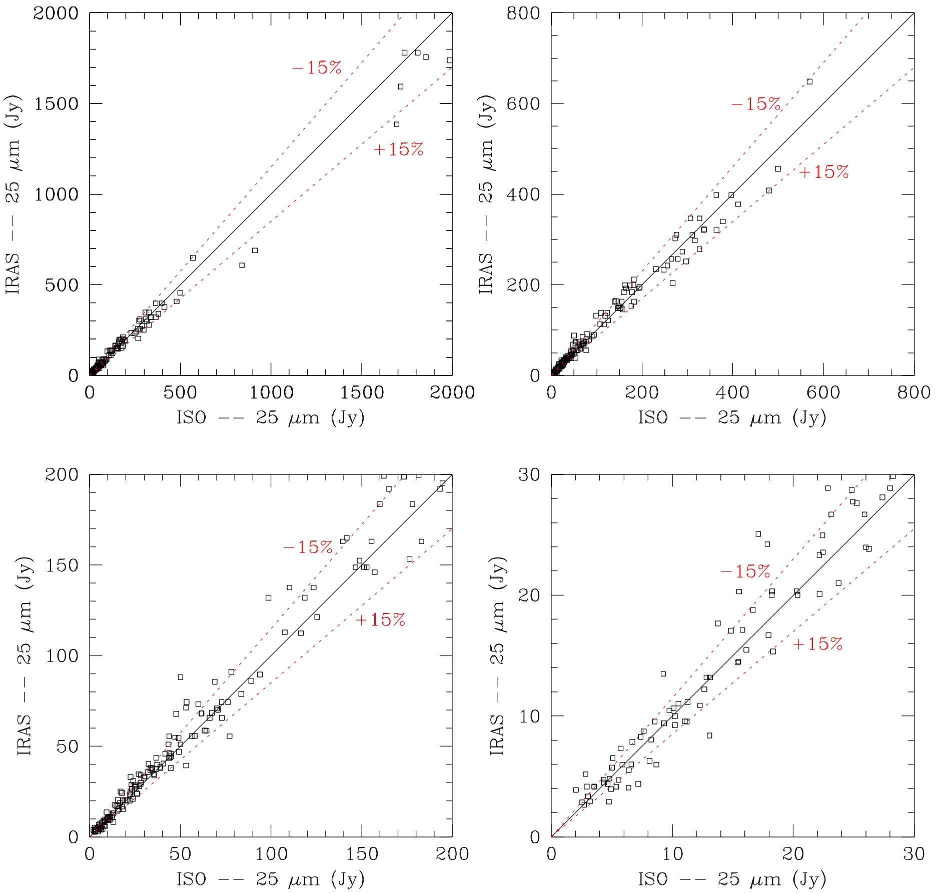


Figure 3.2: *ISO SWS synthetic photometry at 25 $\mu$m derived from OLP Version 10 data products compared to IRAS photometry at the same wavelength. The dashed red line represents a 15% discrepancy level.*

In this case, however, the overall distribution of discrepancies plotted in Figure 3.3 (right panel) is not asymmetric, in contrast with what was found at 12 $\mu$m. The number of strongly underestimated fluxes by ISO with respect to IRAS are in this case more or less similar to the number of overestimations. The few obvious outliers at both sides of the distribution are actually the same sources observed as outliers at 12 $\mu$m supporting the hypothesis that they may be variable stars. Thus, we interpret the symmetry observed in this case as the consequence of the smaller number of badly pointed observations at this wavelength, probably because of the larger apertures used by SWS bands 3 and 4, which lowers the probability of missing part of the incoming flux from a point source when it is observed slightly off-axis.

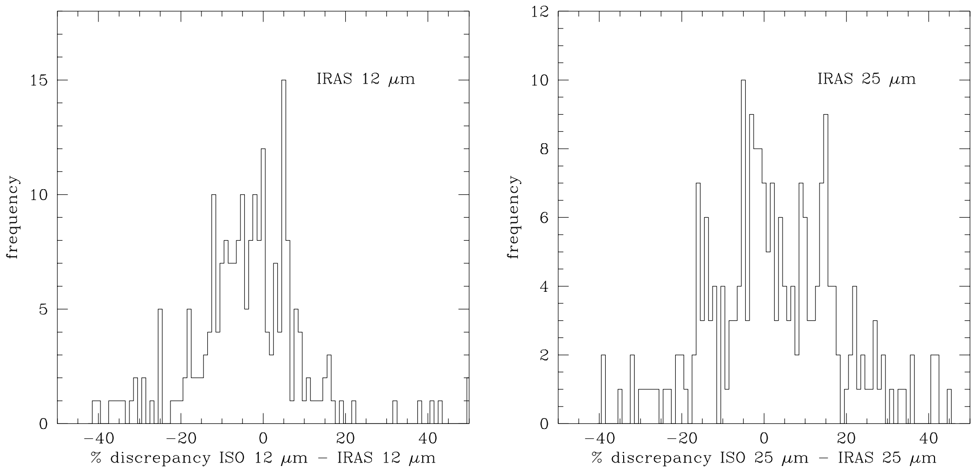


Figure 3.3: *Distribution of the discrepancies found between the ISO SWS synthetic photometry at 12 $\mu$m (left) and 25 $\mu$m (right) derived from OLP Version 10 data products compared to the IRAS photometry*

### 3.1.2 LWS versus IRAS photometry

A similar analysis was performed by Chan et al. 2001, [4] considering all sources observed with ISO LWS in the grating scan mode (LWS01 AOT) for which there was also available photometry at 100 $\mu$m in the IRAS Point Source Catalogue.

In order to compare the absolute flux calibration of IRAS and ISO LWS the ISO Data Archive was searched for observations made with ISO at the same positions of the sky, allowing a maximum offset of $2'$. The objects were selected according to the additional following criteria:

1. IRAS flux density qualities $\geq$2 in the 60 and 100 $\mu$m bands
2. LWS data showing no fringes — to avoid sources with a strong cirrus background and/or extended objects
3. $F_\nu$(100 $\mu$m) $<$ 1000 Jy — to avoid detector non-linearities
4. $F_c/F_s < 0.5$, where $F_c/F_s$ is the flux density ratio of cirrus and source
5. IRAS CIRR3 $\leq$ 254 MJy/sr and no strong cirrus background on the IRAS Sky Atlas Maps or in the LWS parallel maps at 100 $\mu$m (LW1 detector).
6. source is not a known variable source

A total number of 170 different pointings were found in the ISO Data Archive containing LWS01 observations satisfying the above criteria corresponding to 120 different IRAS sources. They all were included in this cross-calibration analysis as test cases, covering a wide range of spectral shapes and brightness.

The OLP Version 10 LWS grating spectra were retrieved from the ISO Data Archive and further processed with ISAP Version 2.1 prior to their comparison with the IRAS photometry at 100 $\mu$m. Bad data points affected by glitches were removed from the spectra using the available tools in ISAP. A few sources had to be corrected also for the so-called ‘near-infrared leak’. This is an instrumental effect which produces false strong features at $\sim$53 $\mu$m and $\sim$105 $\mu$m on the LWS spectra of sources with a bright near infrared counterpart. These features can easily be removed by fitting a power-law to the underlying continuum and assuming they have a Gaussian profile, which is a very good aproximation to their real shape (see ISO Volume III of the Handbook on LWS, [20] for more details).

ISAP was also used to perform the equivalent 'ISO LWS photometry' at 100 $\mu$m of all the 120 sources contained in our new cross-calibration sample. This was done using again the `syn_phot` application, which convolves the ISO spectrum with the transmission profile of the IRAS 100 $\mu$m filter. This assigns a monochromatic flux at this wavelength under the assumption that the source SED shape is of the form $\nu \times f_\nu$ = constant, or equivalently $\lambda \times f_\lambda$ = constant, in the same way as IRAS did.

The main problem which affects our cross-calibration comparison is the cirrus contamination. The infrared sky is characterised by emission at 100 $\mu$m from interstellar dust on all spatial scales. In spite of the restrictions applied to the selected sources, a significant chance exists that some of them can still be affected by components of this long-wavelength emission on point source scale. While the IRAS photometric fluxes quoted in the Point Source Catalogue are already corrected for this background 'cirrus' emission, this is not the case of the photometry derived from LWS data, which includes this background contribution. Therefore, it is necessary to apply a correction either to LWS data or to the IRAS photometry before making any cross-calibration comparison.

Two methods can be applied to perform this 'cirrus correction'. Both recovery procedures are only an approximation:

- **Method 1:** based on the restoration of the original IRAS flux density at 100 $\mu$m uncorrected for cirrus (i.e. $F_c + F_s$) using the value of *CIRR2* listed in the IRAS Point Source Catalogue, which is directly related via Equation 2.1 to the value of $F_c/F_s$. As we have already mentioned in Section 2.2.4 *CIRR2* is an integer in the range from 1 to 9. *CIRR2* values less than 4 indicate little or no cirrus contamination. *CIRR2* values larger than 5 indicate the presence of bright cirrus emission heavily contaminating the source photometry.

- **Method 2:** based on the removal of the cirrus contamination from the ISO-LWS synthetic photometry using the CIRR3 values listed in the IRAS Point Source Catalogue. *CIRR3* is the total surface brightness of the sky surrounding a source in a 0.5° beam at 100 $\mu$m clipped to exclude values larger than 254 MJy/sr. LWS calibration is based on point sources, so those that sit on a significant background will require this correction before they can be compared with the IRAS photometric values in the Point Source Catalogue. To perform this correction requires the knowledge of the ISO LWS beam; that is, the effective solid angle of the LWS detectors and the so-called 'extended source correction factors', both of which are given in the ISO Handbook Volume III on LWS, [20]. The main problem of this whole procedure is that in regions with bright cirrus emission, the *CIRR3* value may overestimate grossly the true background flux local to the source.

Figure 3.4 shows the distribution of ISO/IRAS flux density ratios at 100 $\mu$m as a function of the IRAS flux density at 100 $\mu$m in a logarithmic scale using the two different methods above mentioned. The results obtained suggest that, in spite of the uncertainties induced by the sometimes large (and inaccurate) correction factors needed to make this comparison, there is a reasonable good agreement between ISO and IRAS at 100 $\mu$m in most cases (within 30%).

However, ISO flux calibration is found to give systematically 12.5% higher fluxes respect to IRAS (if we take the mean value), independent on the method used. A similar discrepancy (11.3%) was reported in the *LWS OLP Version 10 Scientific Validation Report* (Lim et al. 2001, [36]),

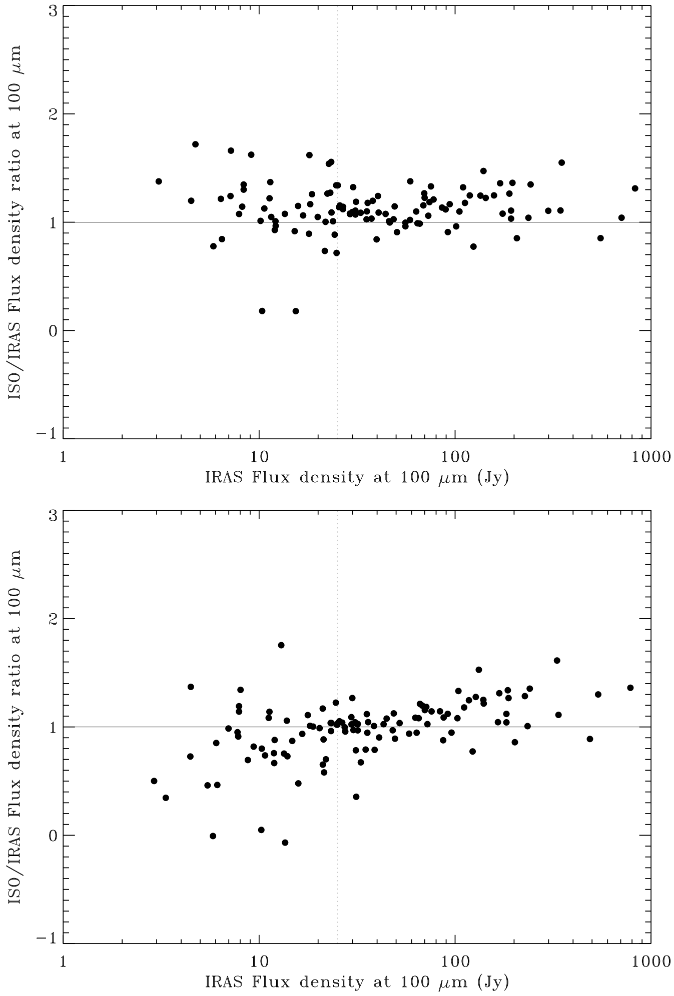


Figure 3.4: *The LWS/IRAS flux density ratios at 100 $\mu$m as a function of the IRAS flux density at 100 $\mu$m using Method 1 (top) and Method 2 (bottom). The vertical dashed line represents an arbitrary limit below which LWS accuracy becomes dominated by inaccurate dark current subtraction. Note the higher fluxes detected by ISO with respect to IRAS at high flux levels in both cases (from Chan et al. 2001, [4]).*

where the calculations were restricted to a short list of low background sources, suggesting that the problem is not related to a wrong background subtraction.

In order to analyse more in detail the problem we have plotted in Figure 3.5 the results of the same cross-calibration comparison in a linear scale and only including sources with IRAS flux densities at 100 $\mu$m below 100 Jy using Method 1. Interestingly, the distribution shows the existence of at least 2 different turning points leading to three different regimes. The first regime is followed by sources with ISO fluxes below 25 Jy. These are the sources showing the higher degree of consistency with ISO in terms of absolute flux level, although the dispersion is very high at these low flux levels, as expected, due to inaccurate dark current subtraction. A second regime is followed by sources well detected by ISO with fluxes at 100 $\mu$m between 25 and 75 Jy. These sources show systematically 10–15% higher ISO fluxes compared to IRAS with a dispersion of only 20%. And there seems to be even a third regime beyond 75 Jy which shows an even larger systematic discrepancy (up to 20%) with a similar dispersion. The same behaviour, although not shown here, is observed when we use Method 2.

The discontinuities observed are still of unknown origin and may be either in ISO or in IRAS

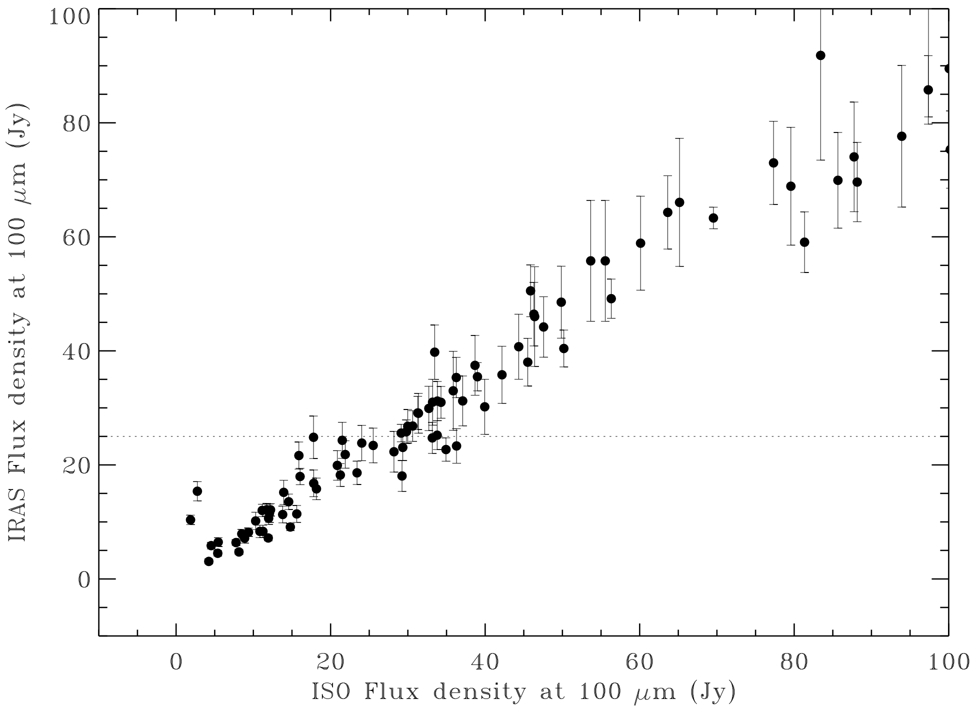


Figure 3.5: *ISO LWS synthetic photometry at 100 $\mu$m compared to IRAS photometry at the same wavelength for sources with IRAS flux density at 100 $\mu$m less than 100 Jy, using Method 1. The horizontal dashed line represents an arbitrary limit below which LWS accuracy becomes dominated by inaccurate dark current subtraction (taken from Chan et al. 2001, [4]).*

calibration. It is remarkable that the problem seems to be not related with inaccuracy at low flux levels induced by an inaccurate dark current subtraction since this would just increase the observed dispersion but it would not change the zero-point of the absolute flux calibration. Actually, the strongest discrepancies are observed in the group of the brightest sources.

Neither the problem seems to be directly correlated with the inaccuracy of the diferent methods use for cirrus correction, since it equally affects sources with low and high background, as we have already mentioned.

An interesting independent comparison between ISO LWS and IRAS photometry at 60 and 100 $\mu$m was carried out by Brauher & Lord 2001, [1] on a large sample of extragalactic sources.

This sample consisted of observations of galaxies taken with the LWS in the grating modes (LWS01 and LWS02) that were reduced in a uniform manner using all of the advanced data reduction techniques of LIA and ISAP starting from OLP Version 7 data products. The galaxy sample comprised nearly all galaxies observed during the ISO mission whose far-infrared emission fell within the 75$''$ LWS beam and had IRAS Point Source Catalogue detections. There were 155 such galaxies in the ISO Data Archive with 60 $\mu$m fluxes ranging from below 1 Jy to 300 Jy.

In this study, a small correction factor was introduced in the derivation of the ISO synthetic photometry at 60 $\mu$m with ISAP in order to account for the fraction of the IRAS 60 $\mu$m filter not covered by ISO LWS (27–87 $\mu$m is the spectral coverage of the IRAS 60 $\mu$m filter versus 43–197 $\mu$m for LWS). This may introduce some uncertainty in the derived values. Assuming that the majority of the galaxies used for this comparison span a narrow temperature range (30–45 K) the amount of the integrated flux measurement missed by LWS is estimated to vary from 2-8%. Thus, an average correction of 5% to the LWS 60 $\mu$m fluxes was applied to all the galaxies in the sample.

The LWS02 60 $\mu$m and 100 $\mu$m continuum fluxes must also have a secondary correction applied. The fluxes for this AOT were estimated by fitting a 2–5 $\mu$m linear baseline through the IRAS filter central wavelengths, essentially producing a monochromatic flux density. This flux density must be corrected to estimate the flux density IRAS found over its extended passband. Fitting a linear baseline to the spectra overestimates the integrated spectral photometry by 12% at 60 $\mu$m and 9% at 100 $\mu$m. Thus, the LWS02 fluxes were also corrected for these overestimations accordingly.

After these corrections were applied, the infrared sky background was estimated using IRSKY (images from the all-sky IRAS Survey Atlas with a resolution of 4′ in each of the IRAS bands) and then removed from the LWS data, in a similar way as Method 2 described above does it. The background subtracted LWS data were then compared with the IRAS photometry at 60 and 100 $\mu$m quoted in the Point Source Catalogue.

Figure 3.6 shows how the LWS and IRAS data compare after a careful reduction with the LWS Interactive Analysis software (LIA), including interactive dark currrent subtraction, absolute responsivity corrections, as well as manual removal of glitches and fringes.

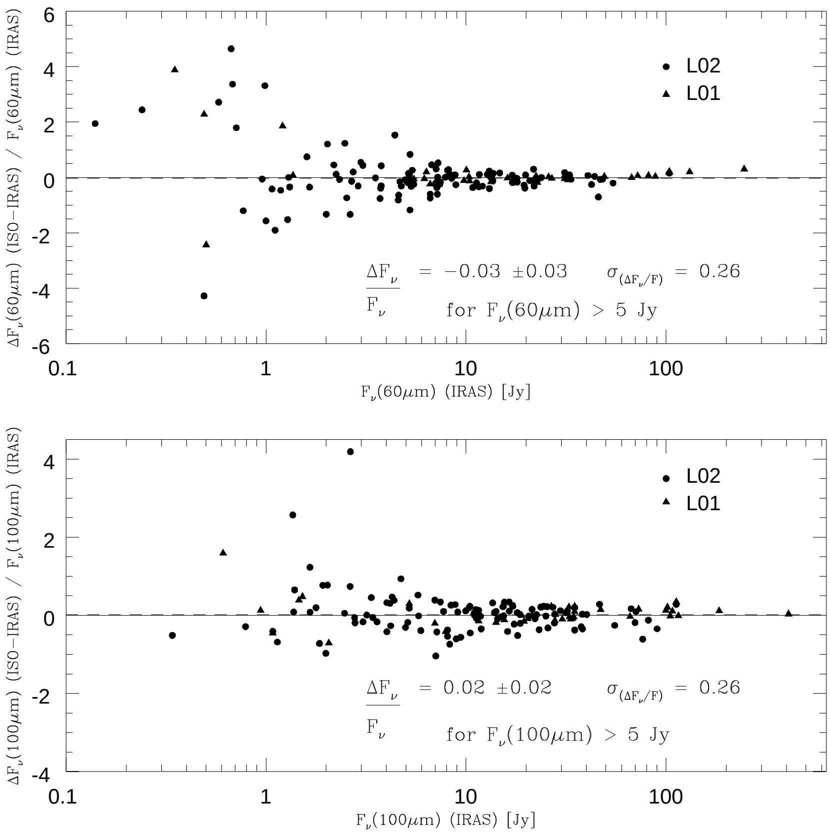


Figure 3.6: *The difference between the LWS and IRAS fluxes at 60 $\mu$m and 100 $\mu$m. The systematic offsets and dispersions of the LWS01 (triangles) and LWS02 (circles) data with respect to IRAS data are similar. The overall agreement is typically within 26% for fluxes above 5 Jy (from Brauher & Lord 2001, [1]).*

The results obtained suggests an overall good agreement between ISO LWS and IRAS both at

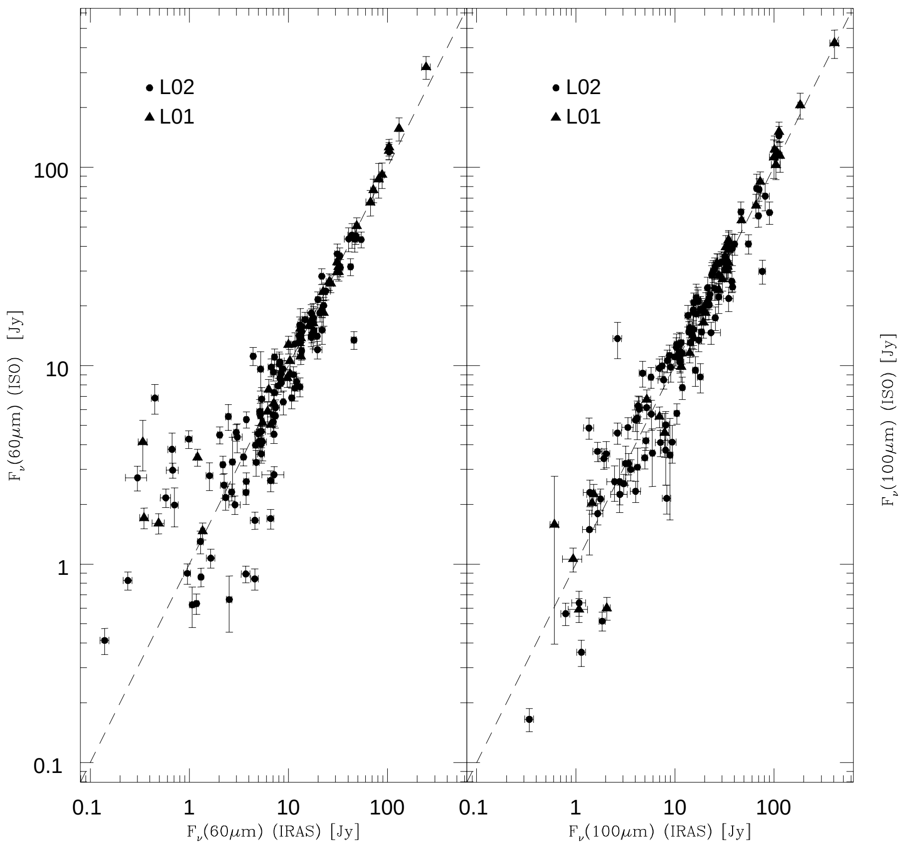


Figure 3.7: *LWS versus IRAS comparison for 60 μm and 100 μm. LWS01 observations are indicated with triangles while LWS02 observations are indicated with filled circles. The IRAS errors come from the Point Source Catalogue, and the ISO errors are a combination of the calibration and measurement uncertainty errors (from Brauher & Lord 2001, [1]).*

60 and 100 $\mu$m, typically within 26% for fluxes above 5 Jy. The ISO fluxes, according to this study are (1) systematically lower than IRAS fluxes by 3% between 5–300 Jy at 60 $\mu$m and (2) systematically higher than the IRAS fluxes by 2% between 5–300 Jy at 100 $\mu$m. Below 5 Jy the dispersion increases by a factor of two and is attributed to the dark current subtraction errors.

However, it is worth to note that if only the brightest sources in the sample are considered (above 25 Jy) the LWS fluxes are found systematically 12% higher than the corresponding IRAS fluxes both at 60 $\mu$m and 100 $\mu$m. This result is strikingly similar to the offset found at 100 $\mu$m by Chan et al. 2001, [4].

The strong discrepancies at high flux levels are more evident in Figure 3.7 where we have plotted the same results in a different format. The discrepancy seems to be of the order of 20–40% for fluxes above 70–80 Jy, supporting our previous findings.

### 3.1.3 ISO composite SWS+LWS spectra versus IRAS photometry at 60 and 100 $\mu$m

We can take advantage of the availability of the sample of cross-calibration sources used for the internal comparison between SWS and LWS presented in Section 2.1.4 to produce good quality, composite ISO SWS+LWS spectra which can be directly compared with IRAS photometry at 60 and 100 $\mu$m. The spectral coverage of the resulting ISO composite spectrum is such that there is no need need to apply in this case any correction factor to the IRAS photometry at 60 $\mu$m, since the IRAS photometric band is fully covered by ISO when we combine SWS+LWS data in a single spectrum.

The test sample includes 23 sources which are listed in Table 3.1. Note that, unfortunately, we had to exclude from this cross-calibration analysis some of the sources used in the previous comparison. For instance, this time we could not include the well known variable sources TX Cam or OH 26.5+0.6, observed close in time by ISO with SWS and LWS, but at a completely different epoch with respect to IRAS photometry, taken in 1983–1984. Neither we could use the source IRAS 15452−5459 because of the bad quality of its IRAS photometry at 60 and 100 $\mu$m.

Table 3.1: *ISO OLP Version 10.1 synthetic photometry at 60 and 100 $\mu$m compared with IRAS photometry*

| Source | IRAS 60 $\mu$m | IRAS 100 $\mu$m[1] | IRAS 100 $\mu$m[2] | ISO 60 $\mu$m | ISO 100 $\mu$m | IRAS *CIRR2* | Notes |
|---:|:-:|:-:|:-:|:-:|:-:|:-:|:--|
| HD 161796 | 151.7 | 48.7 | 49.2 | 167.3 | 56.3 | 1 | |
| NGC 6543 | 133.3 | 62.7 | 63.3 | 144.2 | 72.9 | 1 | |
| IRAS 19114+0002 | 515.9 | 168.1 | 169.8 | 674.5 | 224.3 | 1 | |
| R Dor | 243.5 | 83.5 | 84.3 | 311.1 | 96.3 | 1 | strong near infrared leak |
| CRL 618 | 1036 | 339.9 | 343.3 | 1361 | 547.4 | 1 | bad SWS band 4 |
| CPD −56 8032 | 199.1 | 91.7 | 93.5 | 236.5 | 105.0 | 2 | |
| CW Leo | 5652 | 922.0 | 940.0 | 5297 | 1247 | 2 | |
| Circinus | 248.7 | 315.9 | 322.2 | 314.6 | 426.3 | 2 | bad SWS band 4 |
| HD 101584 | 193.0 | 104.0 | 110.2 | 226.4 | 132.5 | 3 | |
| Hen 2−113 | 176.6 | 71.3 | 75.6 | 217.5 | 94.7 | 3 | |
| M 1−78 | 589.6 | 408.2 | 432.7 | 792.6 | 592.6 | 3 | |
| HD 44179 | 173.1 | 66.2 | 70.2 | 215.1 | 81.9 | 3 | |
| IC 418 | 103.6 | 31.2 | 33.1 | 119.6 | 35.4 | 3 | |
| IRAS 16342−3814 | 290.2 | 139.4 | 157.5 | 262.8 | 122.1 | 4 | mean of two measurements |
| SAO 34504 | 96.6 | 41.0 | 46.3 | 119.1 | 44.0 | 4 | bad SWS band 4 |
| AFGL 4106 | 851.8 | 181.1 | 239.1 | 1053 | 310.4 | 5 | |
| $\mu$ Cep | 127.0 | 49.9 | 65.9 | 140.1 | 52.8 | 5 | strong near infrared leak |
| IRAS 16594−4656 | 131.4 | 34.4 | 61.2 | 146.2 | 78.2 | 6 | |
| IRAS 21282+5050 | 33.4 | 15.0 | 26.7 | 38.6 | 31.4 | 6 | |
| IRAS 21318+5631 | 90.0 | 25.4 | 44.7 | 93.8 | 45.0 | 6 | |
| $\alpha$ Sco | 115.5 | 31.9 | 56.1 | 139.2 | 53.2 | 6 | bad SWS band 4 & strong near infrared leak |
| VX Sgr | 262.7 | 82.3 | 144.9 | 312.9 | 197.9 | 7 | |

[1] IRAS flux density quoted in the Point Source Catalogue
[2] restored IRAS flux density including background cirrus emission

At these long wavelengths, and as it was already mentioned in Section 3.1.2, one needs to consider very seriously the amount of cirrus contamination in the measurements. In principle, the effect is expected to be strong only at 100 $\mu$m in regions of strong cirrus background while the measurements at 60 $\mu$m will only be slightly affected. In any case, in order to take this possibility into account and because it can be of help in the analysis, the sources in Table 3.1 have been sorted as a function of the parameter *CIRR2*, previously defined in Equation 2.1, which is directly related with the background emission at 100 $\mu$m in the vicinities of the IRAS point source.

For the derivation of the ISO SWS+LWS synthetic photometry at 60 and 100 $\mu$m listed in Table 3.1 we used again ISAP Version 2.1. First the corresponding SWS+LWS OLP Version 10.1 spectra were directly retrieved from the ISO Data Archive and combined to create the composite spectra. Then bad data points affected by glitches in both SWS and LWS sections of the composite spectra were removed and the LWS spectra were corrected for near infrared leaks when necessary. Finally the `syn_phot` application of ISAP was used to convolve the ISO spectrum with the transmission profile of the IRAS filters at 60 and 100 $\mu$m. This way we derived a monochromatic flux at each of these wavelengths under the assumption that the source SED shape is of the form $\nu \times f_\nu$ = constant, or equivalently $\lambda \times f_\lambda$ = constant, in the same way as IRAS did.

Figure 3.8 shows the distribution of the derived ISO/IRAS flux density ratios at 60 $\mu$m as a function of the IRAS flux density at 60 $\mu$m in logarithmic scale. As we can see the systematic discrepancy between ISO and IRAS photometry at 60 $\mu$m (of the order of 15%) is confirmed.

The discrepancy cannot be attributed to background contamination since it is not correlated at all with the value of the IRAS *CIRR2* parameter. Instead, there seems to be a clear correlation with increasing flux, similar to that previously found for the sample of extragalactic sources analysed in Section 3.1.2.

In order to determine whether this systematic discrepancy between ISO and LWS is also found at 100 $\mu$m we used again the sources in Table 3.1 to perform an independent analysis.

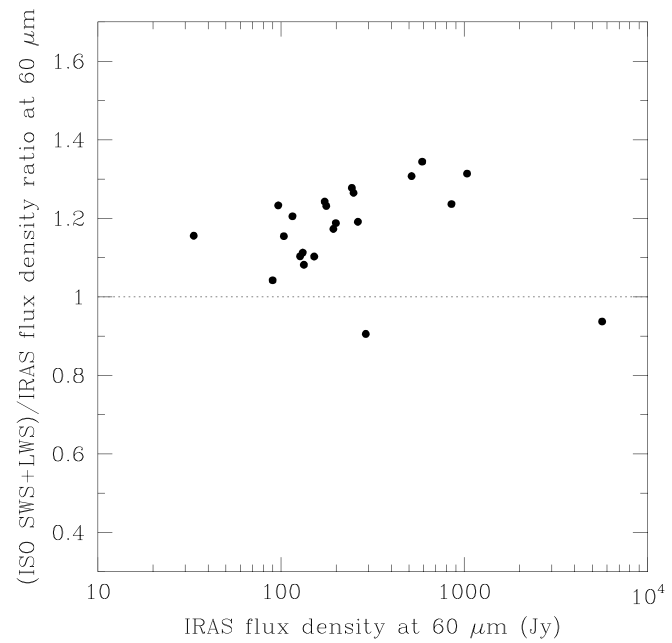


Figure 3.8: *The ISO/IRAS flux density ratios at 60 $\mu$ as a function of the IRAS flux density at 60 $\mu$m.*

Following the strategy proposed by Josephine Chan in their comparison of ISO data with IRAS photometry at 100 $\mu$m, we used their Method 1, this is, the restoration of the background emission estimated from the *CIRR2* parameter to the quoted IRAS flux density at 100 $\mu$m in the IRAS Point Source Catalogue Version 2.1, to determine the total cirrus+source flux density. This is the quantity that must be used to compare with the LWS measurements, as

LWS measured both source+background emission.

Figure 3.9 shows in logarithmic scale the distribution of ISO/IRAS flux density ratios at 100 $\mu$m as a function of the restored IRAS flux density at 100 $\mu$m.

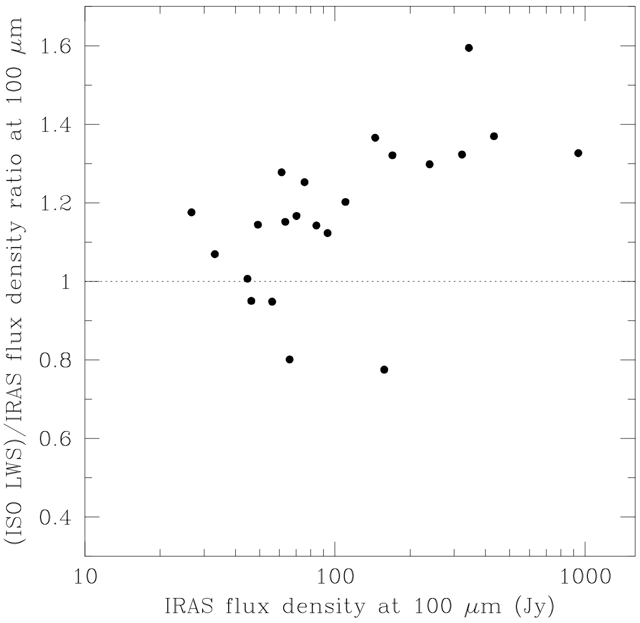


Figure 3.9: *The ISO/IRAS flux density ratios at 100 $\mu$ as a function of the restored IRAS flux density at 100 $\mu$m for the same calibration sample used in Figure 3.8.*

Interestingly, we see again the same effect. ISO equivalent fluxes at 100 $\mu$m are found to be around 20% higher if we take the mean value of all measurements and up to 60% in the most extreme cases. The discrepancies found are not correlated with IRAS *CIRR2*, being equally distributed among sources with low and high background contamination. Surprisingly we find again, instead, what seems to be a clear correlation with the flux level, so that in general the brightest sources are those showing the strongest discrepancies while ISO data and IRAS photometry appear consistent to within the 25% level for sources below 100 Jy.

A plot which combines all the results obtained in the three independent cross-calibration analysis performed at 60 and 100 $\mu$m between ISO and IRAS here presented is shown in Figure 5.8 of the ISO Handbook Volume III on LWS.

In summary, our conclusion is that both at 60 and 100 $\mu$m IRAS and ISO agree within a few % in average for sources fainter than 25 Jy, while ISO fluxes are found systematically higher than IRAS fluxes for sources brighter than 25 Jy. The difference increases from about 15% around 100 Jy, to a level of about 20% for sources up to 400 Jy, and up to 30–50% for sources brighter than 400 Jy.

The reason for this behaviour is not understood. We know it is not due to inaccurate dark current subtraction, nor to cirrus background contamination. A possible cause could be some non-linearities in the infrared detectors. However, the problem could be associated with IRAS data and not with ISO.

Indeed, Figure IV.A.4.2 of the IRAS Explanatory Supplement, [28] does evidence detector non-linearity behaviour and Section VI.B.4.d quotes errors of respectively 30% and 70% at 60 and 100 $\mu$m for sources above 100 Jy.

### 3.1.4 LWS raster scans of extended sources versus IRAS photometry

LWS observations have also been made at a number of positions in the complex Trumpler 14 and 16 fields, and in the direction of the Galactic Centre. LWS data have been compared with the IRAS 100 $\mu$m fluxes at the same positions. All fields contain large areas of extended emission, which although relatively smooth, do change by a factor of $\sim$40 within each region.

The point source fluxes (Jy) provided by the LWS pipeline calibration have been converted to extended source fluxes (MJy sr$^{-1}$) using the correction factors implemented in ISAP Version 2.0.

Figure 3.10 shows the comparison of the converted LWS and IRAS 100 $\mu$m fluxes. As we can see, the results indicate that there is an excellent agreement between the fluxes provided by ISO and the IRAS results. From the analysis of the data we obtain a mean ratio, LWS/IRAS = 1.0$\pm$0.1.

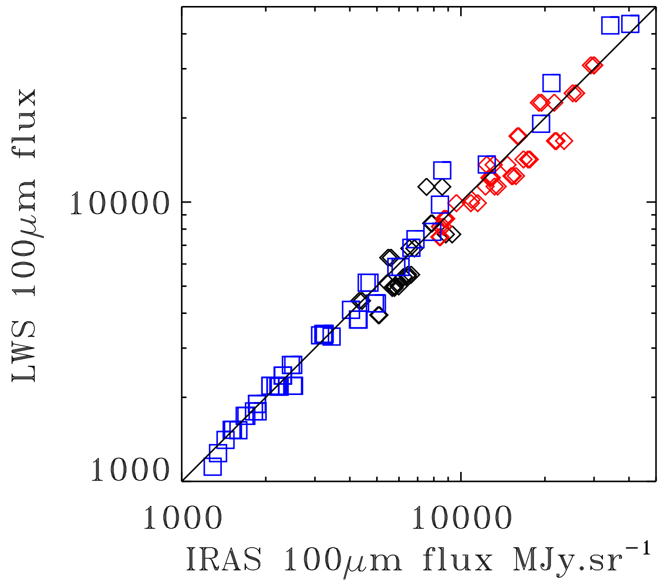


Figure 3.10: *Comparison of LWS and IRAS 100 $\mu$m fluxes in the Trumpler 14 (red diamonds), Trumpler 16 (black diamonds), and Galactic Centre (blue squares) fields.*

Part of the uncertainty is probably due to the unresolved structure of the sources observed within the beam. This is because the extended source correction factors applied have been derived under the assumption of a smooth and very extended flux distribution. In the real world, structure or embedded sources could produce significant discrepancies from the ideal situation and, with it, differences in flux.

Note also that for fields containing multiple sources the observed flux will depend critically on the precise positions of the sources relative to the optical axis. To recover or model the observed flux requires positional information on the sources and a deconvolution with the PSF and instrumental profile. Indeed, for single point sources observed off-axis a similar procedure is required to recover the correct flux.

### 3.1.5 ISOPHOT-P and -C versus IRAS photometry

The database of ISO observations generated by a project intended to search for Vega-like debris disks around nearby main-sequence stars (Habing et al. 1996, [21]; Laureijs et al. 2002, [34]) has also been used to assess the quality of ISOPHOT photometric calibration.

The sample contains more than 80 main sequence stars that were observed with ISOPHOT at 25, 60, 150 and 170 $\mu$m, in order to determine whether the star had an infrared excess indicating the presence of a dusty disk. Unfortunately, the number of stars found with disks was very low: only 8 out of 65 stars observed with ISO showed a significant excess at 60 $\mu$m.

The positive point, from the cross-calibration perspective, is that the non-detected stars constitute a nice homogeneous sample of observations which can be used to improve our knowledge of the quality of the observations made with ISOPHOT by comparing the observations with models and with the IRAS photometry of the same sources at 25 and at 60 $\mu$m.

The subsample of observations here analysed were performed using the AOT PHT03 (PHT-P detectors) in triangular chopped mode at 25 $\mu$m and mini-maps ($3\times3$ with $46''$ steps) centred at the source location at 60 $\mu$m using the AOT PHT22, and reflects the status of the PHT calibration as of OLP Version 8.

Figure 3.11 shows the result of the ISO observations compared to the IRAS photometry (when available) of the stars observed at 25 and 60 $\mu$m.

As we can see, the level of agreement with IRAS photometry at 25 $\mu$m is in most cases better than 25%. The brighter targets ($F_{25} > 1$ Jy) appear to have systematically ISO flux densities lower than the IRAS values. This underestimation is expected from the usage of the chopped mode, where a relatively high source-background contrast causes a signal loss due to transient responsivity in the PHT-P detector. On the other hand, the ISO fluxes of the fainter stars ($F_{25} <$ 300 mJy) appear overestimated with respect to IRAS. The explanation for this overestimation is still not clear but it might be the result of (i) the peculiar transient behaviour of the P2 detector, (2) a low level signal non-linearity, or (3) uncertainties in the IRAS calibration (we have to consider that at these low flux levels we are close to the detection limit of IRAS at 25 $\mu$m).

At 60 $\mu$m the statistics become poorer. IRAS fluxes are available only for 11 targets. The obvious outlier showing $F_{60,IRAS} >> F_{60,ISO}$ consists of 3 resolved point sources in the ISOPHOT map. For the remaining detections the correlation is high. However, the ISO observations are systematically ($\sim$25%) below the IRAS values. This discrepancy could partially be attributed to the fact that we have assumed point source calibration in the conversion from measured flux in an array pixel to the final target flux. In case of small extended sources the flux would be underestimated for this reason and this is actually what we observe in stars like Vega and $\beta$-Pictoris, contained in the sample, which are known to be slightly extended infrared sources.

As a consequence of the calibration upgrades implemented in the latest versions of the ISOPHOT pipeline, the accuracy of chopped PHT-P and PHT-C photometry has further improved significantly.

As an example, we show in Tables 3.2 and 3.3 the photometric data derived from OLP Version 10 for a subset of the stars in the sample above mentioned compared with IRAS photometry

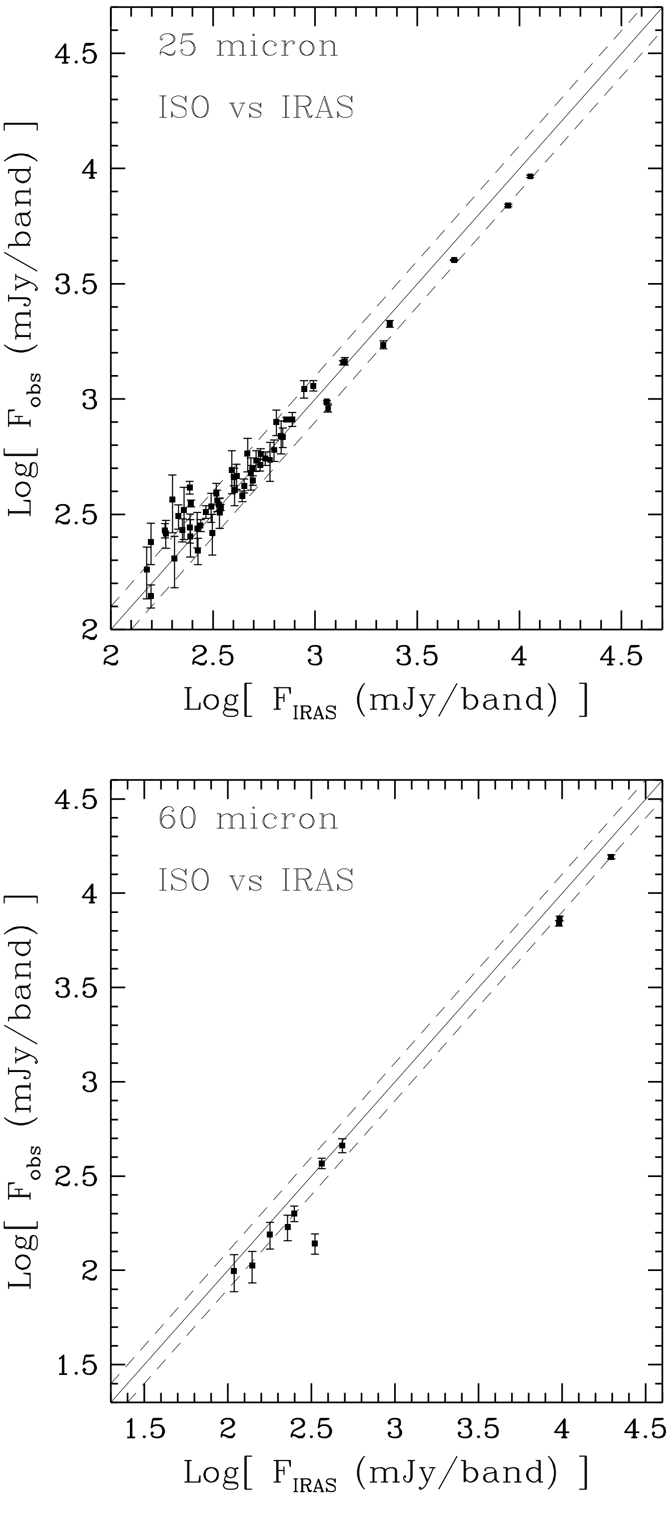


Figure 3.11: *The flux densities of the 80 main sequence stars included in the Vega project derived from ISO chopped PHT-P photometry at 25 μm (top) and PHT-C mini-maps at 60 μm (bottom) are compared to IRAS photometry. (from Laureijs et al. 1999, [33]).*

and model predictions (Ulrich Klaas, private communication). ISOPHOT and IRAS fluxes are colour corrected.

Table 3.2: *OLP Version 10 chopped PHT-P photometry at 25 $\mu$m compared to IRAS photometry and model predictions*

| Source $[Jy]$ | ISOPHOT flux $[Jy]$ | IRAS flux $[Jy]$ | Model flux $[Jy]$ |
|---|---|---|---|
| Sirius | 18.52 | 24.09 | 21.54 |
| HR7557 | 5.24 | 5.76 | 5.27 |
| HR7310 | 4.31 | 3.66 | 3.40 |
| HR5986 | 0.68 | 0.53 | 0.52 |
| | 0.63 | | |
| | 0.58 | | |
| HR5914 | 0.39 | 0.41 | 0.38 |
| HR5447 | 0.32 | 0.30 | 0.26 |
| HR7469 | 0.25 | 0.22 | 0.25 |

Table 3.3: *OLP Version 10 chopped PHT-C photometry at 60 $\mu$m compared to IRAS photometry and model predictions*

| Source $[Jy]$ | ISOPHOT flux $[Jy]$ | IRAS flux $[Jy]$ | Model flux $[Jy]$ |
|---|---|---|---|
| Sirius | 4.08 | 3.73 | 3.68 |
| | 4.04 | | |
| HR1654 | 1.68 | 1.53 | 1.61 |
| HR7980 | 1.25 | 1.12 | 1.17 |
| HR7557 | 0.95 | 0.95 | 0.90 |
| HD185144 | 0.11 | 0.12 | 0.10 |
| HR7469 | 0.06 | ¡0.75 | 0.04 |

## 3.2 Comparison with MSX

In order to extend the cross-calibration analysis of ISO SWS to observations made with other space facilities than IRAS we performed a similar analysis using this time photometric data provided by the *Midcourse Space Experiment* (MSX; Egan et al. 1999, [16]).

Briefly, MSX was a multi-discipline experiment sponsored by the USA Ballistic Missile Defense Organization. The principal objective of the MSX astronomy experiments was to complete the census of the mid-infrared sky. Experiments were designed to cover the regions either missed by IRAS and COBE/DIRBE or where the sensitivity of IRAS was degraded by confusion noise in regions of high source densities or structured extended emission, including the entire Galactic Plane.

The MSX Point Source Catalogue contains all the point sources detected with signal-to-noise ratio > 3 following criteria very similar to IRAS (detection requires multiple confirmations).

The infrared instrument on MSX was a 35 cm clear aperture off-axis telescope cooled by a single solid $H_2$ cryostat equipped with Si:As BiB arrays with eight columns of detectors, each with 192 rows of 18".3 square pixels, and a high sensitivity (0.1 Jy at 8.3 $\mu$m). Two narrow band filters covered the spectral regions centred at 4.29 (B1) and 4.35 (B2) $\mu$m, and four broad-band filters covered the spectral regions centred at 8.28 (A), 12.13 (C), 14.65 (D) and 21.34 (E) $\mu$m (see Table 3.4).

Table 3.4: *Description of MSX photometric bands*

| Band | No active cols. | Isophotal $\lambda[\mu$m] | 50% peak intensity | Isophotal BW[$\mu$m] | Zero mag flux [Jy] | Abs. Photom. Accuracy | Survey Sens. [Jy] | Effective FOV $\Omega_{EFOV}$ [$\times 10^{-9}$sr] |
|---|---|---|---|---|---|---|---|---|
| A | 8 | 8.28 | 6.8−10.8 | 3.36 | 58.49 | 5% | 0.1−0.2 | 10.6 |
| $B_1$ | 2 | 4.29 | 4.22−4.36 | 0.104 | 194.6 | 9% | 10−30 | 14.0 |
| $B_2$ | 2 | 4.35 | 4.24−4.45 | 0.179 | 188.8 | 9% | 6−18 | 14.0 |
| C | 4 | 12.13 | 11.1−13.2 | 1.72 | 26.51 | 3% | 1.1−3.1 | 11.7 |
| D | 4 | 14.65 | 13.5−15.9 | 2.23 | 18.29 | 4% | 0.9−2 | 11.3 |
| E | 2 | 21.34 | 18.2−25.1 | 6.24 | 8.80 | 6% | 2−6 | 12.6 |

In the following analysis we will only consider the broad MSX filters A, C, D and E, which are the most sensitive filters onboard MSX.

About 100 sources with an available SWS01 spectrum in the ISO Data Archive were identified to have their corresponding mid-infrared counterpart in the MSX Point Source Catalogue.

After excluding from this sample all the suspected variable stars and extended sources (as we did for the cross-calibration with IRAS) we ended up with around 50 sources suitable for cross-calibration with MSX at all the above mentioned filters.

The OLP Version 10 SWS spectra of these sources were retrieved from the ISO Data Archive and further processed with ISAP Version 2.1. Bad data points affected by glitches were identified and removed from the SWS spectra using the available tools in ISAP and ISO 'synthetic photometry' was performed at the A, C, D and E MSX filters with the help of `syn_phot`. This ISAP application convolves the ISO spectrum with the transmission profile of the corresponding MSX filters assigning a monochromatic flux to each band under the assumption that the SED shape is of the form $\nu \times f_\nu$ = constant, or equivalently $\lambda \times f_\lambda$ = constant.

In Figures 3.12 to 3.15 we show the results obtained. As we can see, they are very similar to the ones obtained in the previous cross-calibration comparison with IRAS data.

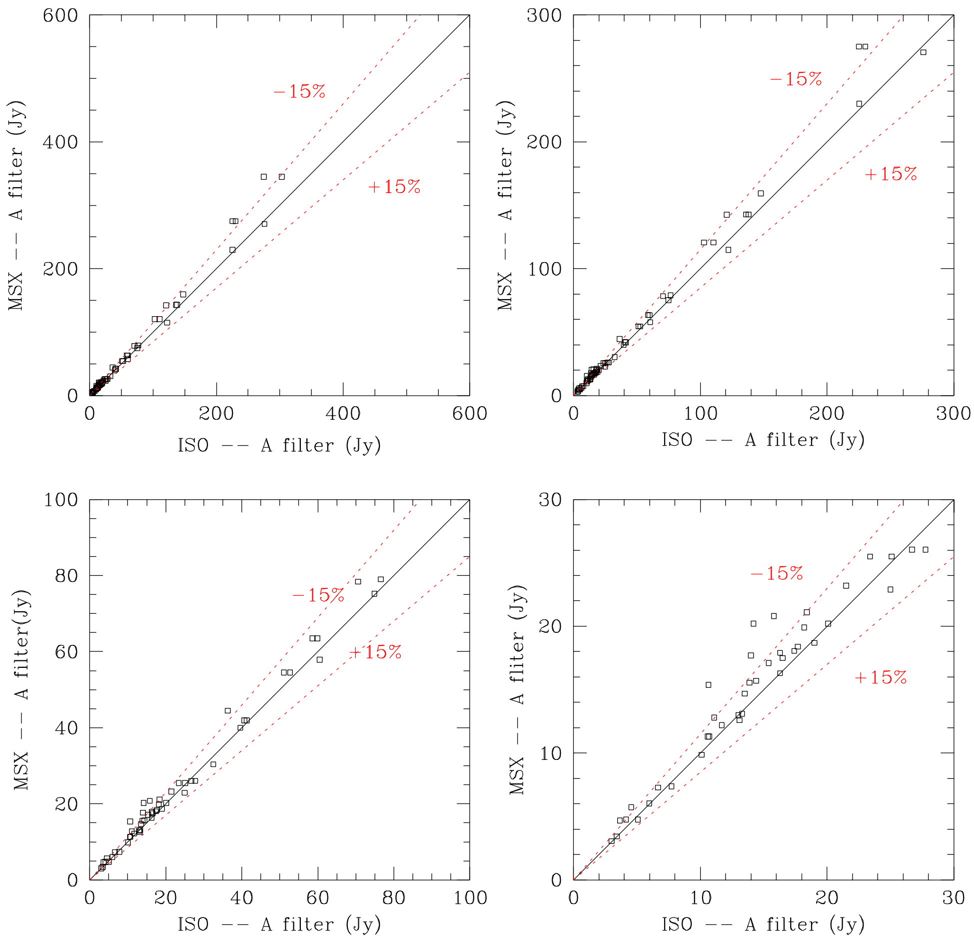


Figure 3.12: *ISO SWS synthetic photometry at 8.28 $\mu$m derived from OLP Version 10 data products compared to MSX filter A photometry at the same wavelength. The dashed red line represents a 15% discrepancy level.*

Esentially, the absolute flux calibration of ISO SWS and MSX agrees to within the 10–15% level at all flux levels, with very little degradation even at the lower flux levels.

The few outliers are interpreted as previously unknown variable sources and/or slightly badly pointed observations, similarly to what was observed in the previous comparison with IRAS.

Comparing the absolute flux level of all the measurements peformed with ISO and MSX there is a general good agreement in all filters with a zero-point consistency better than 5% in all cases with the exception of filter A (see Figure 3.16), where the distribution of observed discrepancies show a marked asymmetry.

This asymmetry is most probably due to a higher percentage of badly pointed observations (similarly to what we observed also in the cross-calibration comparison with IRAS at 12 $\mu$m).

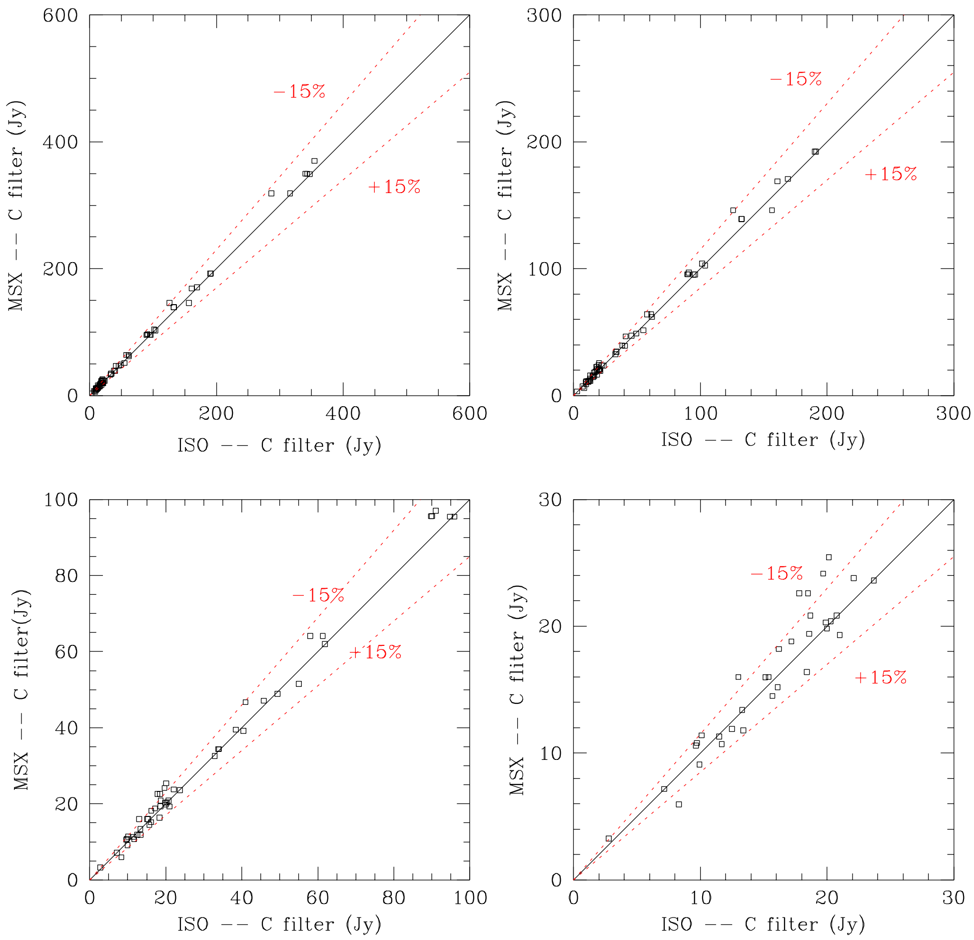


Figure 3.13: *ISO SWS synthetic photometry at 12.13 μm derived from OLP Version 10 data products compared to MSX filter C photometry at the same wavelength. The dashed red line represents a 15% discrepancy level.*

Note that this is the filter covering a wavelength range where SWS is most sensitive to small pointing offsets because of the smaller aperture size.

On the other hand, the slightly worse correlation found between ISO SWS and MSX filters D and E (compared to filters A and C) is probably induced by the fact that these filters show a larger overlap with SWS band 3, which is known to be less accurate than SWS band 2 in terms of absolute flux calibration.

Globally considered, the main difference found with respect to the previous cross-calibration comparison with IRAS is the absence of the strong discrepancies observed at high flux levels between ISO and IRAS data. This supports our hypothesis that the non-linearity problem is in the IRAS calibration at high flux levels.

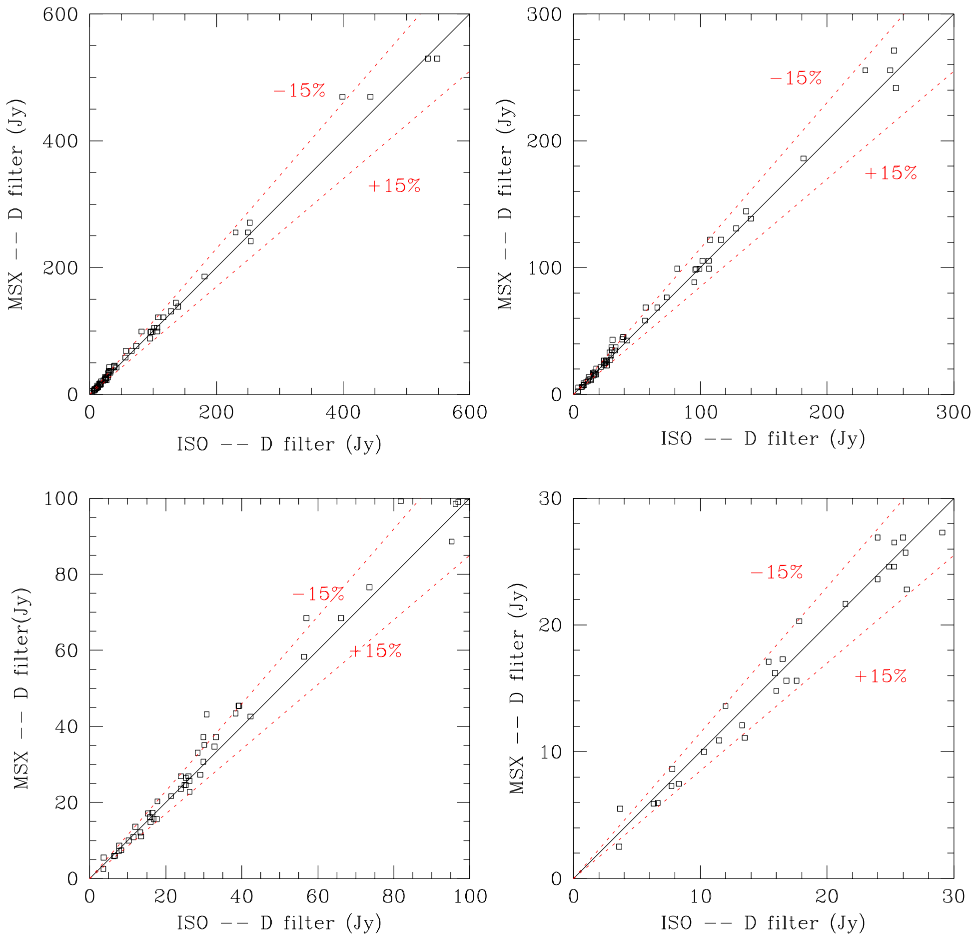


Figure 3.14: *ISO SWS synthetic photometry at 14.65 μm derived from OLP v10 data products compared to MSX filter D photometry at the same wavelength. The dashed red line represents a 15% discrepancy level.*

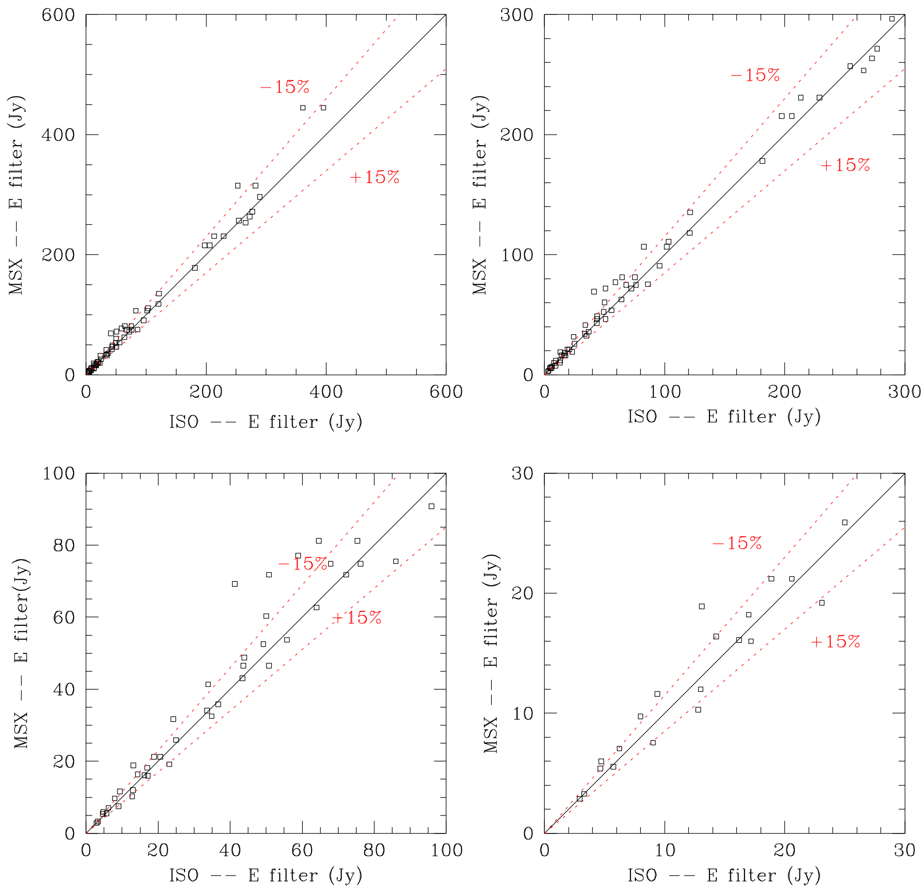


Figure 3.15: *ISO SWS synthetic photometry at 21.34 μm derived from OLP v10 data products compared to MSX filter E photometry at the same wavelength. The dashed red line represents a 15% discrepancy level.*

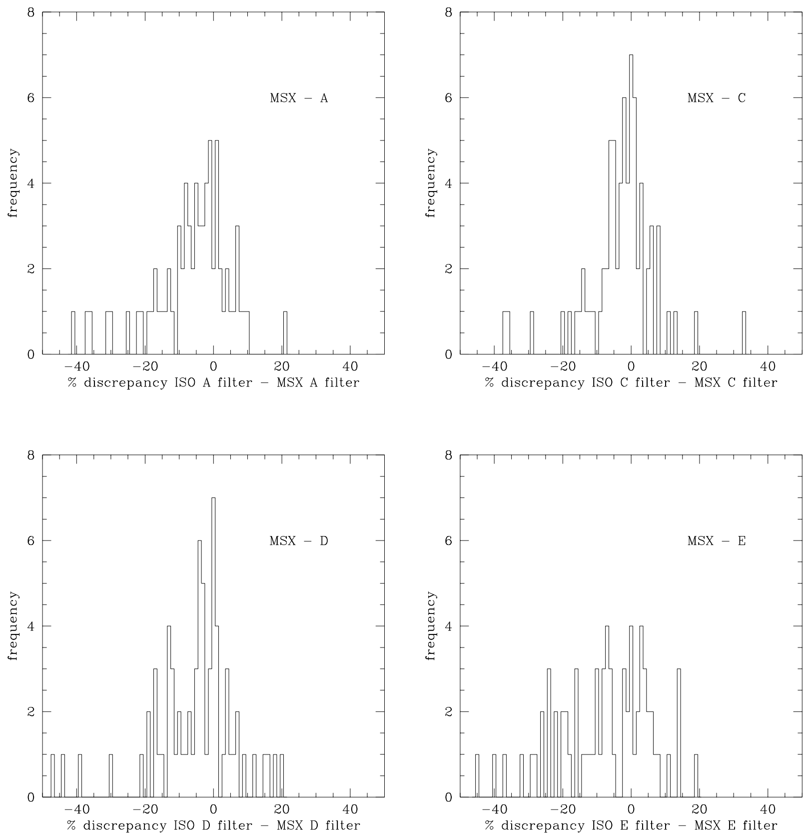


Figure 3.16: *Distribution of discrepancies found between the ISO SWS synthetic photometry at 8.28, 12.13, 14.65 and 21.34 μm, derived from OLP Version 10 data products compared to MSX filter A, C, D and E photometry, respectively.*

## 3.3 Comparison with COBE/DIRBE

ISOPHOT data has also been compared with COBE/DIRBE data as part of our cross-calibration analysis. The *Diffuse Infrared Background Experiment* (DIRBE; Hauser et al. 1998b, [24]) was one of the three instruments onboard COBE (the *Cosmic Background Explorer*), a satellite developed by NASA's Goddard Space Flight Center and launched in November 1989 to measure the diffuse infrared and microwave radiation from the early universe to the limits set by our astrophysical environment.

DIRBE obtained infrared absolute sky brightness maps in the wavelength range 1.25 to 240 $\mu$m. Most of this range was also covered by ISOPHOT. However, the comparison between ISOPHOT and COBE/DIRBE data is complicated, mainly because of the vastly different beam sizes ($42'$ FWHM for COBE/DIRBE), as we will see below.

### 3.3.1 PHT-S spectroscopy versus COBE/DIRBE photometry

In order to check the consistency between the absolute flux calibration of COBE/DIRBE photometry and PHT-S spectroscopy we present here a comparison of the absolute surface brightness of the zodiacal light measured by PHT-S and COBE/DIRBE data reported by Dotto et al. 2002, [15].

Figure 3.17 shows the OLP Version 9.0 sky background measurements taken with the long wavelength channel of PHT-S in the vicinities of the asteroids Frigga, Kassandra and Polyxo together with COBE data at 4.9 and 12 $\mu$m. Note that the zodiacal light is the dominating background at the PHT-S wavelengths.

As we can see PHT-S is in excellent agreement with COBE data. From the sky background observed we can deduce that the zodiacal light can be well approximated by a blackbody emitting at a temperature of 267 K.

For the short wavelength channel the comparison is not possible because the extremely low flux in this range is below the detection limit of PHT-S. In spite of this we see that the featureless PHT-S spectrum fits nicely between the COBE/DIRBE photometric data points at 4.9 and 12 $\mu$m.

Unfortunately, COBE did not cover wavelengths in between 5 and 12 $\mu$m, in the range where the brightness of the zodiacal light rises very steeply. However, complementary results obtained with PHT-P and ISOCAM confirm that the zodiacal emission spectrum can be well fitted by a blackbody of 267 K and that the spectrum is featureless between 5 and 16 $\mu$m.

### 3.3.2 PHT-C versus COBE/DIRBE photometry

The consistency of the absolute sky brightness derived from ISO C100 maps with COBE/DIRBE data was also verified as part of the OLP Version 8.4 scientific validation of PHT22 staring raster maps (Klaas et al. 2000, [30]).

The mean surface brightness of specific areas of the sky was derived from the full C100 maps used for the flat-field assessment and compared with the surface brightness values in the corresponding filters or adjacent filters of COBE/DIRBE. The use of the full area of the ISOPHOT maps offers the advantage of getting a solid angle coverage comparable to the COBE/DIRBE pixels.

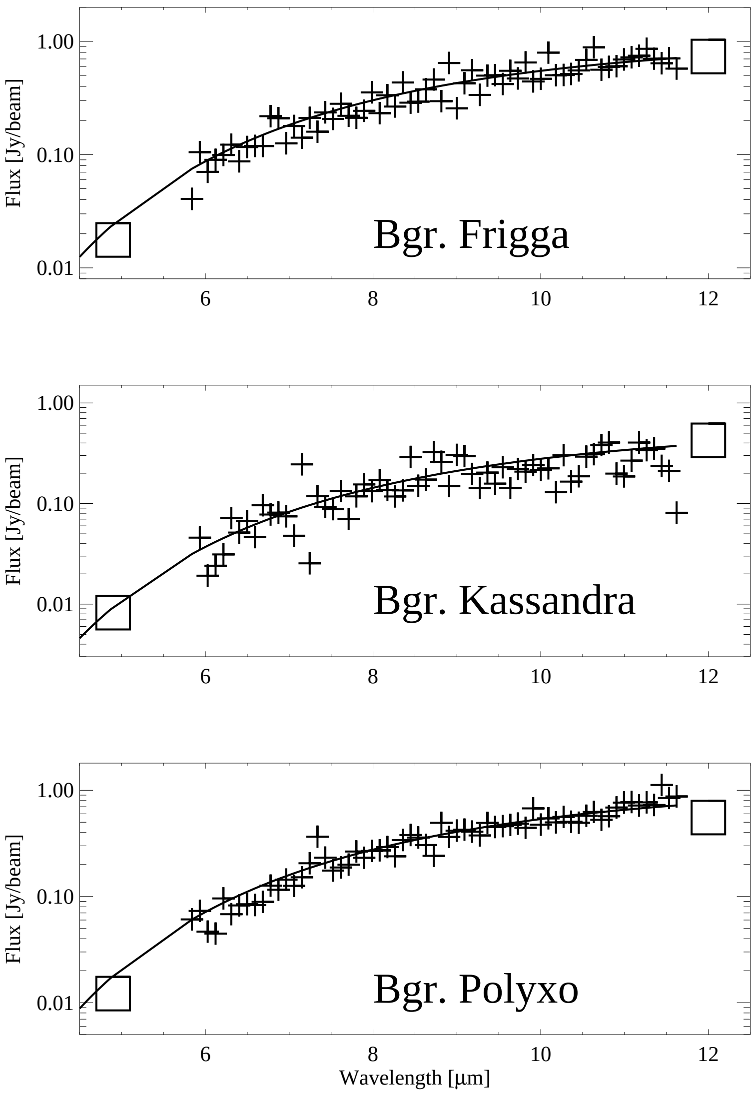


Figure 3.17: *Comparison of PHT-S sky background measurements made in the vicinities of the asteroids Frigga, Kassandra and Polyxo (crosses) with COBE data at 4.9 and 12 $\mu$m (squares). The solid line corresponds to the fitted blackbody curve (from Dotto et al. 2002, [15]).*

However, in most cases the solid angles of the ISOPHOT maps are still considerably smaller than one pixel in COBE/DIRBE. The COBE/DIRBE annual maps were used (since at the wavelengths considered the contribution from the zodiacal light is very small) to determine the fluxes for the DIRBE pixel coincident with the map area centroid. For a check of the large scale variations of the sky background average fluxes of a 1.5 degree circular area were as well determined. ISOPHOT maps containing bright sources were not considered (they would give a considerably higher average surface brightness due to the smaller area considered).

In Table 3.5 we present the results obtained. Except for the different beam sizes a comparison of the ISOPHOT/DIRBE 60 and 100 $\mu$m filters is relatively straightforward. In general a good agreement better than 25%, in particular for those maps with comparable sizes to the COBE/DIRBE beam, is found. All larger deviations can be explained by the source structure which is extended over the ISOPHOT map area, but compact inside the COBE/DIRBE beam. The largest outlier shows a similar excess in the C200 range.

Without any correction, the ISOPHOT 90 $\mu$m filter maps seem to show a systematic positive surface brightness excess with regard to the DIRBE 100 $\mu$m photometry. However, inspection of the COBE/DIRBE SEDs indicates a steep decline in flux between 60 and 100 $\mu$m. In fact, the 90 $\mu$m ISOPHOT values are practically always in between the 60 and 100 $\mu$m DIRBE values. Very often, the surface brightness ratio 60/100 is about 2, i.e. with a linear interpolation between 60 and 100 $\mu$m, the 90 $\mu$m flux is by 25% higher than the 100 $\mu$m flux due to the shape of the SED. Then, also the surface brightness of the 90 $\mu$m maps are consistent with COBE/DIRBE within the 25% level. If the discrepancy between the ISOPHOT 90 $\mu$m surface brightness and the DIRBE 100 $\mu$m surface brightness is small, usually the source SED is reasonably flat between 60 and 100 $\mu$m. Whether there is still a positive excess at 90 $\mu$m cannot be solved by this kind of study, but needs better matching areas and a proper colour correction of the background SEDs.

From the consistency found in the three filters at 60, 90 and 100 $\mu$m and the relative photometric accuracies of all ISOPHOT C100 filters, we conclude that the consistency should also hold for the remaining ISOPHOT filters at 65, 80 and 105 $\mu$m. The good correspondance holds for the flux range 4.5 to 400 MJy sr$^{-1}$.

A similar analysis was also performed by Klaas et al. 2000, [30] for ISOPHOT C200 maps. Since the longest COBE/DIRBE filters (140 and 240 $\mu$m) have an internal uncertainty of 20 to 30%, for a subsample of maps with low dynamic range the average fluxes of a 1.5 degree circular area were used, which gives a more robust photometry (this means averaging over 70 COBE/DIRBE pixels).

In Table 3.6 we present the results of the comparison. No colour correction with regard to a modified blackbody describing the background spectral energy distribution nor a wavelength correction to better match the COBE/DIRBE filter central wavelength with the ISOPHOT filter central wavelength were performed. Again we have to remark that nearly all the ISOPHOT maps are considerably smaller in area than the solid angle of one COBE/DIRBE pixel. Therefore, structures in the source or background can affect the resulting absolute flux. In case of a flat field, the flux of the centred COBE/DIRBE pixel as well as the 3 degree circular area average is listed to give an impression of the variation of the background (and also the stability of the COBE/DIRBE measurement in one pixel). If the map contains a bright target and is smaller than the COBE/DIRBE pixel, then only the flux of the centred COBE/DIRBE pixel is given.

Taking into account the discrepancies in beam size and the non-correction for different wavelengths of filters and background SEDs, the general agreement is in the order of 20 to 30% at all four filters considered (150, 170, 180 and 200 $\mu$m). Restricting the comparison to ISOPHOT maps with comparable solid angles with the COBE/DIRBE measurement, the consistency is confirmed to be better than 25%. This holds for all filters and a surface brightness range between 2.5 and 600 MJy sr$^{-1}$.

Larger deviations between the average ISOPHOT map flux and the COBE/ DIRBE flux only occur for bright central sources which are compact in comparison with the COBE/DIRBE beam. In these cases, the COBE/DIRBE fluxes are always less than the ISOPHOT fluxes, as expected.

Table 3.5: *Consistency check of C100 map absolute surface brightness with COBE/DIRBE annual map photometry. The solid angle of one COBE/DIRBE pixel is 19.5 $10^{-5}$ sr. No correction for the wavelength shift between ISOPHOT 90 $\mu$m and DIRBE 100 $\mu$m filters has been performed which causes for most sky backgrounds a systematic positive excess of the 90 $\mu$m flux (see text for details).*

| OLP product name | filter [$\mu$m] | surface brightness [MJy sr$^{-1}$] | solid angle [$10^{-5}$sr] | DIRBE flux [MJy sr$^{-1}$] | DIRBE filter [$\mu$m] | solid angle [$10^{-5}$sr] | consistency [%] |
|---|---|---|---|---|---|---|---|
| 19002101 | 60 | 6.8 | 0.81 | 6.6 | 60 | 19.5 | +2.2 |
| 08900102 | 60 | 9.5 | 1.60 | 6.5 | 60 | 19.5 | +47 |
| 85001219 | 60 | 22.8 | 0.21 | 22.3 | 60 | 19.5 | +2.2 |
| 13400214 | 60 | 39.8 | 0.22 | 39.6 | 60 | 19.5 | +0.6 |
| 68300807 | 60 | 21.3 | 6.77 | 27.2 | 60 | 19.5 | −22 |
| 84403913 | 60 | 23.9 | 1.04 | 24.5 | 60 | 19.5 | −2.5 |
| 69801101 | 60 | 107.4 | 1.16 | 122.3 | 60 | 19.5 | −12 |
| 35100809 | 90 | 5.1 | 5.49 | 3.3 | 100 | 19.5 | +55 |
| 58200903 | 90 | 11.8 | 3.06 | 12.9 | 100 | 19.5 | −7.9 |
| 19201091 | 90 | 4.8 | 7.30 | 3.1 | 100 | 19.5 | +52 |
| 86901244 | 90 | 5.2 | 2.75 | 3.6 | 100 | 19.5 | +44 |
| 41502788 | 90 | 8.1 | 5.10 | 5.7 | 100 | 19.5 | +44 |
| 09000606 | 90 | 11.8 | 0.77 | 11.3 | 100 | 19.5 | +4.4 |
| 08901904 | 90 | 15.1 | 0.23 | 13.6 | 100 | 19.5 | +11 |
| 40100614 | 90 | 14.7 | 6.80 | 13.3 | 100 | 19.5 | +10 |
| 87001338 | 90 | 5.3 | 2.93 | 3.6 | 100 | 19.5 | +47 |
| 57501902 | 90 | 12.1 | 1.15 | 9.7 | 100 | 19.5 | +25 |
| 53700514 | 90 | 4.4 | 0.85 | 3.7 | 100 | 19.5 | +21 |
| 60002009 | 90 | 7.1 | 4.24 | 5.2 | 100 | 19.5 | +37 |
| 50000124 | 90 | 4.8 | 8.87 | 3.3 | 100 | 19.5 | +43 |
| 50100273 | 90 | 5.8 | 8.68 | 3.5 | 100 | 19.5 | +68 |
| 20701079 | 90 | 25.6 | 0.33 | 22.8 | 100 | 19.5 | +12 |
| 20800709 | 90 | 5.8 | 3.49 | 4.0 | 100 | 19.5 | +46 |
| 86800640 | 90 | 5.7 | 2.96 | 3.6 | 100 | 19.5 | +60 |
| 10101158 | 100 | 30.7 | 1.71 | 21.0 | 100 | 19.5 | +46 |
| 79401149 | 100 | 44.2 | 0.51 | 40.6 | 100 | 19.5 | +9.0 |
| 44900714 | 100 | 387.7 | 15.2 | 440.1 | 100 | 19.5 | −12 |
| 15601578 | 100 | 17.4 | 1.82 | 6.1 | 100 | 19.5 | +187 |
| 27600420 | 100 | 15.4 | 1.74 | 12.1 | 100 | 19.5 | +27 |
| 71901220 | 100 | 18.5 | 3.66 | 16.0 | 100 | 19.5 | +15 |
| 33401134 | 100 | 96.4 | 4.06 | 49.3 | 100 | 19.5 | +96 |

Table 3.6: *Consistency check of C200 map absolute surface brightness with COBE/DIRBE annual map photometry. The solid angle of one COBE/DIRBE pixel is 19.5 $10^{-5}$ sr (see text for details).*

| OLP product name | filter [$\mu$m] | surface brightness [MJy sr$^{-1}$] | solid angle [$10^{-5}$sr] | DIRBE flux [MJy sr$^{-1}$] | DIRBE filter [$\mu$m] | solid angle [$10^{-5}$sr] | consistency [%] |
|---|---|---|---|---|---|---|---|
| 56200110 | 150 | 3.6 | 2.91 | 4.1 | 140 | 19.5 | −13 |
| 56201814 | 150 | 22.2 | 0.42 | 20.9 | 140 | 19.5 | +6.2 |
| 08900103 | 150 | 5.5 | 1.26 | 7.7 | 140 | 19.5 | −29 |
| 79400434 | 170 | 3.2 | 3.15 | 2.2 | 140 | 19.5 | +45 |
| | | | | 2.9 | 140 | 215.3 | +10 |
| 59300101 | 170 | 3.5 | 6.53 | 3.5 | 140 | 19.5 | −1.4 |
| | | | | 3.4 | 140 | 215.3 | +4.2 |
| 19800208 | 170 | 3.2 | 3.41 | 5.0 | 140 | 19.5 | −37 |
| | | | | 3.3 | 140 | 215.3 | −3.6 |
| 21001305 | 170 | 3.6 | 3.39 | 4.1 | 140 | 19.5 | −12 |
| | | | | 3.5 | 140 | 215.3 | +3.4 |
| 79900733 | 170 | 6.0 | 0.50 | 7.0 | 140 | 19.5 | −14 |
| 33600108 | 180 | 2.7 | 2.50 | 2.7 | 140 | 19.5 | −2.6 |
| | | | | 2.8 | 140 | 215.3 | −4.0 |
| 33600705 | 180 | 4.7 | 2.55 | 5.7 | 140 | 19.5 | −17 |
| | | | | 5.7 | 140 | 215.3 | −17 |
| 35100907 | 180 | 4.1 | 4.92 | 4.5 | 140 | 19.5 | −8.2 |
| 16701206 | 180 | 15.0 | 4.11 | 12.7 | 140 | 19.5 | +18 |
| 52700412 | 180 | 3.2 | 0.87 | 3.8 | 140 | 19.5 | −16 |
| | | | | 3.2 | 140 | 215.3 | +0 |
| 85001037 | 180 | 8.1 | 3.78 | 10.1 | 140 | 19.5 | −19 |
| | | | | 9.3 | 140 | 215.3 | −13 |
| 78200101 | 200 | 6.3 | 28.40 | 5.3 | 240 | 34.45 | +20 |
| 36803005 | 200 | 14.8 | 0.71 | 15.5 | 240 | 19.5 | −4.5 |
| | | | | 14.9 | 240 | 215.3 | −0.9 |
| 39602213 | 200 | 36.2 | 6.22 | 29.2 | 240 | 19.5 | +24 |
| 26101401 | 200 | 69.8 | 11.03 | 85.4 | 240 | 19.5 | −18 |
| 33401133 | 200 | 138.6 | 3.89 | 87.6 | 240 | 19.5 | +58 |
| 86101801 | 200 | 251.9 | 5.01 | 287.9 | 240 | 19.5 | −13 |
| 15601577 | 200 | 11.4 | 1.38 | 5.9 | 240 | 19.5 | +95 |
| 33300559 | 200 | 38.0 | 6.55 | 55.7 | 240 | 19.5 | −32 |
| 10101157 | 200 | 69.7 | 1.41 | 45.2 | 240 | 19.5 | +54 |
| 31000625 | 200 | 345.4 | 1.45 | 207.8 | 240 | 19.5 | +66 |
| 26701013 | 200 | 593.3 | 15.49 | 494.5 | 240 | 19.5 | +20 |
| 40900802 | 200 | 6.9 | 1.97 | 5.6 | 240 | 19.5 | +23 |
| 28001303 | 200 | 13.0 | 2.00 | 12.8 | 240 | 19.5 | +1.6 |

# Chapter 4

# Comparison with Models

## 4.1 ISOCAM

A small sample of Hipparcos Input Catalogue (HIC, [26]) stars were used throughout the ISO mission to calibrate ISOCAM.

In order to determine the consistency between the measurements and the models used to derive the calibration curves, the fluxes derived from OLP Version 10 data for these stars obtained with multi-filter or CVF observations have been compared with the fluxes predicted by the models. Note that in many cases the same star was observed with various apertures. For this analysis all the available measurements were taken into account.

The fluxes considered here were those included in the CPSL (CAM Point Source List) file, which makes use of an automatic PSF fitting tool to determine the position and the flux of all the detected point sources in the ISOCAM field.

In general, the results obtained show that the consistency with models is within the 15% level in most cases.

However, it is remarkable that many of the flux measurements derived this way are significantly below the model fluxes. This could be the consequence of an incorrect PSF fitting since interactive aperture photometry with CIA generally overrides the problem.

The discrepancies between the mean value of all the measurements taken per star and the corresponding model fluxes are listed in Table 4.1. Globally considered, the results obtained show that the fluxes listed in the CPSL files are systematically ∼7% underestimated with respect to the model values.

In Figures 4.1 and 4.2 we show two examples of the results obtained in the case of HIC 67485 and HIC 77277, where the mean errors found were +2% and −10%, respectively.

The full report describing this consistency check can be found in Cesarsky 2002, [2].

Table 4.1: *Mean discrepancies found in the photometry of some ISOCAM calibration stars with respect to their models.*

| Calibration star | OLP v10 |
|---|---|
| HIC 67485 | +2% |
| HIC 69713 | −7% |
| HIC 70218 | −14% |
| HIC 73005 | −18% |
| HIC 77277 | −10% |
| HIC 85317 | +6% |
| HIC 94376 | −12% |
| HIC 94890 | −4% |

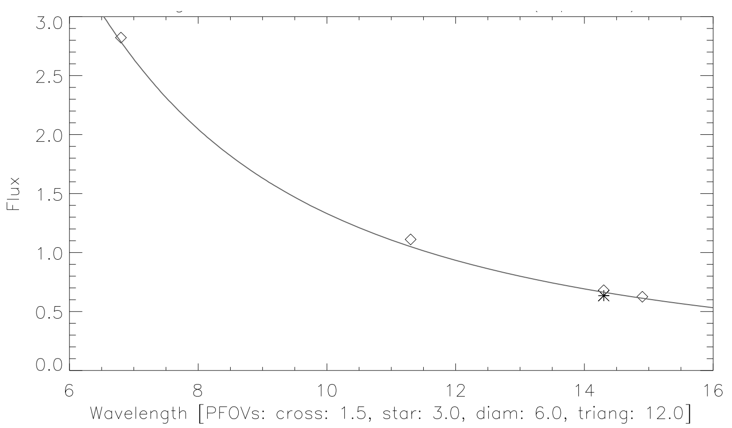


Figure 4.1: *Comparison of ISOCAM OLP Version 10 measurements on HIC 67485 with the calibration model.*

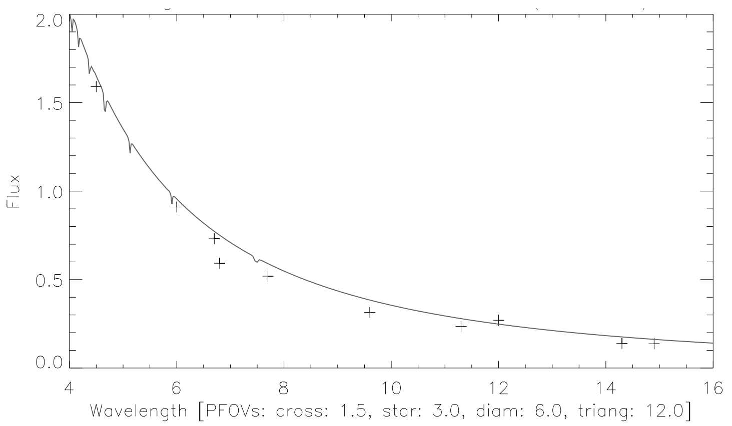


Figure 4.2: *Comparison of ISOCAM OLP Version 10 measurements on HIC 77277 with the calibration model.*

## 4.2 LWS

Several checks were also made during the process of scientific validation of LWS OLP Version 10 data products against models of planets, asteroids and stars (Lim et al. 2001, [36]). A summary of the main results obtained are presented here:

### LWS01 observations of Uranus

LWS photometric calibration is based on Uranus. Thus, a first consistency check was made by comparing Uranus observations versus the model produced by Griffin & Orton 1993, [18].

Table 4.2 shows the average flux for each detector and each observation divided by the average over the model for that detector. The red average row gives the overall average for the period of time covered by type 2 illuminator flashes (revolutions 237 to 442) and the blue row the period of time covered by the type 3 illuminator flashes (after revolution 442). Uranus was not visible during the period when type 1 illuminator flashes were used (before revolution 237).

Table 4.2: *Uranus LWS01 observations averaged per detector versus model predictions as deduced from OLP Version 10 data products for the validation revolutions*

| Rev | SW1 | SW2 | SW3 | SW4 | SW5 | LW1 | LW2 | LW3 | LW4 | LW5 |
|---|---|---|---|---|---|---|---|---|---|---|
| 321 | 0.99 | 0.98 | 0.98 | 0.99 | 0.99 | 0.99 | 0.97 | 0.98 | 0.96 | 0.96 |
| 328 | 0.98 | 0.99 | 0.98 | 1.00 | 0.99 | 0.99 | 1.00 | 0.98 | 0.99 | 0.97 |
| 335 | 1.01 | 1.00 | 0.99 | 1.00 | 1.00 | 0.98 | 0.99 | 0.99 | 1.00 | 0.97 |
| 349 | 0.99 | 1.01 | 1.01 | 1.01 | 1.02 | 1.01 | 1.01 | 0.99 | 1.01 | 1.03 |
| 356 | 1.01 | 1.03 | 1.02 | 1.00 | 0.99 | 1.01 | 1.01 | 1.03 | 1.00 | 1.02 |
| Average | 1.00 | 1.00 | 1.00 | 1.00 | 1.00 | 1.00 | 1.00 | 0.99 | 0.99 | 0.99 |
| 538 | 0.96 | 1.01 | 0.98 | 0.98 | 0.97 | 0.98 | 0.98 | 0.98 | 0.99 | 0.98 |
| 544 | 0.99 | 0.98 | 0.98 | 0.99 | 0.99 | 0.99 | 0.98 | 0.99 | 1.00 | 0.99 |
| 552 | 1.03 | 0.98 | 0.99 | 0.99 | 1.00 | 1.00 | 1.04 | 0.99 | 1.00 | 1.01 |
| 698 | 0.98 | 1.00 | 1.00 | 0.99 | 1.00 | 1.00 | 1.00 | 1.00 | 0.99 | 1.01 |
| 734 | 1.01 | 1.01 | 1.01 | 1.02 | 1.02 | 1.01 | 0.99 | 1.04 | 1.01 | 1.02 |
| 738 | 1.04 | 1.00 | 1.01 | 1.00 | 1.01 | 1.00 | 1.00 | 0.99 | 1.00 | 0.99 |
| 874 | 1.00 | 1.01 | 1.01 | 1.02 | 1.01 | 1.00 | 1.01 | 1.03 | 1.01 | 0.98 |
| Average | 1.00 | 1.00 | 1.00 | 1.00 | 1.00 | 1.00 | 1.00 | 1.00 | 1.00 | 1.00 |

After manual deglitching the available OLP Version 10 data products were averaged with a 2.5 $\sigma$ clipping using ISAP Version 2.0. Detectors SW1 to SW5 were then smoothed with the nominal resolution element of 0.29 $\mu$m. LW1 to LW5 were smoothed with the nominal resolution of 0.6 $\mu$m and both scans directions averaged.

Note that within the 15 measurements considered, the change in apparent size of Uranus corresponds to a total flux variation of $\sim$10%, which was included in the calculations. The background influence is expected to be less than 0.5% and, therefore, it was not taken into account.

The values obtained show that Uranus does calibrate back to the model and that the calibration is good and repeatable to within a few percent for all detectors.

Looking into the behaviour of each detector more in detail, the same data set for which the results are shown in Table 4.2 were also used to produce Figures 4.3 and 4.4.

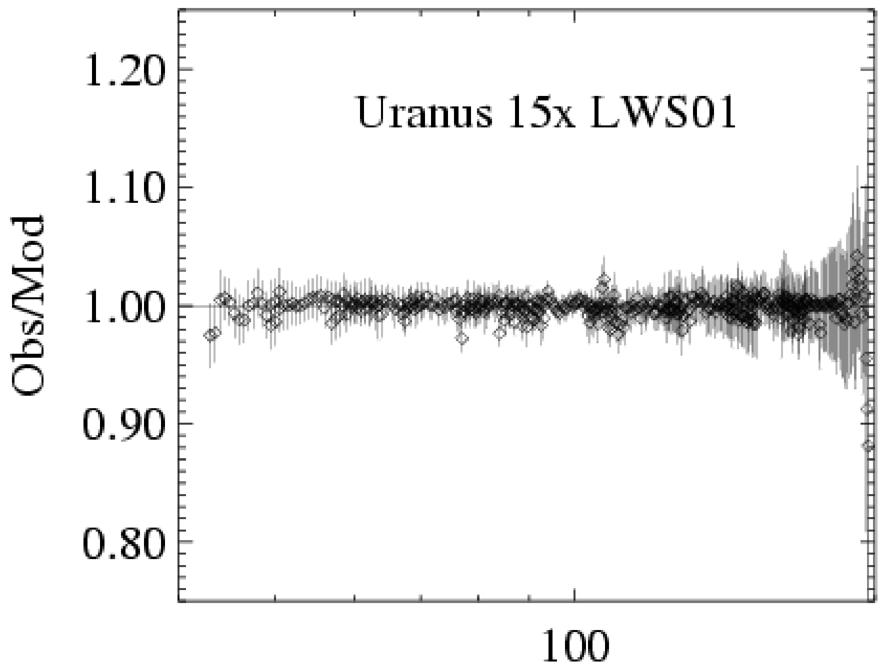


Figure 4.3: *Averaged LWS01 Uranus observations/model ratio for the full LWS wavelength range derived from OLP Version 10 data products.*

As we can see from the averaged observation/model ratios of all 15 measurements the agreement between Uranus model and the calibrated Uranus observations is in most cases within the 2% level. Only SW1 and SW2 show slightly larger deviations at the short wavelength end, as well as LW5, which shows a larger scatter at the long wavelength end.

In general, the reasons for the deviations might be related to the different ways of calculating Uranus fluxes from the brightness temperature model. However, the fluctuations observed in the SW1 detector may be directly connected with a known problem in the RSRF, which produces a conspicuous double-peaked spectral shape observed not only in the spectrum of Uranus but also in all the astronomical sources inspected in the course of our cross-calibration analysis, including planets, asteroids and stars. The relative error induced by this deficient RSRF amounts to 5–10% in flux and its effect is clearly visible in most LWS spectra, as in the few examples plotted in Figure 4.5.

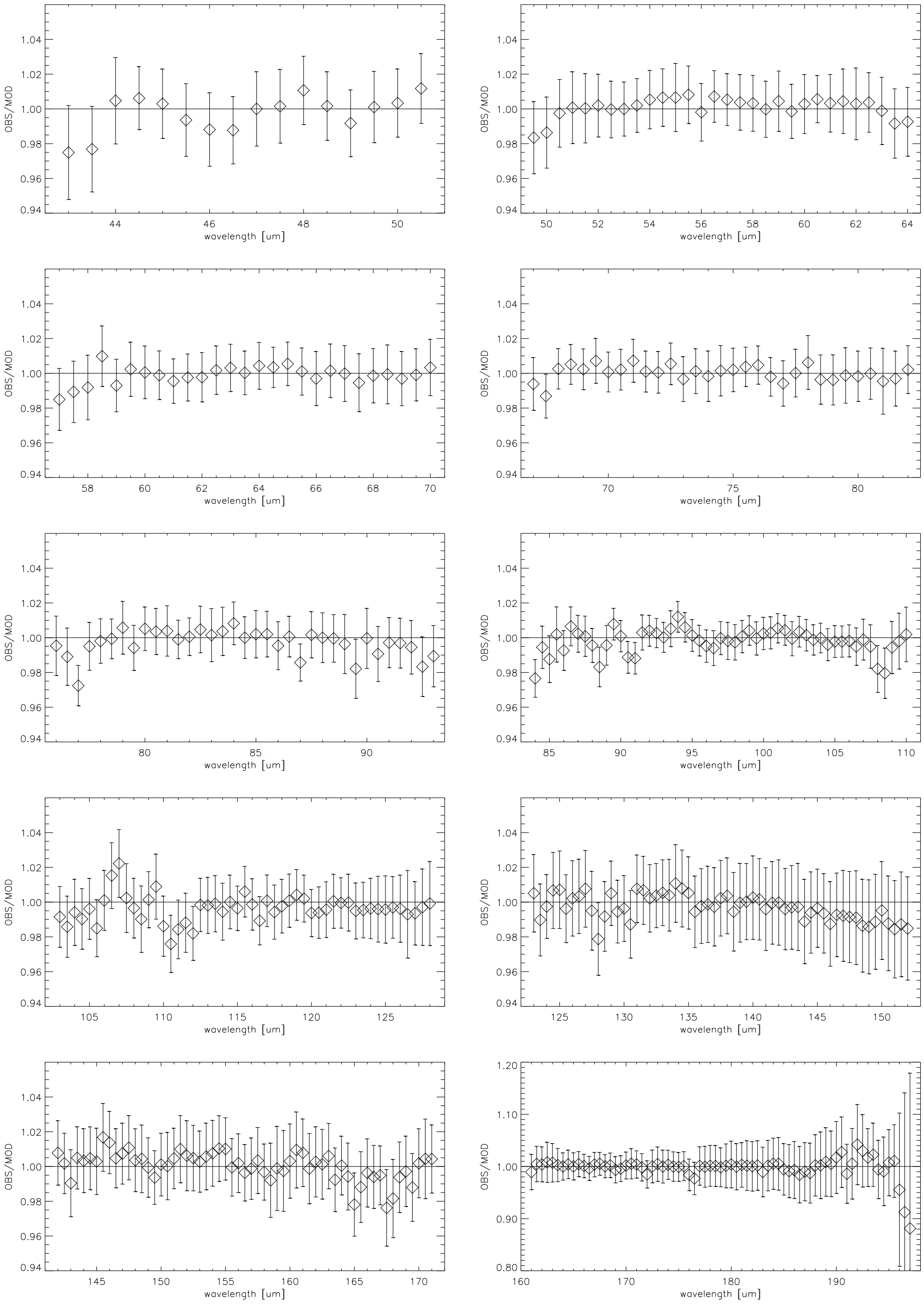


Figure 4.4: *Averaged LWS01 Uranus observations/model ratios per detector derived from OLP Version 10 data products. Error bars represent the standard deviation of the 15 measurements considered.*

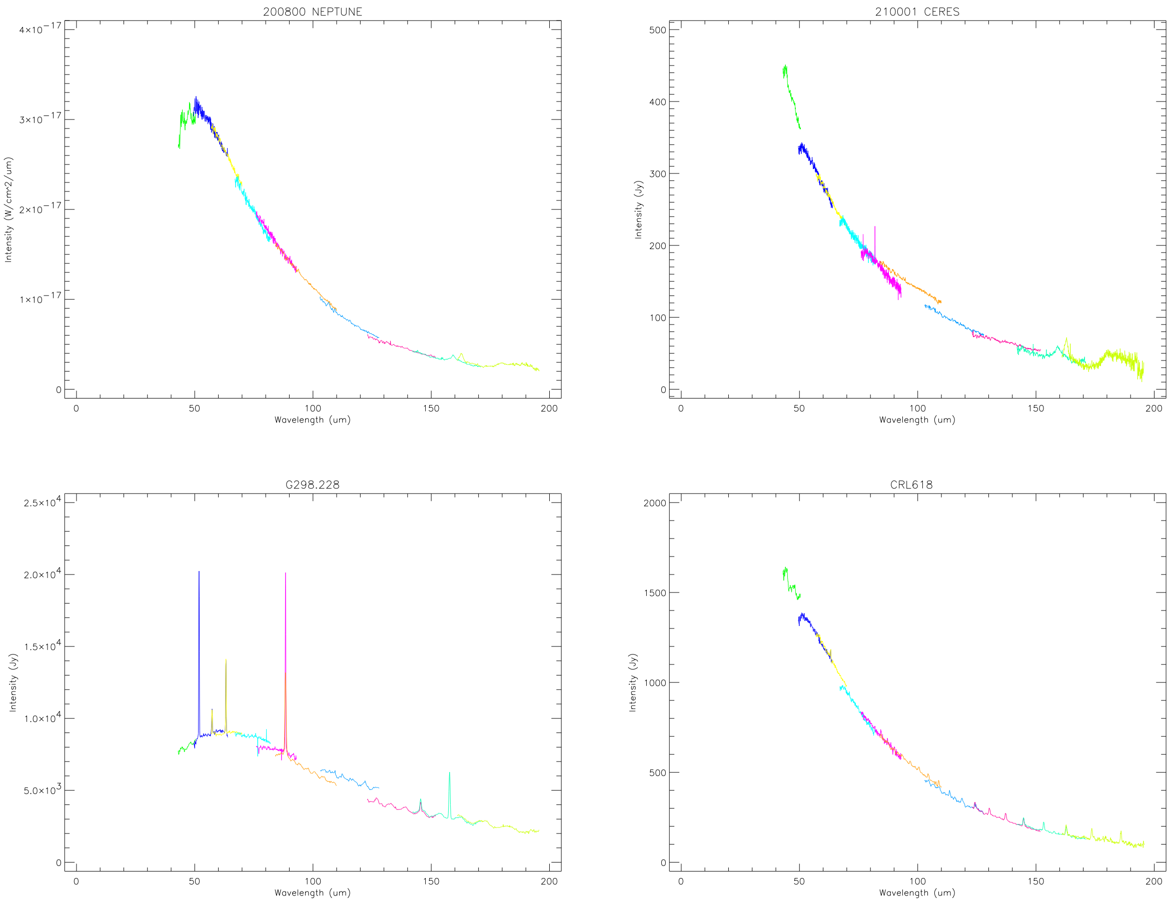


Figure 4.5: *Example of OLP Version 10 LWS spectra of planets (Neptune), asteroids (Ceres), HII regions (G298.228) and proto-planetary nebulae (CRL 618) where the conspicuous double-peaked shape of the SW1 detector is clearly seen at the short wavelength end of the spectra in green colour.*

**LWS02 observations of Uranus**

Thirteen different observations of Uranus taken with the AOT LWS02 (fixed grating LWS spectra) were also retrieved from the ISO Data Archive (OLP Version 10 data products) and analysed in order to check the consistency of this observing mode of LWS.

Only the last 100 s of the detector signal were considered in order to avoid transient effects in the beginning of the measurements. After manual deglitching and dark current subraction using ISAP Version 2.0 (the background values were always smaller than 1% at all wavelengths) we derived the average flux per detector divided by the model.

The agreement found in this case was within the 3% level in general. However, individual observations, especially in SW1 and in the long wavelength detectors LW3, LW4 and LW5 were sometimes off by up to 10% as we can see in Figure 4.6.

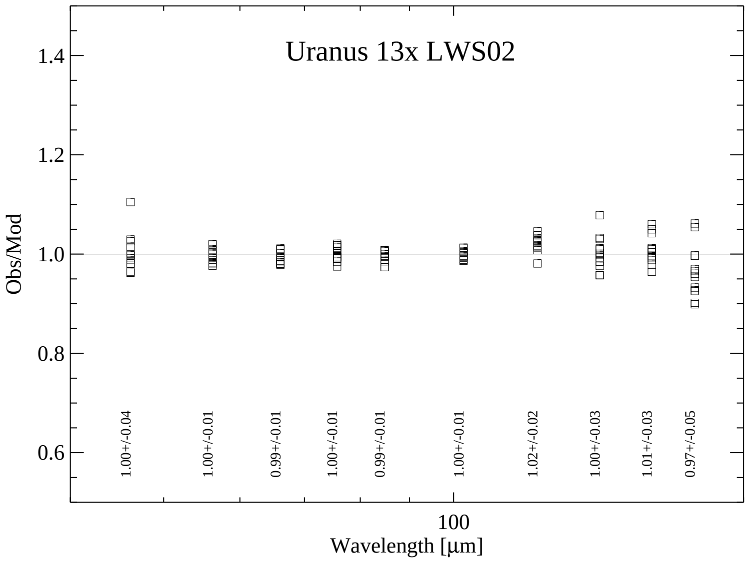


Figure 4.6: *Averaged Uranus LWS02 observations/model ratios for the full LWS wavelength range derived from OLP Version 10 data products.*

.

The average ratios per detector and their standard deviation are listed in Table 4.3.

Table 4.3: *Averaged Uranus LWS02 observations/model ratios per detector derived from OLP Version 10 data products.*

| Detector | <Observations/model> | Detector | <Observations/model> |
|---|---|---|---|
| SW1 | 1.00±0.04 | LW1 | 1.00±0.01 |
| SW2 | 1.00±0.01 | LW2 | 1.02±0.02 |
| SW3 | 0.99±0.01 | LW3 | 1.00±0.03 |
| SW4 | 1.00±0.01 | LW4 | 1.01±0.03 |
| SW5 | 0.99±0.01 | LW5 | 0.97±0.05 |

**LWS observations of Neptune**

Two LWS01 and thirteen LWS02 observations of Neptune retrieved from the ISO Data Archive (OLP Version 10 data products) were analysed in a similar way. The background values for Neptune were again taken from COBE/DIRBE weekly maps (up to 100 $\mu$m) and yearly maps (for wavelengths larger than 100 $\mu$m). The model of Neptune adopted was developed by Orton & Burgdorf (private communication).

LWS01 and LWS02 observations of Neptune agree extremely well. In the full scans detector non-linearities appear as jumps between the individual detectors. In the LWS02 mode (see Figure 4.7), detectors SW2, SW3, SW4 and SW5 have been used as references since they seem to give consistent results for all objects. The other detectors are given relative to these 4 detectors. There is a nice agreement between the observations and model predictions but the model seems to underestimate the overall flux detected by 2%. SW1 is systematically 4–8% too low, LW1 a few percent too high. The stressed Ge:Ga detectors LW2 through LW5 are 5–10% too low, with increasing offsets at longer wavelengths. LW5 shows a larger scatter.

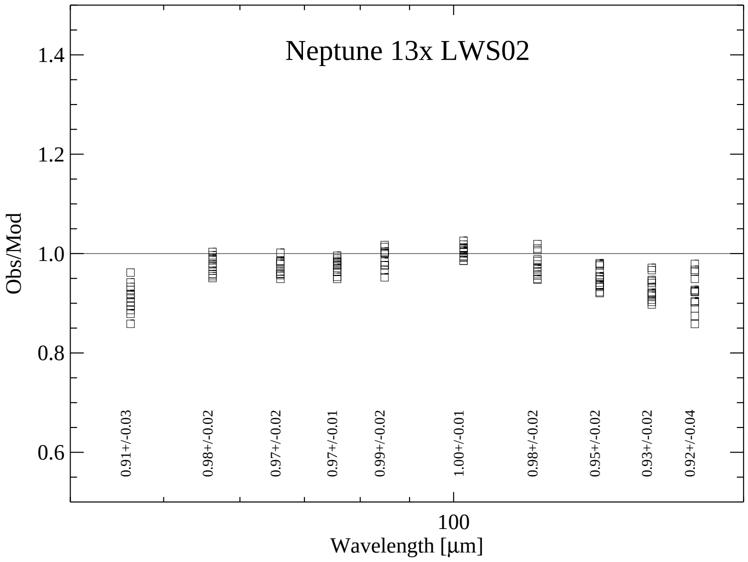


Figure 4.7: *Averaged Neptune LWS02 observations/model ratios for the full LWS wavelength range derived from OLP Version 10 data products.*

.

**LWS observations of asteroids**

The same exercise was performed on a number of asteroids. OLP Version 10 data products were retrieved from the ISO Data Archive and reduced using ISAP Version 2.0 in a similar way as Uranus and Neptune, but here background subtraction becomes quite important. The background values were taken from COBE/DIRBE weekly maps (up to 100 $\mu$m) and yearly maps (for wavelengths larger than 100 $\mu$m). The asteroid models were those produced by Müller & Lagerros 2002, [40].

LWS01 and LWS02 observations agree extremely well. The slight differences found between both observing modes are probably due to transients; LWS02 is less affected by transients since only the last 100 s of each fixed grating position were taken.

- Ceres: A nice agreement (at the 3% level) between observations (15) and model predictions is found for this bright asteroid (see Figure 4.8). SW1 was off in a few cases by up to 20%

as expected when observations taken before revolution 237 (the analysis was done before the correction was implemented in OLP Version 10.1). LW1 was on average 6% too high, LW2 5% too low, LW3 15% too low, while LW4 and LW5 were about 10% too low, but with a larger scatter (10% in LW4 and 20% in LW5).

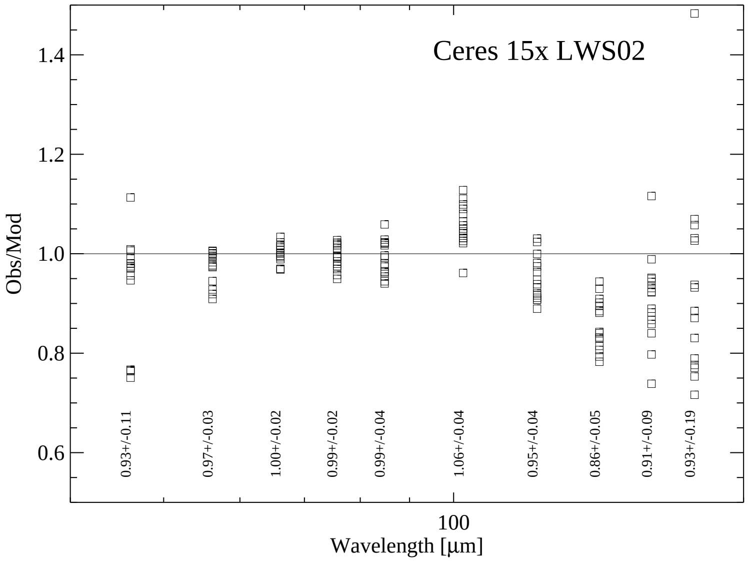


Figure 4.8: *Ceres LWS02 observations/model ratios per detector derived from OLP Version 10 data products. The underestimated SW1 measurements correspond to observations made before revolution 237.*

- Pallas: A nice agreement between observations (4) and model was also found at the 5% level. The SW1 measurement taken before revolution 237 was 15% off, again as expected. LW1 was 10% too high, LW2 12% and LW3 15% too low. Dark current problems in LW4 and LW5 produced too large scatter because of the relatively low flux level of the asteroid at these wavelengths.

- Vesta: The agreement betwen observations (14) and model predictions is at the 5% level, including SW1 (no observations were taken before revolution 237 in this case). LW1 was found 12% too high, LW2 10% and LW3 15% too low. Again, dark current problems in LW4 and LW5 produced a large scatter at these wavelengths.

- Hygiea: The agreement between observations (2) and model predictions is at the 15% level. SW1 is 15% too low in the observations taken before revolution 237 as expected, LW1 11% too high, LW2 20% too low and LW3 30% too low. This asteroid is the faintest in the sample. Therefore, dark current problems were so strong in the LW4 and LW5 bands that they prevented any kind of analysis at these wavelengths.

### LWS01 observations of stars

Stars are among the faintest objects observable with LWS and although detected, the uncertainty in the dark current was in many cases comparable to their flux, particularly at the longer wavelengths. Table 4.4 lists the average observations/model ratios per detector for two of the brightest stars observed with LWS01 as derived from OLP Version 10 data products. The stellar models were taken from the available templates in the Cohen, Walker, Witeborn et al. (CWW) absolute calibration programme (Cohen et al. 1992a, [5]; 1992b, [6]; 1995, [7]; 1996, [8] and 1998, [9]).

The scatter in the values obtained is mainly due to uncertainty in the dark current subtraction. Therefore, no definitive statement can be made about the detector performance, except that the photometric behaviour is still within pre-launch expectations of about 30–50%, even at these very low flux levels.

Table 4.4: *LWS01 observations (averaged per detector) versus model predictions for stars $\alpha$ Boo (Arcturus) and $\alpha$ Tau (Aldebaran). The scatter in the values obtained is mainly due to uncertainty in the dark current subtraction.*

| Detector | Arcturus | | Aldebaran | | |
|---|---|---|---|---|---|
| | Rev 448 | Rev 608 | Rev 818 | Rev 848 | Rev 861 |
| SW1* | 1.15 | 1.16 | 0.93 | 1.14 | 0.73 |
| SW2* | 1.33 | 1.23 | 1.12 | 1.59 | 1.28 |
| SW3* | 1.39 | 1.27 | 1.00 | 1.48 | 1.44 |
| SW4 | 0.57 | 0.71 | 1.35 | 1.31 | 0.83 |
| SW5 | 1.10 | 1.08 | 1.67 | 1.89 | 1.58 |
| LW1* | 1.42 | 1.06 | 1.89 | 1.37 | 1.11 |
| LW2* | 1.22 | 1.18 | 1.53 | 2.05 | 2.01 |
| LW3 | N/A | N/A | 1.50 | 2.38 | 1.53 |
| LW4 | N/A | N/A | 1.49 | 1.75 | -1.05 |
| LW5 | N/A | N/A | 1.81 | 1.68 | -3.24 |

* Detectors affected by NIR leaks.

**LWS02 observations of stars**

Two LWS02 observations of $\alpha$ Boo (Arcturus) were also retrieved from the ISO Data Archive (OLP Version 10 data products) and reduced using ISAP Version 2.0. Background subtraction was again extremely important in this case. The background values were taken from COBE/DIRBE weekly maps (up to 100 $\mu$m) and yearly maps (for wavelengths larger than 100 $\mu$m), as usual, and they represent up to 50% of the total flux for some detectors. The stellar model was taken from the CWW absolute calibration programme.

As we can see in Figure 4.9 detectors SW1, SW3 and SW4 agree within the 20% level with the model, while LW2 and LW3 are systematically too low (30 and 50%, respectively). Detectors SW2 and LW1 were affected by near infrared leak features.

Others stars like $\gamma$ Dra were studied but, unfortunately, they were too faint to perform any kind of analysis with the data products provided by the pipeline.

In summary, OLP Version 10 LWS data products of Neptune, the few asteroids studied and $\alpha$ Boo agree nicely with the model predictions. Observational uncertainties are only large for the fainter asteroids and for some of the stars studied, like $\alpha$ Tau or $\gamma$ Dra, mainly because they are also too faint for LWS.

Appart from the (known) problem affecting detector SW1 before revolution 237, which was corrected in Version 10.1 of the pipeline, detectors LW4 and LW5 usually encounter dark current problems. Manual dark current determinations improve the situation significantly; however, this is only an option for LIA users.

LW1, LW2 and LW3 show systematic effects assuming the COBE derived backgrounds. At the

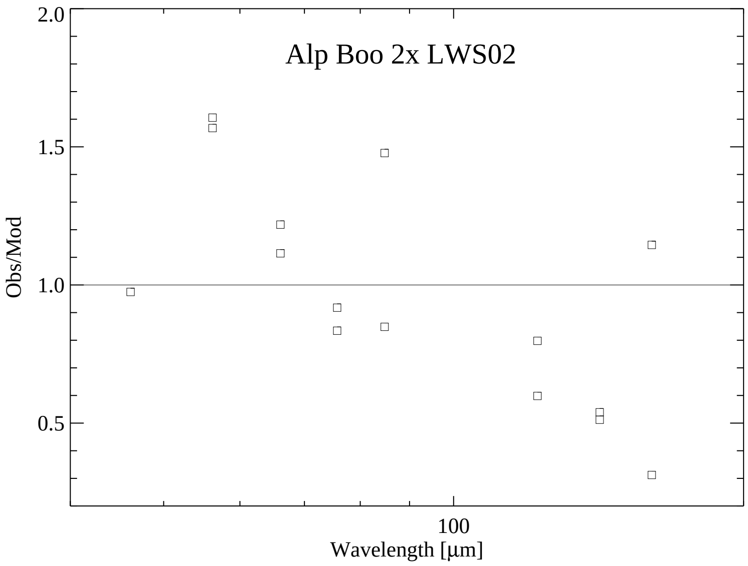


Figure 4.9: *Arcturus ($\alpha$ Boo) LWS02 observations/model ratios per detector derived from OLP Version 10 data products.*

faint end the responsivities possibly depend on the total incoming flux. In the case of LW1 the calibrated fluxes can be up to 15% higher for the faintest sources (as compared to the models). For the stressed detectors LW2 and LW3 the opposite effect is found. Faint sources are systematically underestimated by up to 30% for LW2 and up to 40% for LW3.

A quick comparison with ISOPHOT stressed Ge:Ga detectors reveals the possible nature of this finding. An explanation for the discontinuities observed could come from the known non-linearities shown by stressed Ge:Ga detectors. When going from bright sources (Uranus) to faint sources (stars) the incoming fluxes change by three orders of magnitude. Non-linearity corrections over this flux range can be up to 50% for ISOPHOT. Similar effects could then be expected in LWS detectors.

Although the results are not conclusive, empirical non-linearity corrections have tentatively been derived for LW1, LW2 and LW3, based on the sources here analysed (Neptune, the four asteroids and $\alpha$ Boo). They are available in Müller 2001, [38].

More details on these consistency checks can also be found in Müller & Lagerros 2001, [39].

## 4.3 ISOPHOT

In the case of PHT a large number of consistency checks with models of planets, asteroids and stars were also performed as part of the process of scientific validation of OLP data products (Klaas et al. 2000a, [30]; 2000b, [31]; Klaas & Richards 2002, [32]).

Some of the analysis made are summarised below.

### PHT-S staring observations

Staring PHT-S measurements of some of the calibration stars (HR7001 = Vega, HR 5340, HR 7469, HR 7924, HR 7980 and HR 8487) that were used to establish the dynamic relative spectral response function surfaces of Cal-G file PSDYNAMIC were checked in order to determine whether their input model SEDs were correctly reproduced by the pipeline.

OLP Version 10 data products were retrieved from the ISO Data Archive. Once background subtracted, the SEDs of the stars above mentioned were compared with their flux models (see Figure 4.10).

The results obtained show that the absolute accuracy reached is better than ±10% with a relative spectral shape accuracy better than ±20% for the flux range of 1–8000 Jy with the SS-array and for the flux range of 0.2–1800 Jy with the SL-array.

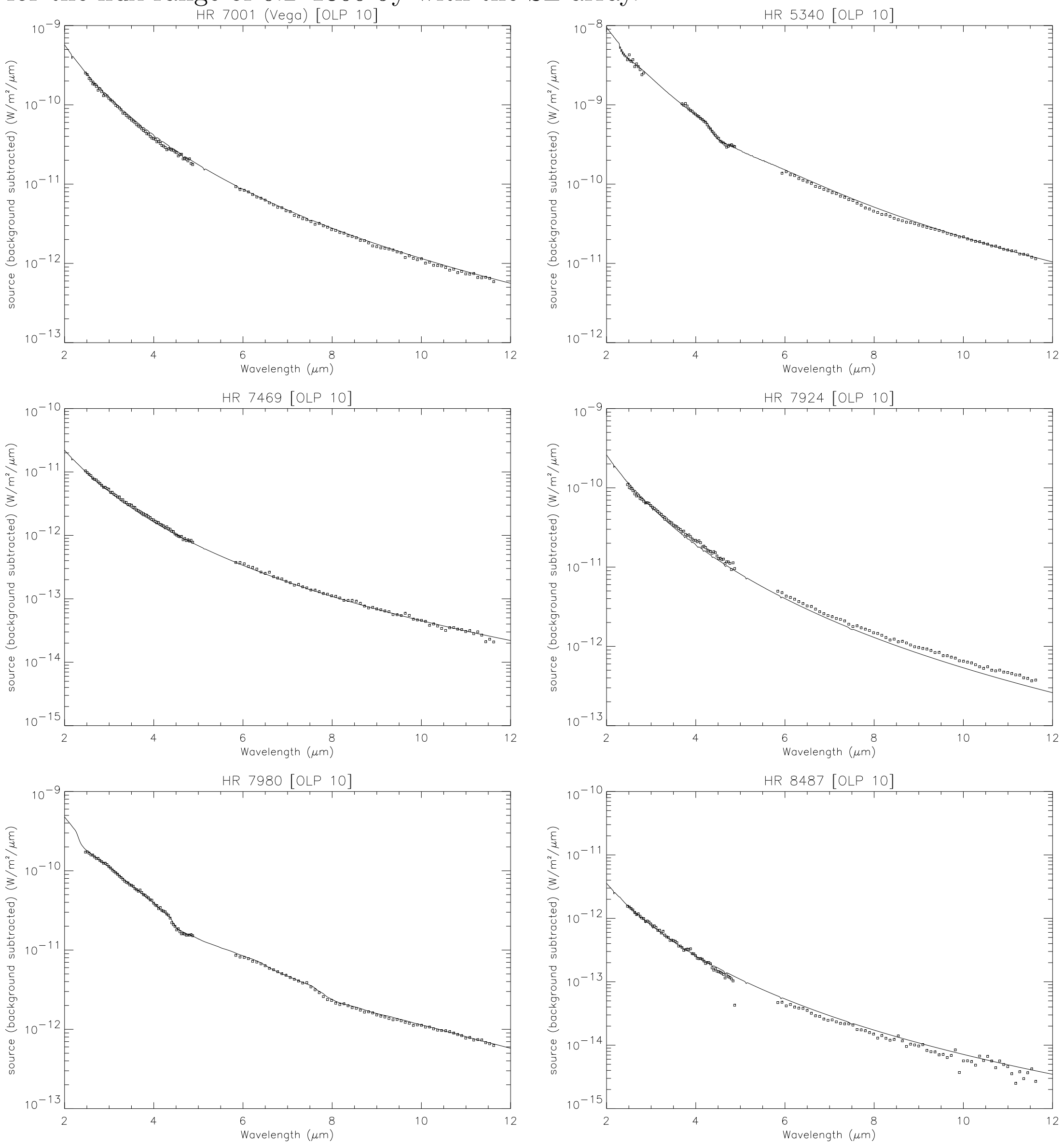


Figure 4.10: *Comparison of the staring OLP Version 10.0 PHT-S spectra of HR 7001 (=Vega), HR 5340, HR 7469, HR 7924, HR7980 and HR 8487 with their model SEDs*

.

To confirm the accuracy of the observing mode the analysis was extended to a small number of non-calibration stars with similar spectral types as the standard stars above mentioned but different brightness, obtaining very similar results (Klaas & Richards 2002, [32]).

**PHT-S chopped observations**

Measurements of two calibration stars (HR 6817 and HR 6847) which were used to establish the Relative Spectral Response Function for chopped PHT-S calibration were checked in order to determine whether their input model SEDs (provided by Hammersley et al. 1998, [22]) were correctly reproduced by the pipeline. Both calibration stars were measured both in rectangular and triangular chopped modes.

OLP Version 10 data products retrieved from the ISO Data Archive show an excellent agreement with the models (see Figure 4.11). Although not shown in Figure 4.11 there is no significant difference in the results between rectangular and triangular chopped mode. The absolute accuracy and the relative spectral shape accuracy are in both cases better than ±10%.

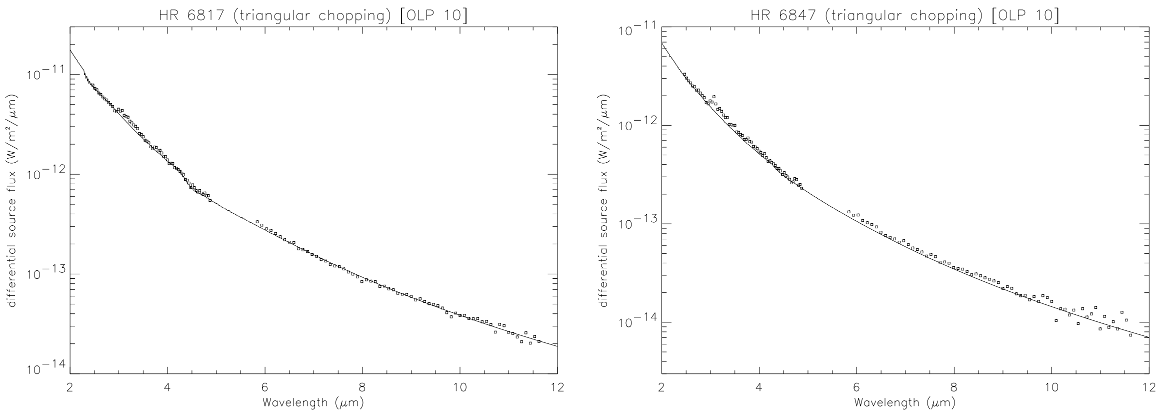


Figure 4.11: *Comparison of the chopped OLP Version 10 PHT-S spectra (only the triangular chopping mode results are shown) of the calibration stars HR 6817 (left) and HR 6847 (right) with their models.*

As for the staring measurements, the analysis was extended to a small number of non-standard stars with different brightness, obtaining very similar results (Klaas & Richards 2002, [32]).

**Multi-filter photometry**

The composite spectra from 1 to 35 $\mu$m extrapolated to 300 $\mu$m provided by Martin Cohen for HR 5340 ($\alpha$ Bootes = Arcturus) and HR 6705 ($\gamma$ Draconis) were compared with observations of these stars taken with PHT-P and PHT-C in the staring modes PHT03 and PHT22 with all the available filters (except the 3.6 and 4.85 $\mu$m filters in the case of HR 5340 because the source saturated the detectors). The comparison plots are shown in Figure 4.12.

The conclusion obtained for HR 5340 is that OLP Version 10 photometry gives a good representation of the SED from 3.3 to 170 $\mu$m (agreement within 10% in most cases), with still some problems at the longest wavelengths where the source flux extraction is more difficult because of the strong background.

In the case of HR 6705, there is a general good agreement from 3 to 100 $\mu$m with the only exception of a measurement at 15 $\mu$m affected by strong transients. The C100 filters are systematically high by 20 to 45%. Adopting a default responsivity calibration for these filters gives fluxes which are lower than the model in contrast with the fluxes derived from actual responsivity calibration. The exception is the 105 $\mu$m filter which is too low both for actual and default responsivity calibration methods. Very likely this is caused by the background subtraction. For C200 filters, no useful results were achieved. The fluxes are all too low or even negative.

Similar analysis performed on other test cases indicate that reliable photometry with the standard on-off staring mode can be obtained up to a lower flux limit of 0.5 Jy for P1 and P2 detectors, 1.5 Jy for P3 and C100 detectors and 2.0 Jy for C200 with slightly worse accuracies in the case of chopped photometry, more affected by transients. Systematic offsets are only

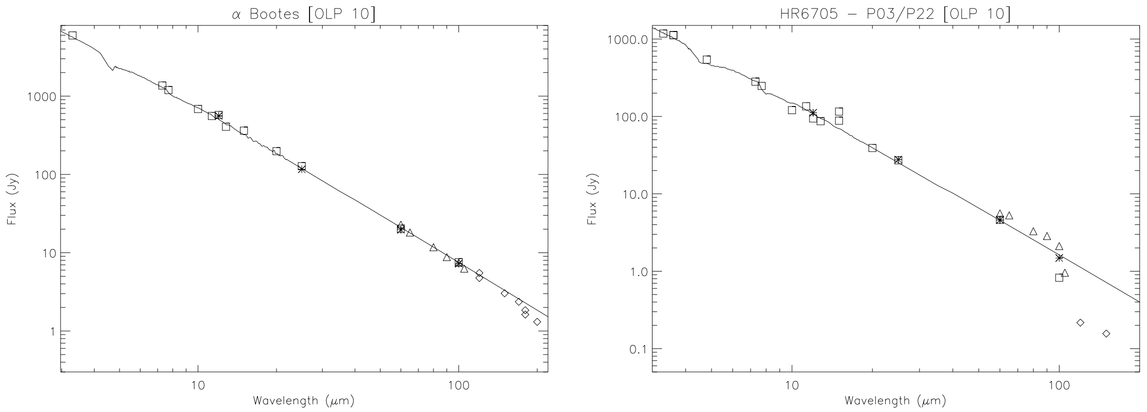


Figure 4.12: *Comparison of PHT-P and PHT-C photometry, using the full ISOPHOT filter set, with the composite spectra extrapolated to 300 $\mu$m of $\alpha$ Bootes (=HR 5340) (left) and $\gamma$ Dra (=HR 6705) (right) provided by M. Cohen and with IRAS photometry for OLP Version 10.0 data products. All photometric points were colour-corrected for a 4000 K blackbody. The meaning of symbols is the following: solid line = model; asterisks = IRAS; squares = PHT-P (PHT03) measurements; triangles = C100 (PHT22) measurements; diamonds = C200 (PHT22) measurements.*

detected for some flux ranges in some filters for staring mode observations as well as for PHT-P photometry in smaller apertures than the standard ones (see Klaas & Richards 2002, [32] for more details).

**Absolute photometry**

PHT05 and PHT25 (absolute photometry) measurements of the calibration star HR 6705 ($\gamma$ Draconis) were compared to the model available from Martin Cohen (composite spectrum from 1 to 35 $\mu$m extrapolated to 300 $\mu$m). The background subtracted, colour-corrected fluxes were compared also with IRAS photometry. The results are shown in Figure 4.13.

The accuracy of the absolute photometry of $\gamma$ Draconis is better than $\pm$15% for all detectors, even for the 170 $\mu$m filter of C200 in contrast to the multi-filter measurement.

A similar analyis was performed with a number of PHT05 observations of HR 2491 (Sirius) covering the range from 3.3 to 25 $\mu$m (see Figure 4.14). In this case the accuracy of the absolute photometry achieved was better than 6% for both P1 and P2 detectors (for the 25 $\mu$m filter a background measurement was performed and the non-negligible background flux was subtracted from the on-target flux).

Similar results on absolute photometry (PHT05) were found when the comparison was made using observations of $\alpha$ Ari (HR 617) up to 100 $\mu$m. The background subtracted, colour-corrected flux values derived from OLP Version 10.0 data products are shown in Figure 4.15.

Accuracies are found to be better than 10% over the full P1 filter range, except for the three filters centred at 4.8, 11.3 and 12.8 $\mu$m. The 4.8 $\mu$m filter colour correction appears to be not appropriate due to an underlying strong absorption feature. For P2 detectors the background subtraction was performed using COBE/DIRBE fluxes since background measurements were not taken with ISOPHOT. Once this background contribution is removed, the accuracy of the P2 absolute photometry is also found to be better than 10%.

Finally, OLP Version 10 data products corresponding to C200 absolute photometric mode (PHT25) observations of Uranus at 120 and 200 $\mu$m were also compared against the Uranus model produced by Griffin & Orton 1993, [18].

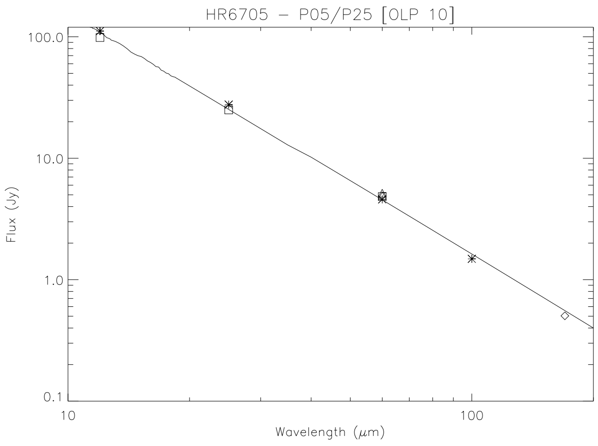


Figure 4.13: *Comparison of PHT-P and PHT-C absolute photometry with the composite spectrum of $\gamma$ Draconis (HR 6705) provided by M. Cohen and with IRAS photometry for OLP Version 10.0 data products. All photometric points are colour-corrected for a 4000 K blackbody. The meaning of the symbols is the following: solid line = model; asterisks = IRAS; squares = PHT-P (PHT05) measurements; triangles = C100 (PHT25) measurements; diamonds = C200 (PHT25) measurements.*

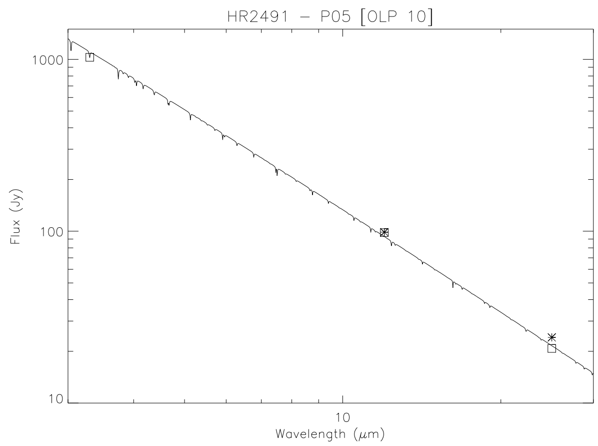


Figure 4.14: *Comparison of PHT-P absolute photometry with the composite spectrum of Sirius (HR 2491) provided by M. Cohen and with IRAS photometry for OLP Version 10.0 data products. All photometric points are colour-corrected for a 10000 K blackbody. The meaning of the symbols is the following: solid line = model; asterisks = IRAS; squares = PHT-P (PHT05) measurements.*

Figure 4.16 shows the results obtained where we can see that the measurements are within the 5% level of agreement.

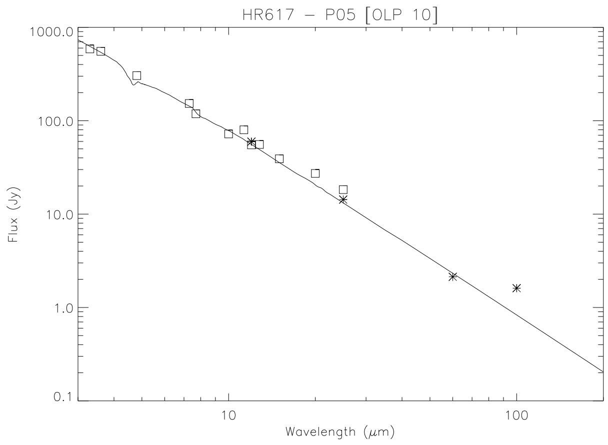


Figure 4.15: *Comparison of PHT-P absolute photometry with the composite spectrum of α Ari (HR 617) provided by M. Cohen and with IRAS photometry for OLP Version 10.0 data products. All photometric points are colour-corrected for a 4000 K blackbody. The meaning of the symbols is the following: solid line = model; asterisks = IRAS; squares = PHT-P (PHT05) measurements.*

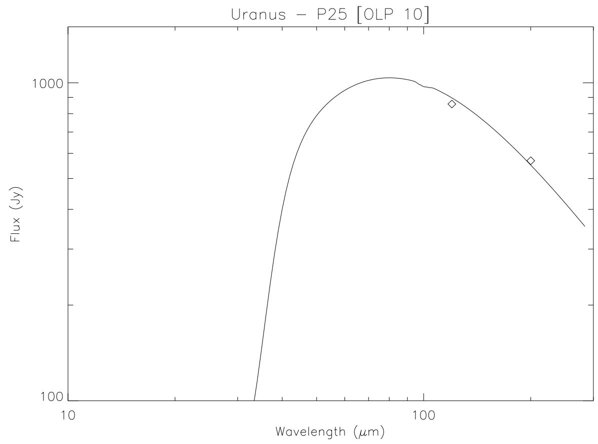


Figure 4.16: *Comparison of C200 OLP Version 10.0 absolute photometry of Uranus with the model. All photometric points are colour-corrected for a 60 K blackbody. The meaning of the symbols is the following: solid line = model; diamonds = C200 (PHT25) measurements.*

## 4.4 SWS

Detailed cross-calibration comparisons were made by Decin 2001, [13] between a few OLP Version 8.4 spectra of bright stars observed with SWS and their corresponding synthetic spectra from 2.38 to 12 $\mu$m derived using the MARCS-code (Gustafsson et al. 1975, [**?**] and subsequent updates).

The purpose of this study was to determine the origin of the small discrepancies emerged from the confrontation between SWS OLP Version 8.4 spectra and the theoretical spectra leading both to improvements in the calibration of SWS and on the theoretical description of stellar atmospheres. This data set was used to improve the flux calibration of SWS bands 1 and 2 in OLP Version 10.

The broad-band shape of the relative spectral response function (RSRF) was as of OLP Version 8.4 already quite accurate in band 1. However, some improvements were made at the beginning of band 1A and a fringe pattern recognized at the end of band 1D was also corrected in OLP Version 10. The final accuracy of SWS in band 1 is estimated to be better than 2%.

In band 2 the calibration improved also with respect to previous calibrations in OLP Version 10, but still some problems exist. Due to the new model for memory effect correction based on the Fouks-Schubert model and developed by Do Kester (Kester 2001, [**?**]) the problems with the memory effects are now under control, at least when the flux jumps are not too high.

By making a comparison between the SWS data and the theoretical models first as a function of the spectral type and then as a function of the absolute flux value (see Figures 4.17 and 4.18) it was possible to distinguish between problems affecting OLP Version 8.4 which were spectral type related -i.e., problems with the theoretical predictions of the model - and problems which were flux, and so memory effect, related. This way it was learned that:

- A bump of $\sim$2.5% in the wavelength range from 4.08–4.30 $\mu$m present both in hot and cool stars, in low-flux as well as in high-flux sources is indicative of problems with the RSRF.
- From 4.75 to 4.85 $\mu$m, a sligt increase ($\sim$1%) is noticeable. Once more, an indication of a small problem with the RSRF.
- At the end of band 2A, a quite different behaviour for all the stars emerges. Further inspection indicates that we see a combination of problems with the memory-effect correction, synthetic predictions and, consequently, maybe also with the RSRFs. When we look at Figure 4.17 we can recognize a same — increasing — trend for $\beta$ Peg, $\alpha$ Cet, $\beta$ And and $\alpha$ Tau, the coolest stars in the sample and so indicating a problem with the synthetic predictions. This behaviour is however not visible for HD 149447, whose spectral type is in between $\beta$ And and $\alpha$ Tau. An analogous discrepancy is visible for $\delta$ Dra with respect to the stars with almost the same effective temperature. Looking now at Figure 4.18 we see that HD 149447 and $\delta$ Dra (together with Vega and $\alpha$ Tuc) have almost the same absolute flux-level in band 2A and show the same trend (decreasing slope) in this plot, indicating a problem with the correction for memory-effects, a statement which is confirmed when we compare the up-scan and down-scan data.

The majority of discrepancies encountered in bands 2B and 2C are due to still existing problems with the memory-effect correction and smaller problems with the RSRFs. This kind of exercise gives us, however, also an idea on the relative accuracy in band 2 for OLP Version 8.4: an accuracy of better than 6 %, which is — taking into account the problematic behaviour of the detectors in band 2 — a very good result, which may have been slightly improved in OLP Version 10 with the latest iteration in the determination of the RSRFs.

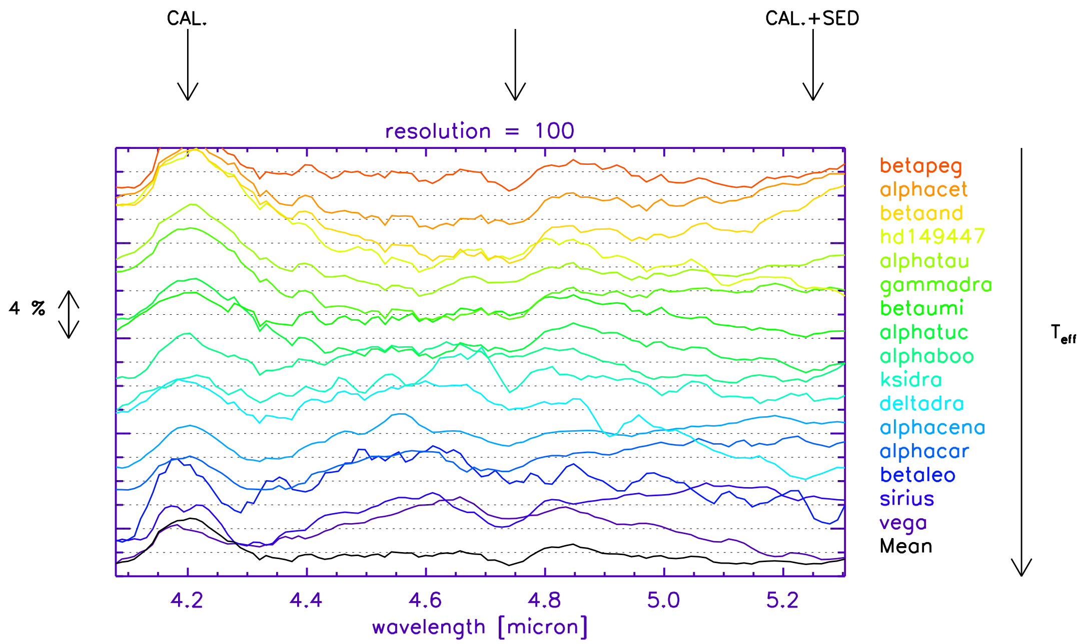


Figure 4.17: *Division between OLP Version 8.4 SWS AOT01 data and their theoretical predictions at a resolving power of 100. The synthetic spectra are calculated using as stellar parameters the values determined from band 1 data. In this figure, the stars are ordered by spectral type. The mean of the different, coloured, divided spectra is given in black at the bottom of the figure (from Decin 2001, [13]).*

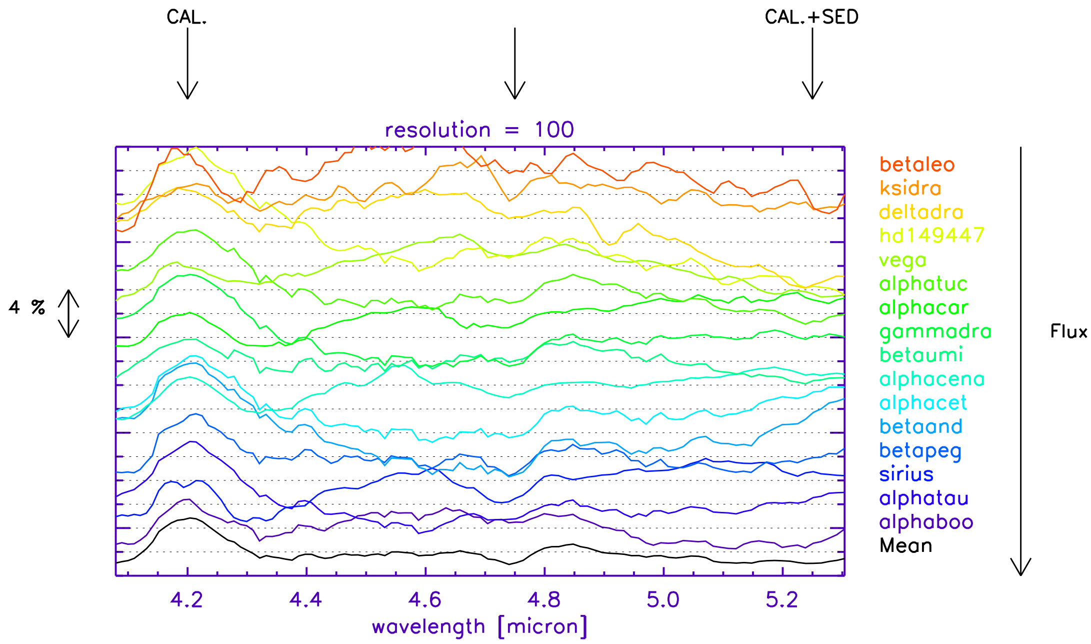


Figure 4.18: *Division between OLP Version 8.4 SWS AOT01 data and their theoretical predictions at a resolving power of 100. The synthetic spectra are calculated using as stellar parameters the values determined from the band-1 data. In this figure, the stars are ordered by absolute-flux value. The mean of the different, coloured, divided spectra is given in black at the bottom of the figure (from Decin 2001, [13]).*

The new set of synthetic spectra resulting from the work by Leen Decin was used to improve the calibration of OLP Version 10, while in OLP Version 8.4 models provided by Martin Cohen were used. Thus, a confrontation between the two sets may be instructive. Several stars are in common between the two samples: i) Vega and Sirius, for which Cohen has constructed a calibrated model spectrum; ii) a composite spectrum (i.e. various observed spectra have been spliced to each other using photometric data) is available for $\alpha$ Cen A, $\alpha$ Boo, $\gamma$ Dra, $\alpha$ Tau, $\beta$ And, $\alpha$ Cet and $\beta$ Peg; iii) a template spectrum (i. e. a spectrum made by using photometric data of the star itself and the shape of a 'template' star) is built for $\delta$ Dra (template: $\beta$ Gem: K0 III), $\xi$ Dra (template: $\alpha$ Boo: K2 IIIp), $\alpha$ Tuc (template: $\alpha$ Hya: K3 II-III) and HD 149447 (template: $\alpha$ Tau: K5 III). One should notice that for the composite spectrum of $\gamma$ Dra, no spectroscopic data were available at that time in the wavelength range from 1.2 $\mu$m till 5.5 $\mu$m. The spectrum of $\alpha$ Tau has therefore been used to construct the composite spectrum of $\gamma$ Dra in this wavelength range.

In order to ensure independency of the absolute-flux level of the SWS data, the angular diameters of the synthetic spectra were determined by using the photometric data of Cohen, JKLM data from Hammersley's GBPP broad-band photometry, IRAS data and some other published photometric data cited in the IA_SED data-base. A comparison between the (high-resolution) synthetic spectra, SEDs of Cohen and used photometric data is given in Figure 4.4. The obtained angular diameters $\theta_d$ (in $mas$) for the stellar sources are mentioned in the figure.

The most remarkable discrepancies between the two spectra arise in the CO and SiO molecular bands, where the molecular bands are consistently across the sample stronger in the composites of Cohen. Cohen used low-resolution NIR and KAO data to construct this part of the spectrum. Comparing these synthetic spectra with OLP Version 8.4 SWS data (whose calibration is not based on our results) and the high-resolution Fourier Transform Spectrometer (FTS) spectrum of $\alpha$ Boo published by Hinkle et al. 1995, [25] (see Figure 4.5 in Decin 2000, [12]), we did however see that the strongest, low-excitation, CO lines were always predicted as being somewhat too *strong* (a few percent at a resolution of 50000 for the FTS spectrum), probably caused by a problem with the temperature distribution in the outermost layers of the theoretical model (Decin et al. 2003, [14]). Moreover, a comparison between the high-resolution synthetic spectrum of $\alpha$ Boo with its FTS spectrum shows also a good agreement for the high excitation CO $\Delta v = 1$ lines, the low excitation lines being predicted as too weak. The few percent disagreement between FTS and synthetic spectrum will however never yield the kind of disagreement one sees between the low resolution synthetic spectra and the SED data. The CO $\Delta v = 2$ discrepancy visible in $\gamma$ Dra results from using the $\alpha$ Tau observational KAO data. Since $\alpha$ Tau and $\gamma$ Dra have a different set of stellar parameters, with $\alpha$ Tau having a significant larger amount of carbon, the SED of Cohen for $\gamma$ Dra displays too strong a CO feature. One should also be heedful of this remark when judging upon the quality of the template spectra for $\delta$ Dra, $\xi$ Dra, $\alpha$ Tuc and HD 149447.

As conclusion, we may say that the SED spectra of Cohen are excellent (and consistent) for the absolute calibration of an instrument, but that attention should be paid when using them for relative flux calibration.

This kind of analysis, which has been proven to be very adequate, will be applied also to bands 3 and 4 in the future.

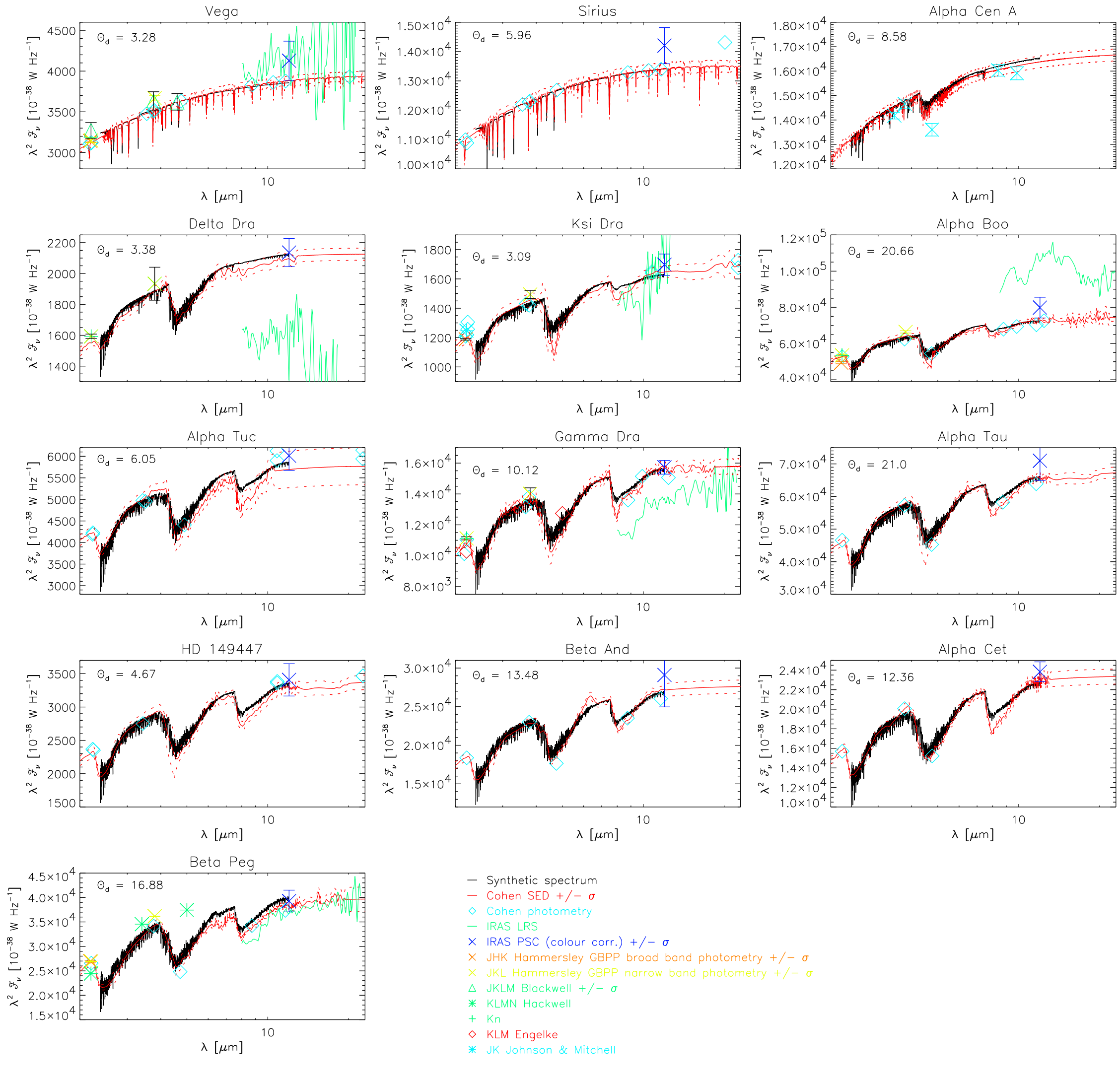


Figure 4.19: *Comparison between the synthetic spectra of the standard stellar sources, their SED of Cohen and various photometric datapoints taken from the literature.*

# Chapter 5

# ISO versus ground-based measurements

## 5.1 ISO SWS versus UKIRT observations

ISO SWS01 and SWS06 observations of a number of proto-planetary nebulae (PPNe) were analysed and compared with results obtained on the same set of targets with IRAS, KAO and UKIRT by Hrivnak et al. 2000, [27].

The SWS01 observations were carried out in a variety of scan speeds covering the full spectral range from 2.4 to 45 $\mu$m. Some of the sources were observed also in the SWS06 mode between 16.5 and 24 $\mu$m in order to detect the presence and study in more detail (higher spectral resolution) the still unidentified 21 $\mu$m feature usually associated to stars in this short evolutionary stage.

The SWS01 data reduction was carried out using OLP Version 7 of the standard pipeline processing. Further manual processing was performed also with ISAP Version 1.6. Basically, bad data points were removed, and the full set of data values was averaged to produce the final spectra with a uniform wavelength spacing in bands 1 to 3D and in bands 3E and 4. Band 4 was found severely affected by glitches, and it was not always possible to remove them in a satisfactory manner (a lower resolution was selected in these cases to plot the data).

In most cases the SWS01 data had strong problems in band 3E (27.5–29.0 $\mu$m), which is known to be subject to more noise.

In order to assess the flux calibration carried out this way the ISO spectra were compared to previously existing data on the same sources from IRAS (LRS spectra), ground-based (UKIRT CGS3 observations) and Kuiper Airborne Observatory (KAO) observations.

The IRAS LRS spectra were taken from the IRAS database at Calgary (note that they were flux calibrated against the 12$\mu$m flux IRAS photometry) while UKIRT spectra were taken from Justtanont et al. 1996, [29] and KAO observations are described in Omont et al. 1995, [41].

The result of this cross-calibration comparison is shown in Figure 5.1. The various data sets have not been shifted in any way. As we can see, there is an excellent agreement in most cases. This is usually better than the 10–15% level between all instruments and observing modes with two remarkable exceptions. These are IRAS 19477+2401 and IRAS 18576+0341, which have clearly been observed by ISO with the source off-centre, since the SWS spectra is well below the flux level at which these sources were detected using other facilities and show the characteristic flux jumps already mentioned in this document usually associated to badly pointed observations. Although not so clear, a similar pointing problem might be affecting the spectrum of IRAS 01005+7910.

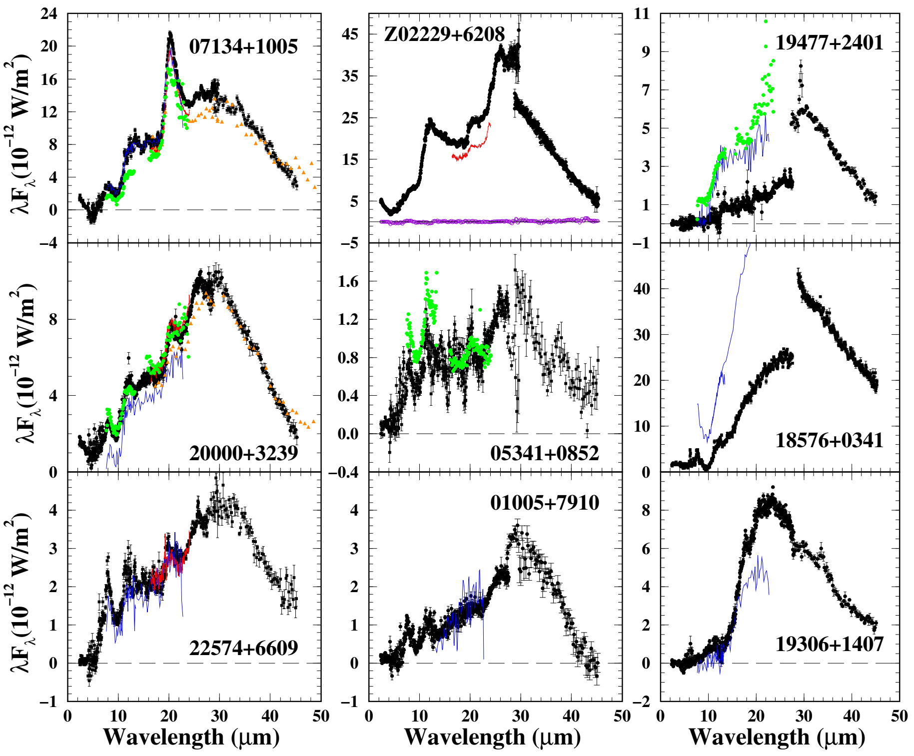


Figure 5.1: *ISO SWS01 spectra (black squares), plotted with error bars. Plotted for comparison are IRAS LRS (blue lines), UKIRT CGS3 (green circles), KAO (orange triangles) and ISO SWS06 (red lines) spectra. No scaling factors have been applied to the ISO data (from Hrivnak et al. 2000, [27]).*

Appart from these obvious strong effects, the only other remarkable discrepancy is observed between the SWS01 and the SWS06 observation of Z02229+6208 (25% difference), not yet understood. The IRAS 12 $\mu$m photometry is in close agreement with the SWS01 spectrum while the 25 $\mu$m band is in agreement with the flux level of the SWS06 observation. The observations were taken 4 days apart but we do not expect such a strong flux variation in that small period of time.

The rest are minor differences which appear to reflect the levels of the precision in the calibrations of the various instruments.

Observations of four of the stars in the sample were also taken with PHT-S in the spectral region covering from 2.5 to 11.6 $\mu$m. The data were taken in staring mode for IRAS Z02229+6208 and IRAS 20000+3239 and in chopped mode for the two fainter sources, IRAS 01005+7910 and 19306+1409. They were reduced using PIA Version 7.3.2. The absolute flux calibration was carried out using the dynamic calibration method to correct the PHT-S staring spectra for transient effects and the special chopped mode calibration for the chopped observations.

The results are plotted in Figure 5.2 together with the rest of available data. Note that in this plot correction factors of 1.50, 2.92 and 1.82 have been applied respectively to the SWS01 spectra of IRAS 01005+7910, IRAS 19477+2401 and IRAS 18576+0341 to remove the effect of flux losses due to bad pointing.

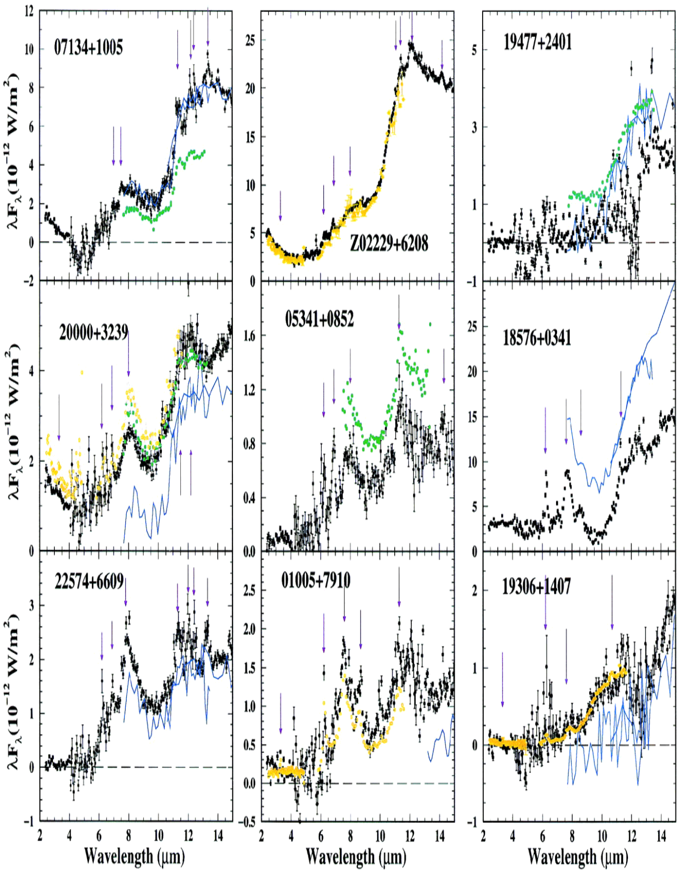


Figure 5.2: *Expanded plot of the ISO SWS01 spectra in the 2–15 μm region, with ISO PHT-S (orange circles) spectra included, and spectral features marked by arrows. Other symbols are the same as in the previous Figure. The SWS flux densities for IRAS 01005+7910, 19477+2401, and 18576+0341 have been scaled by factors of 1.50, 2.92, and 1.82, respectively, while a scale factor of 0.76 was applied to the PHT-S spectrum of IRAS 20000+3239, as discussed in the text (from Hrivnak et al. 2000, [27]).*

In all cases PHT-S and SWS01 spectra agree well in shape where the source is bright enough to have a good quality SWS01 spectrum. The PHT-S data are shown to be particularly valuable as a supplement to SWS01 band 2 data, especially for detection of faint features in this wavelength range such as the 3.3 $\mu$m unidentified infrared feature. The agreement in flux level is good for all sources except for IRAS 20000+3239, for which the PHT-S spectrum was found 30% higher than the SWS01 spectrum.

Comparison with broadband photometry showed that the PHT-S observations for IRAS 20000 +3239 were too high in flux density for unknown reasons while the SWS01 observations agreed with the photometry. Therefore, a scale factor of 0.76 was applied to the PHT-S data for this object and produced good agreement with the SWS01 data.

## 5.2 An example of multi-wavelength cross-calibration

ISO SWS and staring PHT-S observations of the bipolar proto-planetary nebula Hen 401 (= IRAS 10178−5958) have been used in combination with ultraviolet (IUE) spectroscopy, optical and near infrared ground-based photometry and IRAS photometry at 12, 25, 60 and 100 $\mu$m to reconstruct the overall spectral energy distribution of this source from 1150 Å to 100 $\mu$m.

The full range (speed 1) SWS01 spectrum, originally standard pipe-line processed with OLP Version 8.4, was reprocessed using OSIA Version 1.0. All detector signals were inspected for spurious features (small jumps and glitches) which were removed. A flux depression originally observed in band 3E of the SWS spectrum was identified as an artifact and, thus, the emission of this band was manually shifted to match the flux level of the adjacent bands 3D and 4.

The PHT-S spectrum, taken in staring mode and also originally standard processed with OLP Version 8.4 was further inspected for residual glitches not detected by the pipeline and corrected for transients using the available dynamic calibration method as it was implemented in PIA Version 8.1.

Figure 5.3 shows the ISO SWS spectrum and the ISO PHT-S spectrum of Hen 401 in their overlapping spectral range. A first inspection reveals the presence of PAH features at 3.3, 6.2, 7.7, 8.6 and 11.3 $\mu$m, suggesting a C-rich nature of the circumstellar envelope, overimposed on a cool continuum. A comparison between the two ISO spectra shows a very nice agreement both in the overall shape and in the absolute flux level (within 10%) as well as with the IRAS photometry at 12 $\mu$m, which is also plotted for comparison.

In Figure 5.4 we show the ISO results plotted together with IRAS photometry at 12, 25, 60 and 100 $\mu$m, the IUE spectrum, ground-based optical BVRI photometry and near infrared

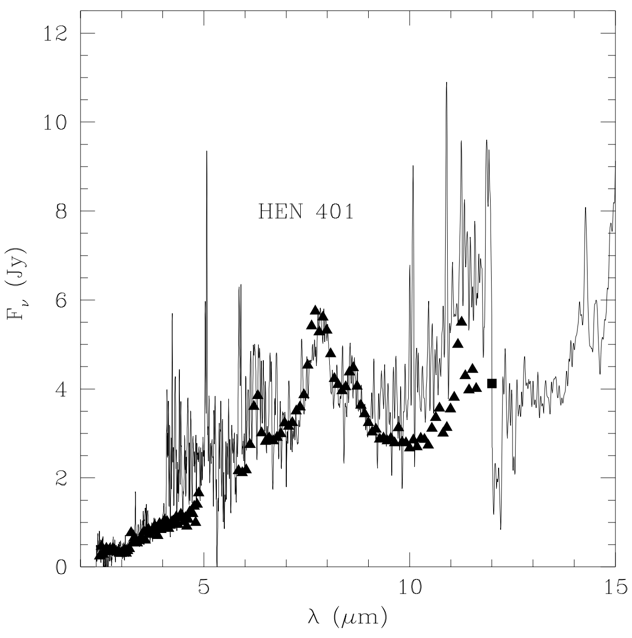


Figure 5.3: *Comparison between the SWS spectrum (solid line) and the PHT-S spectrum (red filled triangles) of Hen 401 where we show how the faint PAH spectral features detecetd both in SWS and PHT are in very nice agreement. Note also the agreement in absolute flux level of both instruments with the IRAS photometry at 12 $\mu$m (blue square) - from Parthasarathy et al. 2001, [42].*

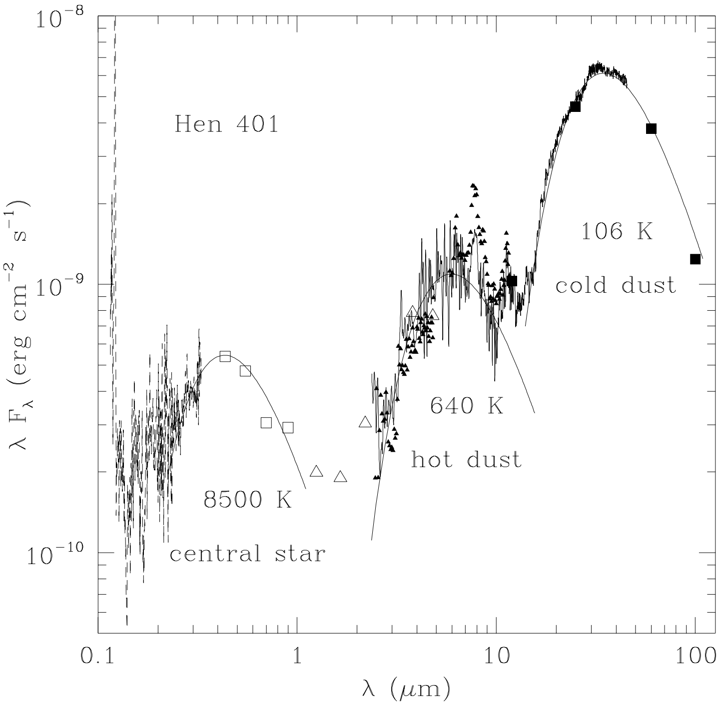


Figure 5.4: *The flux distribution of Hen 401 from the UV to the infrared. ISO SWS (solid line), PHT-S (filled triangles) and IUE data (dashed line) are plotted together with ground-based optical BVRI (open squares), near infrared JHKL'M (open triangles) and the IRAS photometry at 12, 25, 60 and 100 $\mu$m (filled squares) - from Parthasarathy et al. 2001, [42].*

photometry taken in the J, H, K, L' and M filters at the 1m ESO telescope (La Silla, Chile) As we can see, there is a nice consistency also with the results coming from the various other sources of information.

The full multi-wavelength analysis of this source can be found in Parthasarathy et al. 2001, [42].

**Acknowledgements:**

Many people working at the ISO Data Centre and at the National Data Centres have contributed to the results here presented. They are too numerous to name individually but the improvements in ISO calibration would have never been possible without their enthusiastic dedication to the Project.

# Bibliography


[1] Brauher J.R. & Lord S.D. 2001, *The ISOLWS-IRAS cross-calibration of extragalactic sources*, in 'The Calibration Legacy of the ISO Mission', Eds. L. Metcalfe et al., ESA SP-481 (in press)

[2] Cesarsky D.A. 2002, *Validation Report for CAM OLP Version 10*, Version 0.3, March 2002 (see ISO documentation under `http://www.vilspa.esa.es`)

[3] Cesarsky D., Jones A.P., Lequeux J. & Verstraete L. 2000, *Silicate emission in Orion*, A&A 2000, 358, 708

[4] Chan S.J., Lloyd C., Swinyard B.M. & Lim T. 2001, in 'The Calibration Legacy of the ISO Mission', Eds. L. Metcalfe et al., ESA SP-481 (in press)

[5] Cohen M., Walker R.G., Barlow M.J. & Deacon J.R. 1992a, *Spectral irradiance calibration in the infrared. I - Ground-based and IRAS broadband calibrations*, AJ 104, 1650

[6] Cohen M., Walker R.G., Witteborn F.C. 1992b, *Spectral irradiance calibration in the infrared. II - $\alpha$ Tau and the recalibration of the IRAS low resolution spectrometer*, AJ 104, 2030

[7] Cohen M., Witteborn F.C., Walker R.G., Bregman J. & Wooden D. 1995, *Spectral Irradiance Calibration in the Infrared. IV - 1.2–35 micron spectra of six standard stars*, AJ 110, 275

[8] Cohen M., Witteborn F.C., Carbon D.F., Davies J.K., Wooden D. & Bregman J. 1996, *Spectral irradiance calibration in the infrared. VII - New composite spectra, comparison with model atmospheres, and far-infrared extrapolations*, AJ 112, 2274

[9] Cohen M., Witteborn F.C., Roush T., Bregman J. & Wooden D. 1998, *Spectral irradiance calibration in the infrared. VIII - 5–14 micron spectroscopy of the asteroids Ceres, Vesta and Pallas*, AJ 115, 1671

[10] Crovisier J., Leech K., Bockelée-Morvan D. et al. 1997, *The infrared spectrum of comet Hale-Bopp*, in 'First ISO workshop on analytical spectroscopy', Eds. A.M. Heras, K. Leech, N.R. Trams & M. Perry, ESA SP-419, 137

[11] Crovisier J., Brooke T.Y., Leech K. et al. 2000, *The thermal infrared spectra of comets Hale-Bopp and 103 P/Hartley 2 observed with the Infrared Space Observatory*, in 'Thermal Emission Spectroscopy and Analysis of Dust Disks and Regoliths', Eds. M.L. Sitko, A.L. Sprague & D.K. Lynch, ASP Conf. Ser. 196, 109

[12] Decin L. 2000, Ph.D. Leuven University, Belgium

[13] Decin L. 2001, *Stellar models in IR calibration*, in 'The Calibration Legacy of the ISO Mission', Eds. L. Metcalfe et al., ESA SP-481 (in press)

[14] Decin L., Vandenbussche B., Waelkens C., Decin G., Eriksson K., Gustafsson B., Plez B., Sauval A.J. 2003, *ISO-SWS calibration and the accurate modelling of cool-star atmospheres. IV. G9 to M2 stars*, A&A 400, 709

[15] Dotto E., Barucci M.A., Müller T.G., Brucato J.R., Fulchignoni M., Mennella V. & Colangeli L. 2002, *ISO observations of low and moderate albedo asteroids*, A&A 393, 1065

[16] Egan M.P., Price S.D., Moshir M.M., Cohen M. & Tedesco E. 1999, *The Midcourse Space Experiment Point Source Catalog Version 1.2 Explanatory Guide*, Technical Report AFRL-VS-TR-1999-1522

[17] Fouks B.I. & Schubert J. 1995, *Precise theoretical description of photoresponse for detectors of ISOPHOT's Si:Ga array*, Proc. SPIE 2475, 487

[18] Griffin M.J. & Orton G.S. 1993, *The near-millimeter brightness temperature spectra of Uranus and Neptune*, Icarus 105, 537

[19] Grün E., Hanner M.S., Peschke S.B. et al. 2001, *Broadband infrared photometry of comet Hale-Bopp with ISOPHOT*, A&A 377, 1098

[20] Gry C., Swinyard B., Harwood A. et al. 2003, *The ISO Handbook: Volume III, LWS – The Long Wavelength Spectrometer*, ESA SP-1262, SAI-99-077/Dc, Version 2.1

[21] Habing H.J., Bouchet P., Dominik C. et al. 1996, *First results from a photometric infrared survey for Vega-like disks around nearby main-sequence stars*, A&A 315, L233

[22] Hammersley P.L., Jourdain de Muizon M., Kessler M.F. et al. 1998, *Infrared standards for ISO. I. A new calibration of mid-infrared photometry*, A&AS 128, 207

[23] Hauser M.G., Arendt R.G., Kelsall T. et al. 1998a, *The COBE Diffuse Infrared Background Experiment (DIRBE) search for the Cosmic Infrared Background. I. Limits and detections*, ApJ 508, 25

[24] Hauser M.G., Kelsall T., Leisawitz D. & Weiland J. (Eds.) 1998b, *COBE Diffuse Infrared Background Explorer (DIRBE) Explanatory Supplement*, Version 2.3. COBE Ref. Pub. No. 98-A (Greenbelt, MD: NASA/GSFC)

[25] Hinkle K., Wallace L. & Livingston W. 1995, *Infrared atlas of Arcturus spectrum, 0.9–53 microns*, PASP 107, 1042

[26] *The Hipparcos and Tycho Catalogues*, 1997, ESA SP-1200

[27] Hrivnak B.J., Volk K. & Kwok, S. 2000, *2–45 $\mu m$ infrared spectroscopy of carbon-rich proto-PNe*, ApJ 535, 275

[28] 'Infrared Astronomical Satellite (IRAS) Catalogs and Atlases Explanatory Supplement' Vol. 1, 1998. Eds. C.A. Beichman, G. Neugebauer, H.J. Habing, P.E. Clegg & T.J. Chester. NASA RP−1190

[29] Justtanont K., Barlow M.J., Skinner C.J., Roche P.F., Aitken D.K. & Smith C.H. 1996, *Mid-infrared spectroscopy of carbon-rich post-AGB obhects and detection of the PAH molecule chrysene*, A&A 309, 612

[30] Klaas U., Radovich M., Wilke K. & Richards P. 2000a, *Report on the PHT Scientific Validation for OLP Version 8.4*, SAI/1999-041/Rp, Version 2.0

[31] Klaas U., Wilke K., Kiss C., Radovich M. & Richards P. 2000b, *Report on the PHT Scientific Validation for OLP Version 9.0*, SAI/2000-014/Rp, Version 2.0

[32] Klaas U. & Richards P. 2002, *Report on the PHT Scientific Validation for OLP Version 10.0*, Version 1.0, 9 April 2002 (see ISOPHOT documentation under: `http://www.iso.vilspa.esa.es`)

[33] Laureijs R.J et al. 1999, *A systematic search for Vega-like stars with ISO*, in 'Astrophysics with Infrared Surveys: A Prelude to SIRTF', Eds. M.D. Bicay, R.M. Cutri & B.F. Madore, ASP Conf. Series 177, 359

[34] Laureijs R.J., Jourdain de Muizon M., Leech K. et al. 2002, *A 25 μm search for Vega-like disks around main-sequence stars with ISO*, A&A 387, 285

[35] Lellouch E., Crovisier J., Lim T. et al. 1998, *Evidence for water ice and estimate of dust production rate in comet Hale-Bopp at 2.9 AU from the Sun*, A&A 339, L9

[36] Lim T., Hutchinson G., Chan S.J. & Müller T. 2001, *LWS OLP 10 Scientific Validation Report*, (see LWS documentation under: `http://www.iso.vilspa.esa.es`)

[37] Metcalfe L. et al. (Eds.) 2002, *The Calibration Legacy of the ISO Mission*, ESA SP-481 (in press)

[38] Müller T. 2001, *Non-linear detector response of LWS LW-Detectors*, IDC Report SAI/2001-042/Rp, December 2001

[39] Müller T. & Lagerros J.S.V. 2001, *Asteroids as calibration standards in the thermal infrared - Applications and results from ISO*, in 'The Calibration Legacy of the ISO Mission', Eds. L. Metcalfe et al., ESA SP-481 (in press)

[40] Müller T. & Lagerros J.S.V. 2002, *Asteroids as calibration standards in the thermal infrared for space observatories*, A&A 381, 324

[41] Omont A., Moseley S.H., Cox P. et al. 1995, *The 30 μm emission band in carbon-rich pre-planetary nebulae*, ApJ 454, 819

[42] Parthasarathy M., García-Lario P., Gauba G. et al. 2001, *IUE and ISO observations of the bipolar proto-planetary nebula Hen 401*, A&A 376, 941

[43] Schulz B., Clavel J., Altieri B. et al. 2001, *PHT-S spectroscopy of Seyfert galaxies*, in 'ISO Beyond Point Sources: Studies of Extended Infrared Emission', Eds. R.J. Laureijs, K. Leech & M.F. Kessler, ESA SP-455, 245